## Publication A

Ostrovska, Lucie, Antonin Broz, Anna Fucikova, **Tereza Belinova**, Hiroshi Sugimoto, Takashi Kanno, Minoru Fujii, Jan Valenta, and Marie Hubalek Kalbacova. "**The Impact of Doped Silicon Quantum Dots on Human Osteoblasts**." RSC Advances 6, no. 68 (2016): 63403-13, IF = 3,289

RSC Advances



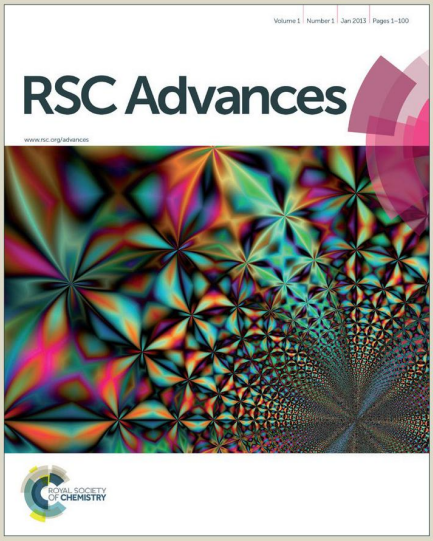




ROYAL SOCIETY OF CHEMISTRY

www.rsc.org/advances

View Article Online
DOI: 10.1039/C6RA14430F



# The Impact of Doped Silicon Quantum Dots on Human Osteoblasts

Lucie Ostrovska[1,2], Antonin Broz[2,3], Anna Fucikova[4], Tereza Belinova[5], Hiroshi Sugimoto[6], Takashi Kanno[6], Minoru Fujii[6], Jan Valenta[4], Marie Hubalek Kalbacova[1,2]*

[1] Biomedical Center, Faculty of Medicine in Pilsen, Charles University in Prague, Pilsen, Czech Republic
[2] Institute of Inherited Metabolic Disorders,1st Faculty of Medicine, Charles University in Prague, Prague, Czech Republic
[3] Institute of Physiology, Academy of Sciences of the Czech Republic, Prague-Krč, Czech Republic
[4] Faculty of Mathematics and Physics, Prague, Czech Republic
[5]Department of the Cell Biology, Faculty of Science, Charles University in Prague, Prague, Czech Republic
[6]Department of Electrical and Electronic Engineering, Graduate School of Engineering, Kobe, Japan

* corresponding author:
Marie Hubalek Kalbacova : marie.kalbacova@lf1.cuni.cz

## Abstract

Silicon (Si) nanostructures allow for the expansion of the application spectrum of this important semiconductor material with respect to the fields of optoelectronics and photonics. At the same time, the significant potential of Si quantum dots (SiQDs) has been revealed in terms of their potential application in the areas of biology and medicine due to their biocompatibility, low toxicity and natural biodegradability unlike currently used semiconductor quantum dots. As far as this study is concerned, SiQDs co-doped with boron and phosphorus were used for the *in vitro* evaluation of their cytotoxicity in human osteoblasts. Two chemically identical types of SiQD differing in terms of their size and photoluminescence (PL) were studied. They both display long-lasting dispersion in methanol and even in aqueous media as well as PL which is not sensitive either to changes in the environment or surface modifications. Our experiments revealed significant differences between the two types of SiQD tested with concern to their behavior in a cell culture environment depending on increasing concentration (25 – 125 µg/ml) and cultivation conditions (the presence or absence of proteins from the fetal bovine serum - component of the cultivation medium). Detailed description of their optical parameters and the evaluation of zeta potential enhance the understanding of the complexities of the *in vitro* results obtained.



## 1 Introduction

Various types of nanoparticles have been studied and used in different fields of science including their application in the field of bio-medicine. In general, nanoparticles (so-called quantum dots - QD)

View Article Online
DOI: 10.1039/C6RA14430F



based on a variety of materials provide a promising tool with regard to potential as drug and gene carriers and as imaging and diagnostic platforms.

Silicon-based nanoparticles make up one of the most promising platforms yet determined for medicinal application due to their high level of biocompatibility and biodegradability which arise from the fact that silicon (Si) is an essential trace element in the human body. Currently, the development of various types of Si-based nanoparticles is focused principally on silica ($SiO_2$) and pure silicon materials which are biodegradable due to the nature of their Si-Si and Si-O bonds.[1,2] In addition, it is essential to note that most Si-based nanoparticles possess the quality of fluorescence (photoluminescence) and therefore facilitate their own imaging without any additional intervention into their structure being required.[3,4] Moreover, their dispersibility in aqueous solutions is also crucial for bio-application.[5] Such properties are similar to the afore-mentioned QDs, thus the term silicon quantum dots (SiQD) is particularly appropriate.

This study is concerned particularly with the assessment of cytotoxicity since this makes up the most important initial step preceding the actual application of any of the materials studied in terms of human medicine. Previous studies have shown that the cytotoxicity of Si-based nanoparticles is influenced by a range of properties such as particle shape, size, zeta potential, dose and chemical composition [6–12] and some of these properties may play a role in the formation of so-called biomolecular coronas. This term describes a layer of biomolecules, mainly proteins (protein corona), originating from the biological environment surrounding nanoparticles which accord them a new identity which differs from that of bare nanoparticle in terms of a number of characteristics especially their reaction with organisms.[13,14] Generally, the concept of the protein corona is given as a biological identity via which nanoparticles are presented to cells. It has been suggested that the presence, and possibly the composition, of the protein corona provides the key to the determination of the cytotoxicity of nanoparticles.[15,16] *In vivo*, the composition of the attached proteins is spatial (lung fluids, bloodstream) and time dependent and, moreover, the condition of the living organism should be considered.[16] On the other hand, *in vitro* conditions are limited by the presence of certain types of proteins contained within the selected supplemented serum; thus, it appears that the protein corona is not subject to the same degree of significant dynamic change in composition as it is *in vivo.* [17]

Previous studies that have focused on the impact of silica nanoparticles ($SiO_2$ NPs) on keratinocytes revealed that the viability of cells is both dose- and size-dependent and, in addition, that this particular type of particle causes damage to the cellular membrane which may be of either chemical or mechanical stress origin.[7,8] It has been proposed that cytotoxicity caused by $SiO_2$ NPs may be the result of oxidative stress induced by the production of intracellular reactive oxygen species.[11,18] However, when compared to other types of nanoparticles, e.g. ZnO particles, $SiO_2$ NPs

View Article Online
DOI: 10.1039/C6RA14430F



reveal lower cytotoxicity levels dependent on the cell type.[7,9,19] Moreover, a number of papers has reported a significant correlation between cytotoxicity and the dose of Si-based nanoparticles (irrespective of the actual concentration range used for a particular cellular type). Generally, the higher the nanoparticle dose applied to the cells, the higher is the cytotoxicity observed following a certain period of time, an example of which is provided by studies by Bhattacharjee et al. wherein increasing concentrations from 0.1 ng/ml - 100 µg/ml of nanoparticles were added to a cell culture of NR8383 macrophages. The same cytotoxicity trend was also evident with respect to keratinocytes, although the concentrations applied were significantly higher (25 – 500 µg/ml).[8,10,11] It is possible to obtain a better understanding of the causes of the cytotoxicity of particular nanoparticles by means of a description of specific cell-nanoparticle interactions.

It is widely accepted that nanoparticles of different types enter cells by means of endocytosis, i.e. a form of active transport; however, the specific ways in which individual particles enter certain cell types remain to be discovered. Considerable interest has been devoted to the discovery of principal nanoparticle uptake pathways and most of the experiments conducted in this respect were performed via the selective gradual blocking of different pathways and the subsequent determination of which was most frequently used. Clathrin- and caveolin-dependent endocytotic pathways have been suggested as the main routes used by silicon-based particles; however, a number of studies also suggest the use of the flotillin-dependent pathway.[12,20] It has been implied that the principal pathway is determined not only by particle size and shape but also by cellular type. It is important to gain an understanding of all the interactions which take place between cells and nanoparticles so as to avoid any harmful effects in terms of potential use in human medicine.

This study employed two types of SiQD of different characteristics (SiQD 1050 – 3 nm size, 750 nm peak emission and SiQD 1100 – 4 nm size, 850nm peak emission) and their influence on a biological system represented by a human osteoblast-like cell line (SAOS-2) was compared. The main focus of the study was i) to determine the appropriate concentration of both types of SiQD based on the induced cytotoxicity and ii) to evaluate the cellular uptake of both SiQDs at 2, 6 and 24 hours by means of fluorescence wide-field and confocal microscopy. The influence of the presence of fetal bovine serum (FBS) in the cultivation media made up an important variable parameter in terms of understanding the impact of the protein corona on SiQD behavior *in vitro*.

## 2 Experimental

### 2.1 The fabrication of co-doped SiQDs

P and B co-doped colloidal Si QDs were synthesized by means of a previously reported procedure.[21,22] Si-rich borophosphosilicate (BPSG) films were deposited on thin stainless steel plates

View Article Online
DOI: 10.1039/C6RA14430F



via the co-sputtering of Si, $SiO_2$, $B_2O_3$, and $P_2O_5$ using the rf-sputtering apparatus. The films were then peeled from the plates and crushed to powder form in a mortar. The powder was then annealed at different temperatures (1050°C and 1100°C thus obtaining SiQD 1050 and SiQD 1100 respectively) in an $N_2$ gas atmosphere for 30 minutes so as to cultivate SiQDs of differing size in BPSG matrices. During the growth of the SiQDs, P and B atoms were incorporated into Si-NCs from the BPSG matrices.

## 2.2 The detailed optical characterization of co-doped Si-QD

Transmission electron microscopy images were obtained using JEOL JEM-200CX, and the IR absorbance of the suspensions measured by means of drop-casting on a gold covered silicon substrate in an FT-IR spectrometer (Perking Elmer, Spectrum GX). UV-VIS spectra were measured by UV-3101PC (Shimadzu). The PL spectra (Figure 1d) were obtained using a spectrofluorometer (Fluorolog-3, Horiba Jobin-Yvon).

The photoluminescence external quantum yield (EQY) of the SiQD suspensions was measured in specially-designed equipment based on an integrating sphere.[23] Excitation wavelengths were tuned over a broad spectral range from UV to yellow using either a set of light-emitting diodes or a white-light emitting laser-driven light source (LDLS, Energetiq) coupled to a 15-cm monochromator. The absorption cross-section $\sigma$ was obtained by means of the intensity-dependent PL-modulation technique applied to a thin liquid layer of SiQD in methanol.[24] Under 405 nm excitation and an emission between 700 and 900 nm, $\sigma$ was determined at around $3 \times 10^{-16}$ $cm^2$ for both of the samples studied.

The PL kinetics of SiQDs under high-repetition short pulses (simulating the conditions of a confocal microscope with a “white” fiber laser) were tested for SiQD 1050 in a cuvette excited via a pulsed diode laser at 408 nm (pulse duration below 0.1 ns, 20 MHz repetition rate and 840 $W/cm^2$ power density) (Figure 3 b).

## 2.3 Zeta-potential assessment

$\zeta$ was measured using a Malvern Zetasizer Nano ZS equiped with MPT-2 titration unit where 0.25 M NaOH, 0.2 M HCl and 0.02 HCl were used as titration agents. The SiQD suspensions were titrated in the acid to base and base to acid direction.

## 2.4 Cell cultivation with SiQDs

SAOS-2 cells (DSMZ, Germany) were cultured in McCoy’s 5A medium without phenol red (HyClone) and supplemented with 10 000 U/ml penicillin (Sigma-Aldrich) and 10 µg/ml streptomycin (Sigma-Aldrich) and, in some of the experiments, with 15% fetal bovine serum (Biosera). The cells were seeded at a density of 10 000 cells/cm² onto a 96-well plate (Techno Plastic Products) in triplets for the measurement of cytotoxicity (100 µl) or onto cell imaging dishes with a 145 µm glass bottom

View Article Online
DOI: 10.1039/C6RA14430F



in singlets (Eppendorf) for microscopy purposes (500 µl). The cells were cultured for 24 hours in a humidified 5% $CO_2$ atmosphere at 37°C.

The required amount of SiQD colloid in pure methanol was added to an equal amount of distilled water and the resulting mixture was subsequently incubated in a dry bath incubator (Major Science) set to 70°C until half of the liquid had evaporated. The final SiQD colloid was ready for immediate dilution into the appropriate cultivation media. Two types of cultivation media were used in the experiments - McCoy's 5A medium without phenol red (HyClone) with 10 000 U/ml penicillin (Sigma-Aldrich) and 10 µg/ml streptomycin (Sigma-Aldrich) with no serum proteins (serum-free) or supplemented with 5% fetal bovine serum (Biosera) (serum-supplemented). The final concentrations of SiQD in the media used for cell treatment consisted of 125 µg/ml, 50 µg/ml and 25 µg/ml.

The cells were gently rinsed with phosphate buffer saline (PBS) prior to the addition of the cultivation media containing SiQDs. Subsequently, the cells were cultivated to different time points depending on the type of assessment. In the case of the serum-free media, an additional volume of 50 µl (96-well plate) or 250 µl (cell imaging dish) of the medium with 5% FBS was added after 6 hours of cultivation and cultivated for an additional 18 hours or 42 hours (in the case of 24 hours or 48 hours of cultivation time respectively).

### 2.5 Cytotoxicity assessment

The cytotoxicity of various concentrations of SiQDs in different media was assessed by means of the measurement of the metabolic activity of the cells at 6, 24 and 48 hours following the addition of SiQDs to the cells. Assessment was performed by means of MTS assay (Cell Titer96® AqueousOne, Promega). The principle of this colorimetric assay consists of the reduction of an MTS ((3-(4.5-dimethylthiazol-2-yl)-5-(3-carboxymethoxyphenyl)-2-(4-sulfophenyl)-2H-tetrazolium)) compound into a soluble colored formazan product via mitochondrial dehydrogenases. The assay was performed according to the manufacturer's instructions. The cells were rinsed three times with PBS and then incubated for 2 hours with an MTS reagent diluted in the appropriate media. Optical density was measured using a microplate reader (Synergy H1, BioTek) at 490 nm subtracting the background at 655 nm. The subtraction of blank values was conducted for each type of medium separately. All the results obtained were compared to the results of the control cells cultivated in a medium supplemented with 5% FBS; the results were expressed as percentages.

### 2.6 Fluorescence wide-field and confocal microscopy

After 2, 6 and 24 hours the cells were rinsed three times with PBS so as to remove any un-internalized SiQDs and then fixed in 4% paraformaldehyde. An Eclipse Ti-S epi-fluorescence microscope (Nikon) with Mercury Arc Lamp Intensilight HGF1 and equipped with DS-Qi1Mc digital camera (Nikon) was used in order to acquire 2D fluorescence images of SiQDs at an excitation

View Article Online
DOI: 10.1039/C6RA14430F



wavelength of 330 – 380 nm and emission wavelength of 510 - 590 nm. The extent of the penetration of SiQDs in the z-axis of the cells was analyzed with respect solely to the 24 hour samples by means of a Leica TCS SP8X confocal laser scanning microscope (Leica Microsystems). The SiQDs were excited using a pulse continuum white light laser (475-499 nm, 80 MHz) and emissions were collected via a hybrid detector at 700 - 795 nm. The elimination of cell autofluorescence from SiQD signals was achieved by the gating of signal detection with a 5 ns delay from the excitation pulse while maintaining a detection width of 7 ns. Multiple line accumulation scanning and prolonged pixel dwell were set so as to allow for the more intense and precise imaging of the SiQDs. All the confocal 3D images were acquired by means of a Leica DFC365 FX monochrome digital CCD camera and further analyzed using LAS X core software (Leica Microsystems). The confocal images were processed using Hyugens software for deconvolution and maximum intensity projection. ImageJ software was subsequently used for contrast and smoothness correction purposes.

### 2.7 Statistical analysis

All the data presented was derived from three independent experiments performed in triplicate. The results are presented in the form of mean values with error bars indicating standard deviations. Data distribution was evaluated using the Shapiro-Wilk test. The nonparametric Wilcoxon matched pairs test was used in order to determine significant differences between the datasets and the control with 5% FBS and the rest of the variables. An ANOVA was used to compare differing SiQD concentrations at certain time points with each other. P values of less than 0.05 were considered statistically significant. Extreme values were excluded from the analysis. Statistical analysis was performed using STATISTICA (StatSoft, Inc.) software.

## 3 Results and discussion

### 3.1 The optical characterization of co-doped SiQD

Phosphorus (P) and boron (B) co-doped colloidal SiQDs were synthesized by means of a previously reported procedure.[21,22] The transmittance spectrum and an image of the colloid are shown in Figure 1a. Transmittance around the band gap of bulk Si crystal (~1100 nm) is almost 100%, which indicates the absence of significant light scattering by QD agglomerates. Figure 1b shows a transmission electron microscope (TEM) image demonstrating a QD monolayer without the formation of three-dimensional agglomerates. Figure 1c shows an infrared (IR) absorption spectrum of SiQD 1100 stored in methanol for 60 days. An absorption peak at ~1080 $cm^{-1}$ assigned to Si-O-Si stretching vibrations can be clearly observed while no absorption peak is evident from C-$H_x$ (~2900 $cm^{-1}$). This suggests that following long-term storage in methanol, the surface of SiQDs is terminated principally by

View Article Online
DOI: 10.1039/C6RA14430F



oxygen. After around one month's storage in methanol, the photoluminescence (PL) spectra of SiQD 1050 and 1100 under excitation at 450 nm exhibit PL peaks of around 750 and 850 nm respectively (Figure 1d). The size-dependence of the PL peak wavelength of B and P co-doped Si QDs has already been studied in detail.[25]

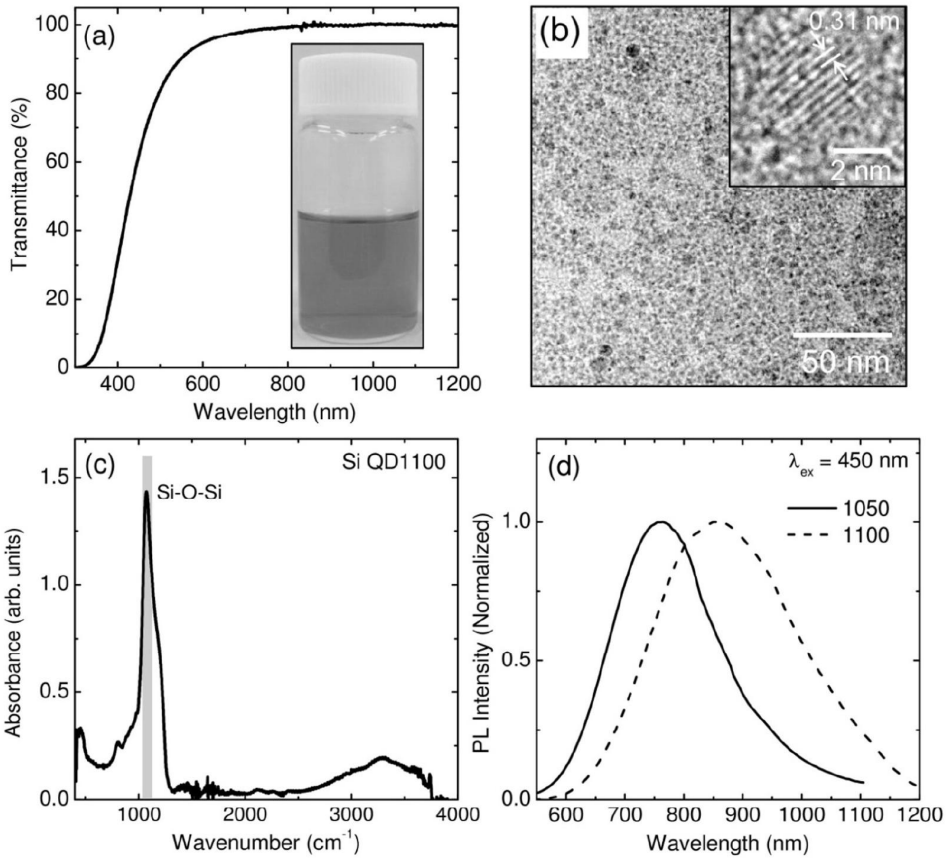


**Figure 1.** (a) Optical transmittance spectrum and photograph of colloidal dispersion (methanol) of SiQD 1100; (b) TEM image of SiQD 1100, Inset: High-resolution TEM image of a QD with lattice fringes corresponding to {111} plane of Si crystals; (c) IR absorption spectrum of SiQD 1100; (d) PL spectra of SiQD 1050 and 1100 (d).

With respect to the imaging of SiQD in cell cultures by means of fluorescence microscopy (wide-field or confocal), the presence of so-called autofluorescence (AF) – i.e. the natural fluorescence of cell proteins and other molecules without artificial staining must be considered. AF usually peaks in green but extends far into the red spectral region in which it overlaps with the PL of the tested SiQDs. This is illustrated in Figure 2 which shows the local PL spectra of the AF and PL of SiQD 1100 under excitation by means of a laser at 405 nm. In general, three measures can be applied so as to improve the ratio of SiQD PL versus AF:

View Article Online
DOI: 10.1039/C6RA14430F



(i) The shifting of the excitation wavelength into the green region (e.g. the Ar-ion laser line at 488 nm) since AF decreases faster with red-shift excitation than does SiQD PL.

(ii) The selection of SiQDs with an emission peaking at long wavelengths where AF disappears but where microscope detectors remain efficient; this usually means between 700 and 800 nm.

(iii) The use of different PL decay kinetics under pulsed excitation. While AF decays within a few nanoseconds, SiQDs have a lifetime in the order of tens of microseconds. Therefore, gated detection can be applied which is delayed following pulsed excitation by around 5 ns. Figure 3a shows the slow rate of PL decay for both the SiQD samples and Figure 3b illustrates that PL decay under excitation by sub-ns pulse with high repetition rate (20 MHz - such a degree of excitation is deliverable by a large number of currently available confocal microscopes) was unable to follow the pulse sequence and thus quasi-constant PL was detected – the yellow rectangle indicates the temporal position of the detection gate (delay 5-12 ns) as used later in this paper (such excitation and detection options are available in a large number of the current models of confocal microscopes).

Finally, we draw attention to the aging of the luminescence properties of SiQDs. During long-term storage (around 1 year) a slow change in the PL peak position and the external quantum yield (EQY) can be observed in methanol suspensions of SiQDs, which is further accelerated in water-based suspensions used in bio-studies. Both types of SiQD exhibit a blue-shift and the EQY changes as illustrated in Figure 2c roughly following a curve which has a maximum EQY of 12% for a peak at 750 nm (similar optimal conditions were reported by Liu et al).[26] Such optimum conditions for fluorescence imaging are characteristic of fresh SiQD 1050 samples; however, upon aging such samples degrade in terms of EQY while SiQD 1100 shifts to the optimum position (a shift from 850 nm to 750 nm). In brief, it is essential that aging properties are characterized in order to be able to anticipate PL evolution and select the ideal sample.

View Article Online
DOI: 10.1039/C6RA14430F



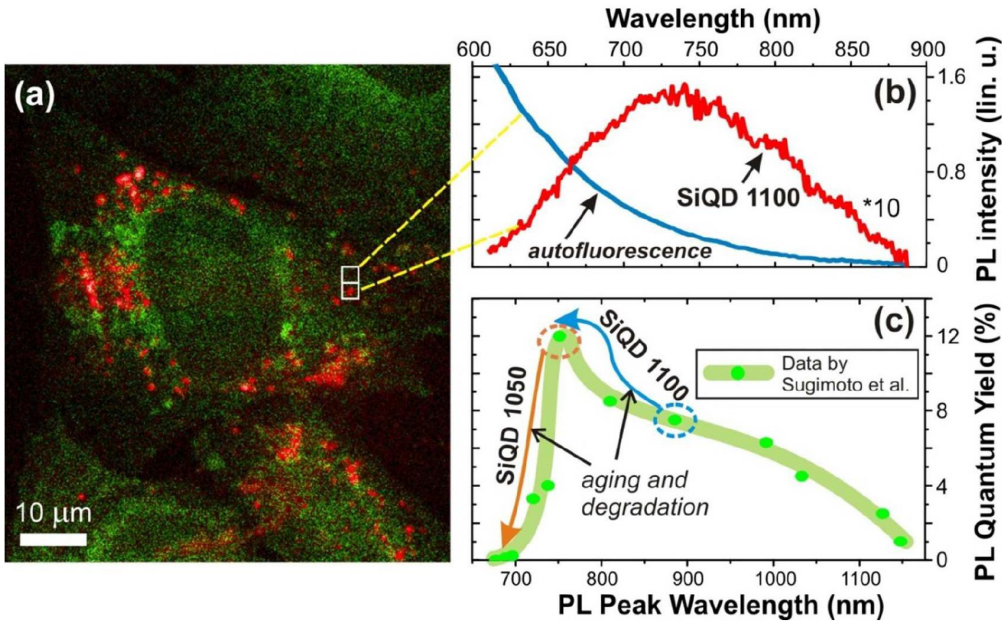


**Figure 2.** Wide-field fluorescence microscopy and spectroscopy under cw excitation at 405 nm: (a) Combined fluorescence image with the green layer showing the full signal (dominated by cell autofluorescence) and the orange layer showing signal above 785 nm (dominated by SiQD luminescence). The vertical stripe shows area of the spectrometer slit introduced for spectral measurements. (b) Luminescence spectrum of cell autofluorescence (blue) and emission of SiQD cluster (red line) from area indicated by a rectangle in the panel a. The autofluorescence signal estimated from area around the SiQD cluster was subtracted and spectral shape corrected to the sensitivity of the experimental apparatus. The peak is around 730 nm. (c) Observed shift of PL peak and quantum yield of SiQDs with time is plotted together with data from the paper by Sugimoto et al .[20] The slow changes due to aging of SiQD suspensions in methanol are accelerated in water based media during bio-studies. The data (green line and points) on PL QY dependence on PL peak position (size of QDs) explains well why T1100 sample is well observed in cell cultures while luminescence of T1050 vanishes.

View Article Online
DOI: 10.1039/C6RA14430F



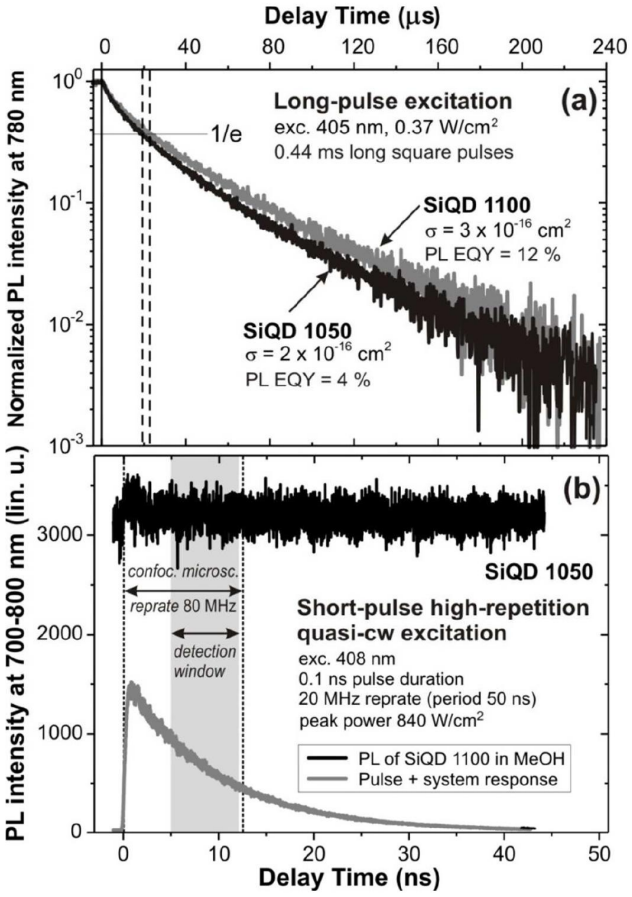


**Figure3.** (a) Kinetics of PL decay under long square pulses and (b) short high-repetition rate (quasi-cw) excitation. The conditions applied in the confocal imaging (80 MHz repetition rate, detection window of 7 ns delayed by 5 ns) is indicated by the yellow rectangle.

### 3.2 Zeta potential assessment

The zeta potential (ζ) of water suspensions of SiQD 1050 and 1100 as a function of pH was determined using 0.25 M NaOH, 0.2 M HCl and 0.02 HCl titration agents. The SiQDs had been titrated in the acid → base and base → acid direction (Figure 4). The iso-electric point of both samples was determined at around pH 2. While SiQD 1100 reacted relatively smoothly to changes in pH, the SiQD 1050 reaction to the addition of acid/base was slow and followed by sudden jumps in ζ. Moreover, a two-peak distribution of ζ was observed for SiQD 1050 at each pH point (Figure 4d) indicating the presence of distinct SiQD fractions. For a pH of 7.5 (the value relevant to biological experiments) the mean value of ζ was around – 64 mV (-16 mV for the smaller peak) for SiQD 1050 and – 57 mV for SiQD 1100 (with an uncertainty of around 8 mV).

View Article Online
DOI: 10.1039/C6RA14430F



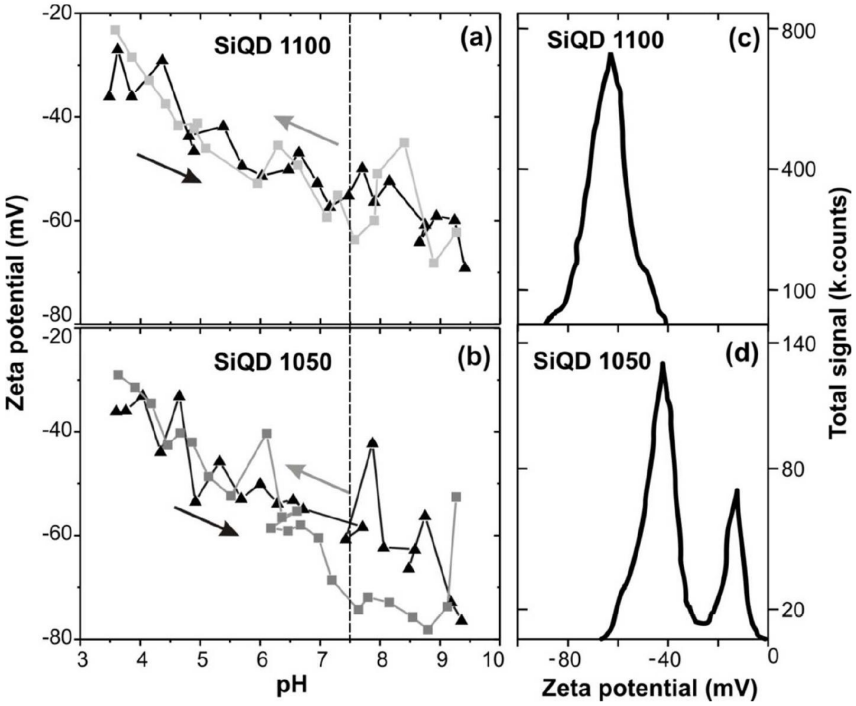


**Figure 4.** Zeta-potential evaluation: (a) Titration curves of SiQD 1100 and (b) SiQD 1050 (each point is average of three measurements). Small graphs show an example of single measurement of zeta potential at pH 7.5 in (c) SiQD 1100 and (d) SiQD 1050.

### 3.3 The effect of different SiQD concentrations on cell metabolic activity in serum-supplemented and serum-free media

Osteoblastic cells were cultivated in a medium supplemented with 5% fetal bovine serum (5% FBS-medium) with gradually increasing concentrations (25, 50 and 125 μg/ml) of two types of SiQD which was followed by the determination of their metabolic activity after 6, 24 and 48 hours (Figure 5 a, b). It is apparent that SiQD 1100 in a fully-supplemented medium had no impact on cell metabolic activity irrespective of concentration at the 6-hour time point; however, after 24 hours the highest concentration of SiQD 1100 decreased cell activity significantly and, after 48 hours, the medium concentration was seen to have a similar effect.

On the other hand, SiQD 1050 (lowest and medium concentrations) surprisingly increased cell metabolic activity after 6 hours and, after 24 hours of incubation, the metabolic activity of SiQD 1050-treated cells was comparable to that of controls with no treatment. Only after 48 hours did the highest concentration of SiQD 1050 significantly decrease cell metabolic activity.

In order to distinguish between the effect of SiQDs and the role of the protein corona (originating from serum proteins), osteoblastic cells were cultivated in a medium containing no supplements

View Article Online
DOI: 10.1039/C6RA14430F



(serum free – 0% FBS-medium). The same concentrations of SiQDs were then added and the same tests performed as described above (under standard conditions). It is apparent (Figure 5 c, d) that the serum-free medium only (with no SiQDs) had a negative effect on cell metabolic activity at the 6-hour time point; however, the decrease was not so strong as to be considered cytotoxic.[27]

Those cells treated in the serum-free medium with the lowest and medium concentrations of SiQD 1100 exhibited a metabolic activity level similar to the control sample (cells cultivated in a 5% FBS-medium) and only in the highest SiQD concentration did cell activity decrease significantly to the cytotoxic level after 6 hours (in contrast to standard conditions). Subsequently, after 24 hours, both the medium and the highest concentrations of SiQD 1100 were found to strongly affect cell activity and, finally (after 48 hours) all the tested concentrations of SiQD 1100 in the serum-free medium were determined as being cytotoxic.

On the other hand, SiQD 1050 did not affect cell behavior at any concentration after 6 hours; however, after 24 hours of incubation, all the tested concentrations were found to be cytotoxic, the level of which was further enhanced following 48 hours of incubation.

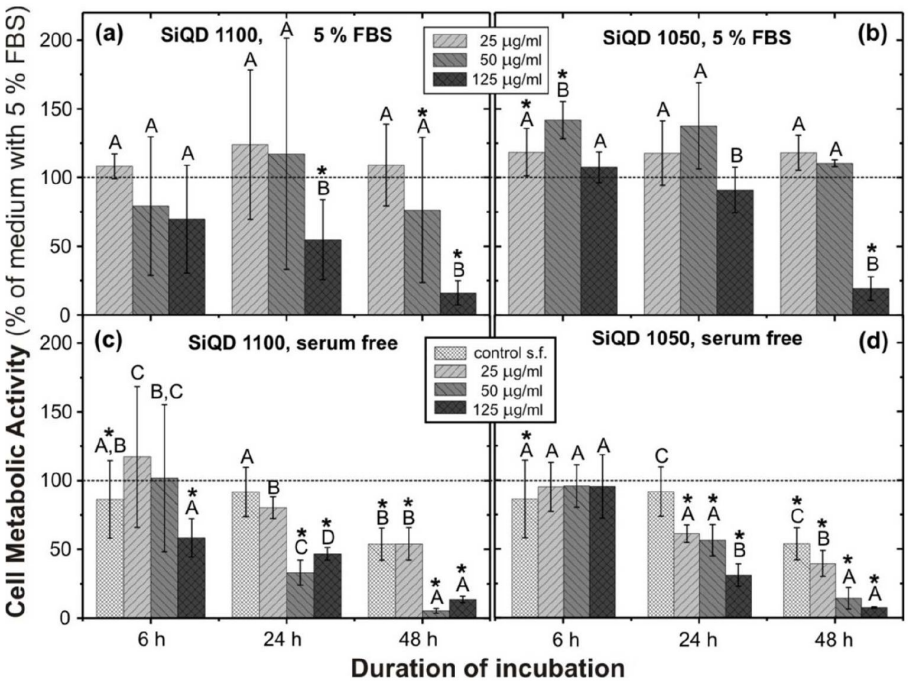


**Figure 5.** Metabolic activity of osteoblasts cultivated in a cultivation medium supplemented with 5% FBS (a, b) and in serum free medium (c, d) for increasing concentration of SiQD 1100 (a ,c) and SiQD 1050 (b, d). Relative values are expressed as a percentage of control sample in the cultivation medium with 5% FBS (dashed line). The star symbol (*) highlights a significant difference from the control in cultivation medium with 5% FBS (Wilcoxon matched-pairs test, $p < 0.05$). Groups marked with different letters express significant inter-group differences within time points (ANOVA, LSD post hoc test, $p < 0.05$).

View Article Online
DOI: 10.1039/C6RA14430F



### 3.4 The microscopy assessment of SiQD effects on cell morphology and metabolic activity in serum-supplemented and serum-free media

Osteoblasts were treated with 50 μg/ml of SiQD 1050 and SiQD 1100 (medium concentration) in a 5% FBS-medium for 2, 6 and 24 hours and then visualized by means of wide-field fluorescence microscopy accompanied by a phase contrast for the more precise localization of the SiQD fluorescence signal within the cells (Figure 6a, b). Confocal microscopy images of cells treated with the same SiQD concentrations were acquired at the 24-hour time point only (Figure 6 c, d).

Figure 6a shows that a very bright fluorescence signal is visible in those cells treated with SiQD 1100 as soon as after 2 hours and that it is even stronger at the 6-hour time point. However, it is apparent from the phase contrast image that the signal originates from a culture medium in which aggregates of SiQD with proteins originating within the FBS had formed and not from the cells themselves. After 24 hours, the fluorescence signal of SiQD 1100 is apparent from inside the cells as well as from the culture medium itself. The confocal image (Figure 6c) taken at the same time confirms the localization of these SiQDs inside cells in a vesicular form with no apparent changes in cell morphology. In addition, cell metabolic activity tests (Figure 8a) indicated that these SiQDs had no negative impact on the cells at the same time point; only after 48 hours of incubation did the SiQD 1100 cause a significant decrease in cell metabolic activity but not to such an extent as to include cytotoxic effects.[27]

In the case of SiQD 1050 an even stronger fluorescence signal of SiQD and proteins in the cultivation medium was detected after 6 hours but only a very weak signal could be detected in the cells after 24 hours (Figure 6 b). The image of cells treated with SiQD 1050 for 24 hours presented was intentionally selected so as to show the cells in the region not totally covered with SiQD-protein aggregates; notwithstanding, most of the sample area was found to be covered with these foggy aggregates. This observation was confirmed by means of confocal imaging (Figure 6d) which revealed a weak fluorescence signal distributed diffusely within the cells (autofluorescence) and a concentrated signal issuing from the culture medium in which SiQD 1050 aggregates and FBS proteins were formed. Indeed, this corresponds well with the data presented in Figure 8b according to which no reduction in metabolic activity (compared to the untreated control in the 5% FBS-medium) was detected in either evaluation using the same concentration of SiQD 1050.

View Article Online
DOI: 10.1039/C6RA14430F



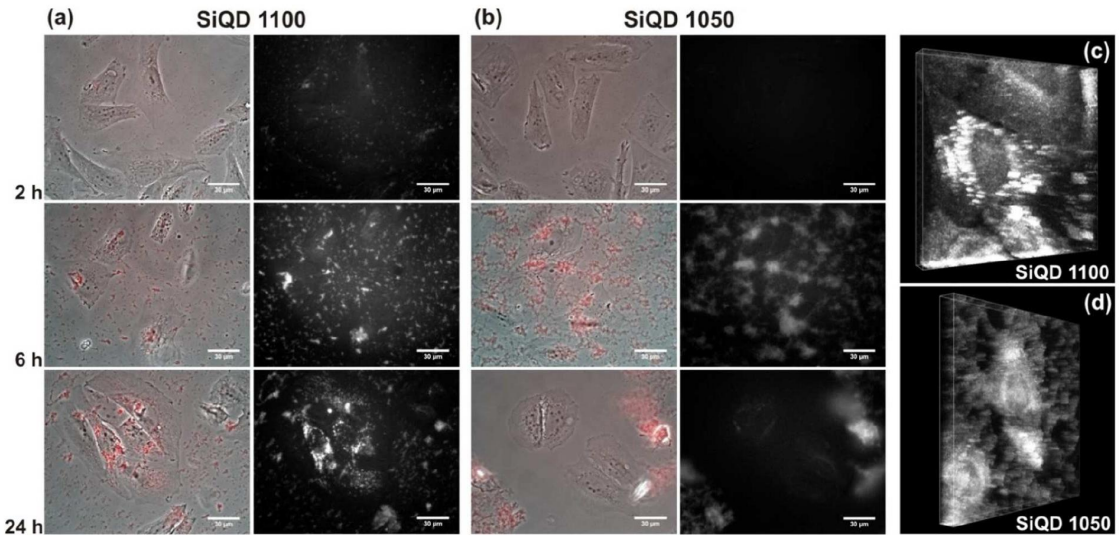


**Figure 6.** Wide-field fluorescence and phase contrast microscope images of osteoblasts treated with (a) SiQD 1100 and (b) SiQD 1050 in 5%FBS-supplemented medium in different time points (the scale bar is 30 μm) and confocal images after 24 h of incubation with (c) SiQD 1100 (imaged volume 75.0 x 75.0 x 7.6 μm) and (d) SiQD 1050 (imaged volume 112.6 x 112.6 x 9.5 μm).

Subsequently, the same experiments were performed with using the serum-free medium (0% FBS-medium). Figure 7a shows that a fluorescence signal is visible in those cells treated with SiQD 1100 as soon as after 2 hours of incubation and it is even stronger at the 6-hour point at which all the cells exhibit a fluorescence signal. After 24 hours, SiQD and protein aggregates were visible in the medium. The proteins originated from the FBS added to the culture medium after 6 hours due to the cells being unable to survive (i.e. to avoid significant behavioral changes) any longer without the addition of FBS. It was expected that all the SiQDs would already have entered the cells by this time point and that they would no longer be present in the medium. However, microscope images demonstrate that after 6 hours a certain amount of SiQD 1100 was still present in the medium available to react with the FBS proteins. Nevertheless, SiQD 1100 were present on a massive scale inside the cells at 24 hours (Figure. 7a) and had a negative impact on cell morphology; moreover, this led to a significant decrease in cell metabolic activity (Figure 8a). The confocal image (Figure 7c) confirms the presence of high quantities of SiQD 1100 inside the cells in the diffused form which is in contrast to the localization of SiQD 1100 in those cells cultivated in the 5% FBS-medium (Figure 6c). Results concerning metabolic activity indicate that the cells were dying at a rapid rate at the 24-hour point and had died at the 48-hour time point.

Conversely, SiQD 1050 were practically invisible at all time points in those cells cultivated in the serum-free medium; a very faint signal was detectable at the 2-hour time point which disappeared over time (Figure 7b). The wide-field microscopy data was confirmed by the confocal images in which

View Article Online
DOI: 10.1039/C6RA14430F



the fluorescence signal was very faint and originated from cell autofluorescence. However, the results presented in Figure 8b suggest that a reduction in metabolic activity occurred after 24 hours of incubation (also apparent in the form of changed cell morphology in Figure 7 b) and that at the 48-hour point the cells had already died.

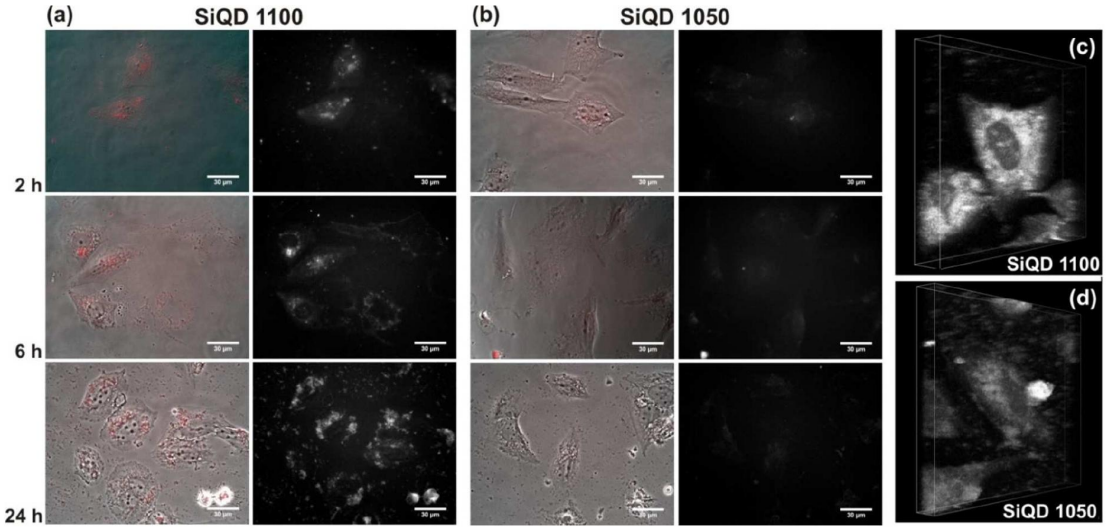


**Figure 7.** Wide-field fluorescence and phase contrast microscope images of osteoblasts treated with (a) SiQD 1100 and (b) SiQD 1050 in the serum-free medium in different time points (the scale bar is 30 μm) and confocal images after 24 h of incubation with (c) SiQD 1100 (imaged volume 85.0 x 85.0 x 11.6 μm) and (d) SiQD 1050 (imaged volume 102.0 x 102.0 x 9.6 μm). Note – After 6 h of cell incubation in serum-free medium, FBS was added due to the cell survival purposes.

View Article Online
DOI: 10.1039/C6RA14430F



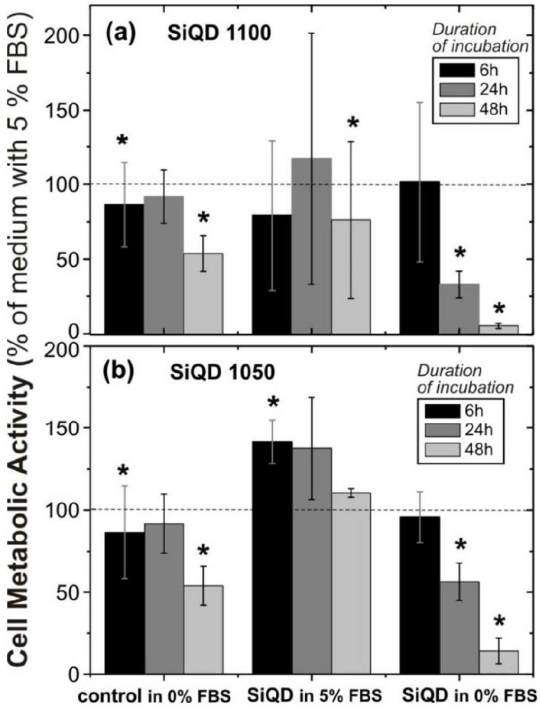


**Figure 8.** Metabolic activity of osteoblasts treated with 50 μg/ml of (a) SiQD 1100 and (b) SiQD 1050 for different time points.

This report presents the first study performed on the impact of novel Si-based nanoparticles on a biological environment consisting of a human osteoblast cell culture. The most unique property of the B and P co-doped SiQDs used consists of their ability to form stable colloidal suspensions in the absence of surfactants and organic passivation. Moreover, these SiQDs required no protective shell layer and were of a very small size (3-4 nm in diameter) in contrast with other semiconductor quantum dots with a core-shell structure and which are substantially larger than 10 nm (not taking into account possible surface passivation) in order that they exhibit a stable emission in a similar spectral region on the border of red and infrared (700 – 850 nm).[28] We selected two types of SiQDs with sizes of 3 and 4 nm (SiQD 1050 and 1100 respectively) the PL emission peaks of which are situated in the afore-mentioned spectral range which is optimal in terms of fluorescence microscopy. Somewhat surprisingly, our experiments revealed significant differences with respect to the interaction of the two types of SiQD with cell cultures which could not be ascribed simply to the 1 nm size difference - at the cellular level such a small difference does not influence particle cytotoxicity and only a slight change in cellular uptake is able to occur.[29–31]

Zeta-potential (ζ) is related to colloidal suspension stability. The critical value of ζ below which a suspension is unstable (and at which agglomeration can take place) is around ± 30 mV.[32] Generally,

View Article Online
DOI: 10.1039/C6RA14430F



ζ is result of the net electrical charge contained within the region bounded by the slipping plane. This charge is strongly dependent on ions present in the solution and therefore changes with pH value. The pH value, for which the net electrical charge is null, is called isoelectric point. Around this point the nanoparticles aggregate rapidly. With concern to biology, the surface potential of a particle is important in terms of the formation of protein corona – nanoparticles with different potentials will bind to different proteins or to different active sites on individual proteins which, in turn, may significantly influence the overall toxicity of nanomaterials. An example of the varying degree of toxicity of Si nanoparticles depending on the value of ζ and the particle covering is reported in [10,11]; however, this effect has also been observed with respect to other types of nanoparticles.[33,34] Our experiments resulted in different values of ζ for Si QD 1050 and 1100; therefore we suspect the formation of a differing protein corona under the same biological conditions.

Both of the tested SiQDs caused harm to the cells in a different manner – SiQD 1100 exhibited a measurable harmful effect at the highest applied concentration level (125 μg/ml) as soon as after 24 hours of incubation in the fully-supplemented medium, while the negative effect of SiQD 1050 was not apparent until after 48 hours of incubation (Figure 5). It is conjectured that this difference may be linked to the observed formation of dense clusters of SiQD 1050 with serum proteins (see the fluorescence images in Figure 6). These clusters act as reaction centers and continue to grow thus forming huge aggregates which cover the outside membranes of the cells and prevent SiQD 1050 from entering the cells. When subjected to fluorescence microscopy, protein/SiQD 1050 aggregates are visible as fog-like structures which grow over time (Figure 6 b, d). Despite this effect, however, a number of uncovered locations were detected after 48 hours thus providing coarse information on the incorporation of SiQD 1050 into the cells (Figure 6b). This phenomenon was also witnessed with respect to SiQD 1100 but to a significantly lesser extent which, nevertheless, still allowed for the visualization of the cells and their incorporation of SiQD 1100. Notably, literature describes this aggregation effect with respect to other types of nanoparticles.[35,36] Therefore, it is safe to conclude that the presence of FBS proteins in the cultivation medium strongly influence specific SiQD behavior and thus their availability and absorption by cells. It may be speculated from the fluorescence images (Figure 6c) that the SiQD 1100 visible in cell cytoplasm are localized in vesicles and thus potentially enter cells by means of endocytosis as has been previously described.[37–40]

When SiQDs were incubated with cells in the serum-free medium, SiQD 1100 exhibited a cytotoxic effect at the highest applied concentration level (125 μg/ml) as soon as after 6 hours of incubation (Figure 5c). Therefore, it was concluded that bare SiQDs (without a protein corona) are able to cross cell membranes more easily and efficiently than treated SiQDs. This statement was subsequently

View Article Online
DOI: 10.1039/C6RA14430F



proven by means of fluorescence imaging (Figure 7a) which revealed the presence of SiQD 1100 in the cell cytoplasm but, surprisingly, that it was localized diffusely rather than in the form of whole spots as in the case of standard cultivation conditions with the presence of FBS. It would appear that the way in which SiQD 1100 enter cells varies under different conditions (with or without a protein corona), a fact that might be studied in greater detail in the future. SiQD 1050 required a longer incubation time (24 hours) before they entered the cells under serum-free conditions; importantly, however, the effect was significantly stronger – all the concentrations of SiQD 1050 tested were found to be cytotoxic after 24 hours (Figure 5d). Both SiQDs in the serum-free medium were seen to harm the cells earlier and at a lower concentration than under fully-supplemented medium conditions. It has already been mentioned that nanoparticles lower their surface free energy via strong non-specific interaction with cell membranes. However, the amount of free energy is lowered by the presence of a protein corona and both the degree of adhesion to the membrane and cell uptake are reduced.[41,42] Thus the observed effect of proteins bound to SiQDs inducing a delay in the onset of cytotoxic effects is not surprising and is in agreement with previous observations.[43,44]

SiQD 1100 were detected within the cells under both test conditions – both with and without proteins originating from FBS; however, it was found that without proteins they enter the cells more rapidly, are distributed diffusely and have a stronger negative effect on metabolic activity. On the other hand, SiQD 1050 were not detected in the cells by means of fluorescence microscopy under either of the test conditions; however, the cytotoxic effect thereof was determined (Figure 8b) which may indicate their entry into the cells. Moreover, the cytotoxic effect was found to be stronger under non-FBS protein presence conditions. This may imply the easier cell entry of SiQD 1050 without a protein corona. However, they were not observable via fluorescence microscopy images. We suspect, as PL aging studies suggest (Figure 2c), that the PL of these SiQDs degrades to a significant extent in aqueous media (i.e. in the natural biological experiment environment). Moreover, it should be noted that SiQD 1050 exhibit three times lower PL EQY and a slightly lower absorption cross-section, which renders them more difficult to observe by means of fluorescence microscopy (Figure 6b, d).

The formation and structure of the protein corona is crucial in terms of the fate of all nanoparticles located in living organisms as has been demonstrated by a large number of previous studies.[13,35,36,45] Bare nanoparticles are unable to survive within a biological system since they are immediately covered by a layer of proteins from the fluid which forms the hard protein corona and which continues to grow until they attain a stable state, which is often a long-term process as observed in the case of SiQD 1050. Experiments conducted prior to *in vivo* application should always mimic the environment of the organism as precisely as possible. *In vitro* dose-dependent tests of nanoparticles should be performed using biological fluids only before forming conclusions on the

View Article Online
DOI: 10.1039/C6RA14430F



cytotoxicity of the material. As was apparent especially in the case of SiQD 1050, the presence of bare SiQDs or protein-coated SiQDs in the cell culture makes a huge difference in terms of cytotoxicity and the immense aggregation of SiQD 1050 with proteins leads to fatal consequences for organisms.

## 4 Conclusion

We attempted to demonstrate to what extent novel co-doped SiQDs react upon being introduced into a natural biological environment consisting of human osteoblasts and a cell culture medium with or without the addition of fetal bovine serum. A series of experiments was conducted at various concentration levels of two types of SiQD (1100 and 1050), an evaluation was made of their cytotoxicity and their localization within the cell culture was assessed by means of fluorescence wide-field and confocal microscopy.

The detailed luminescence characterization of the SiQDs in colloidal suspensions at different times following fabrication as well as of the SiQDs inside cell cultures and water-based media enabled the research team to uncover the continuous changes which took place due to the aging of the SiQDs (a shift in the PL peak to shorter wavelengths and related EQY changes, Figure 2). A detailed knowledge of PL aging allowed us to select the optimum type of SiQD (i.e. SiQD 1100) for fluorescence imaging purposes in cells with an optimal PL peak of around 750 nm and an EQY ensemble of 12%.

Zeta potential measurement indicated that the tested SiQDs differ from each other not only in terms of their size and PL properties but also with respect to zeta potential values. Consequently, the formation of a protein corona differs on the surface of SiQDs, which affects the reaction with the biological components of the cell culture medium and overall cytotoxicity. SiQD 1050 in particular were almost completely entrapped within growing aggregates of proteins which hindered their access into the cells which, in turn, led to the cytotoxicity of SiQD 1050 appearing to be relatively low. However, the real extent of cytotoxicity was revealed under serum-free conditions indicating that a high amount of SiQD 1050 enter cells despite the fact that they become undetectable by fluorescence microscopes (due to a PL shift to shorter wavelengths with strong cell autofluorescence and the degradation of PL yield). On the other hand, SiQD 1100 exhibited a low level of interaction with proteins which enabled cell incorporation even in the serum-supplemented medium. Thus, these particles are able to enter cells in the bare state as well as with the addition of a protein corona although in all probability the pathways used differ.

The results provide important findings concerning the in vitro toxicity of novel co-doped SiQDs and enhance our understanding of the complexity of processes acting between SiQDs and biological environments.

View Article Online
DOI: 10.1039/C6RA14430F



## Acknowledgements

This study was supported by the project LH14246 Kontakt II of Ministry of Education, Youth and Sports of the Czech Republic and by the Visegrad Group (V4)-Japan Joint Research Program on Advanced Materials (project NaMSeN) and by the project of National Sustainability Program I No. LO1503. This study was also supported by Charles University in Prague, First Faculty of Medicine (project PRVOUKP24/LF1/3) and Faculty of Medicine in Pilsen (SVV 260 279/2016).

## References

1 K. K. Qian and H. R. Bogner, *J. Pharm. Sci.*, 2012, **101**, 444 – 463.
2 E. J. Anglin, M. P. Schwartz, V. P. Ng, L. a. Perelman and M. J. Sailor, *Langmuir*, 2004, **20**, 11264–11269.
3 F. Erogbogbo, K.-T. Yong, I. Roy, G. Xu, P. N. Prasad and M. T. Swihart, *ACS Nano*, 2008, **2**, 873–878.
4 Y. Zhong, X. Sun, S. Wang, F. Peng, F. Bao, Y. Su, Y. Li, S.-T. Lee and Y. He, *ACS Nano*, 2015, **9**, 5958–5967.
5 X. Pi, T. Yu and D. Yang, *Part. Part. Syst. Charact.*, 2014, **31**, 751–756.
6 S. E. a Gratton, P. a Ropp, P. D. Pohlhaus, J. C. Luft, V. J. Madden, M. E. Napier and J. M. DeSimone, *Proc. Natl. Acad. Sci. U. S. A.*, 2008, **105**, 11613–11618.
7 Yang X., Liu J., He H., Zhou L., Gong C., Wang X., Yang L., Yuan J., Huang H. and He L., *Part Fibre Toxicol*, 2010, **7**, 1–12.
8 H. Liang, C. Jin, Y. Tang, F. Wang, C. Ma and Y. Yang, *J. Appl. Toxicol.*, 2014, **34**, 367–372.
9 J. Kim, H. Kim and M. Kim, 2014, **9**, 235–241.
10 S. Bhattacharjee, L. H. J. de Haan, N. M. Evers, X. Jiang, A. T. M. Marcelis, H. Zuilhof, I. M. C. M. Rietjens and G. M. Alink, *Part. Fibre Toxicol.*, 2010, **7**, 25.
11 S. Bhattacharjee, I. M. C. M. Rietjens, M. P. Singh, T. M. Atkins, T. K. Purkait, Z. Xu, S. Regli, A. Shukaliak, R. J. Clark, B. S. Mitchell, G. M. Alink, A. T. M. Marcelis, M. J. Fink, J. G. C. Veinot, S. M. Kauzlarich and H. Zuilhof, *Nanoscale*, 2013, **5**, 4870–83.
12 H. Herd, N. Daum, A. T. Jones, H. Huwer, H. Ghandehari and C.-M. Lehr, *ACS Nano*, 2013, **7**, 1961–1973.
13 M. Cui, R. Liu, Z. Deng, G. Ge, Y. Liu and L. Xie, *Nano Res.*, 2014, **7**, 345–352.
14 E. Roduner, *Chem. Soc. Rev.*, 2006, **35**, 583–592.
15 A. Lesniak, F. Fenaroli, M. P. Monopoli, C. Åberg, K. a. Dawson and A. Salvati, *ACS Nano*, 2012, **6**, 5845–5857.
16 M. P. Monopoli, C. Aberg, A. Salvati and K. A. Dawson, *Nat Nano*, 2012, **7**, 779–786.
17 M. Hadjidemetriou, Z. Al-Ahmady, M. Mazza, R. F. Collins, K. Dawson and K. Kostarelos, *Acs Nano*, 2015, **9**, 8142–8156.
18 H.-J. Eom and J. Choi, *Environ. Health Toxicol.*, 2011, **26**, e2011013.
19 S. W. Ha, J. A. Sikorski, M. N. Weitzmann and G. R. Beck, *Toxicol. In Vitro*, 2014, **28**, 354–364.
20 J. Kasper, M. I. Hermanns, C. Bantz, S. Utech, O. Koshkina, M. Maskos, C. Brochhausen, C. Pohl, S. Fuchs, R. E. Unger and C. James Kirkpatrick, *Eur. J. Pharm. Biopharm.*, 2013, **84**, 275–287.

View Article Online
DOI: 10.1039/C6RA14430F



21 M. Fukuda, M. Fujii, H. Sugimoto, K. Imakita and S. Hayashi, *Opt. Lett.*, 2011, **36**, 4026–4028.
22 H. Sugimoto, M. Fujii, K. Imakita, S. Hayashi and K. Akamatsu, *J. Phys. Chem. C*, 2012, **116**, 17969–17974.
23 J. Valenta, *Nanosci. Methods*, 2014, **3**, 11–27.
24 J. Valenta, M. Greben, Z. Remeš, S. Gutsch, D. Hiller and M. Zacharias, *Appl. Phys. Lett.*, 2016, **108**, 023102.
25 H. Sugimoto, M. Fujii, K. Imakita, S. Hayashi and K. Akamatsu, *J. Phys. Chem. C*, 2013, **117**, 11850–11857.
26 X. Liu, Y. Zhang, T. Yu, X. Qiao, R. Gresback, X. Pi and D. Yang, *Part. Part. Syst. Charact.*, 2016, **33**, 44–52.
27 E. Flahaut, M. C. Durrieu, M. Remy-Zolghadri, R. Bareille and C. Baquey, *Carbon*, 2006, **44**, 1093–1099.
28 E. Petryayeva, W. R. Algar and I. L. Medintz, *Appl. Spectrosc.*, 2013, **67**, 215–252.
29 R. G. Mendes, B. Koch, A. Bachmatiuk, A. A. El-Gendy, Y. Krupskaya, A. Springer, R. Klingeler, O. Schmidt, B. Büchner, S. Sanchez and M. H. Rümmeli, *Biochim. Biophys. Acta*, 2014, **1840**, 160–169.
30 S. Chen, C. Zhang, G. Jia, J. Duan, S. Wang and J. Zhang, *Mater. Sci. Eng. C*, 2014, **43**, 330–342.
31 W. Zhang, M. Kalive, D. G. Capco and Y. Chen, *Nanotechnology*, 2010, **21**, 355103.
32
33 A. Asati, S. Santra, C. Kaittanis and J. M. Perez, *ACS Nano*, 2010, **4**, 5321–5331.
34 A. M. El Badawy, R. G. Silva, B. Morris, K. G. Scheckel, M. T. Suidan and T. M. Tolaymat, *Environ. Sci. Technol.*, 2011, **45**, 283–287.
35 M. P. Calatayud, B. Sanz, V. Raffa, C. Riggio, M. R. Ibarra and G. F. Goya, *Biomaterials*, 2014, **35**, 6389–6399.
36 W. Jiang, K. Lai, Y. Wu and Z. Gu, *Arch. Pharm. Res.*, 2013, **37**, 129–141.
37 L. W. Zhang and N. A. Monteiro-Riviere, *Toxicol. Sci.*, 2009, **110**, 138–155.
38 S. Ohta, S. Inasawa and Y. Yamaguchi, *Biomaterials*, 2012, **33**, 4639–4645.
39 A. Anas, T. Okuda, N. Kawashima, K. Nakayama, T. Itoh, M. Ishikawa and V. Biju, *ACS Nano*, 2009, **3**, 2419–2429.
40 P. Shen, S. Ohta, S. Inasawa and Y. Yamaguchi, *Chem. Commun.*, 2011, **47**, 8409–8411.
41 A. Lesniak, A. Salvati, M. J. Santos-Martinez, M. W. Radomski, K. A. Dawson and C. Åberg, *J. Am. Chem. Soc.*, 2013, **135**, 1438–1444.
42 P. Foroozandeh and A. A. Aziz, *Nanoscale Res. Lett.*, 2015, **10**.
43 X. Jiang, S. Weise, M. Hafner, C. Röcker, F. Zhang, W. J. Parak and G. U. Nienhaus, *J. R. Soc. Interface R. Soc.*, 2010, **7 Suppl 1**, S5–S13.
44 F. Catalano, L. Accomasso, G. Alberto, C. Gallina, S. Raimondo, S. Geuna, C. Giachino and G. Martra, *Small*, 2015, **11**, 2919–2928.
45 N. A. Monteiro-Riviere, M. E. Samberg, S. J. Oldenburg and J. E. Riviere, *Toxicol. Lett.*, 2013, **220**, 286–293.

View Article Online
DOI: 10.1039/C6RA14430F



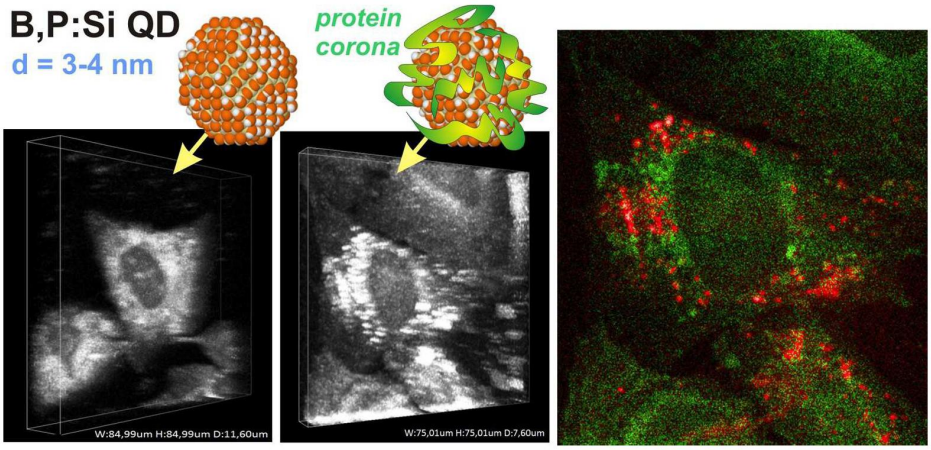


182x86mm (250 x 250 DPI)

## Publication B

**Belinova, Tereza**, Lucie Vrabcova, Iva Machova, Anna Fucikova, Jan Valenta, Hiroshi Sugimoto, Minoru Fujii, and Marie Hubalek Kalbacova. "**Silicon Quantum Dots and Their Impact on Different Human Cells**." physica status solidi (b) 255, no. 10 (2018). IF = 1.729

ORIGINAL PAPER

Group IV-Based Nanostructures

physica status solidi pss b

www.pss-b.com

# Silicon Quantum Dots and Their Impact on Different Human Cells

*Tereza Belinova, Lucie Vrabcova, Iva Machova, Anna Fucikova, Jan Valenta, Hiroshi Sugimoto, Minoru Fujii, and Marie Hubalek Kalbacova**

**Silicon quantum dots (SiQDs) are interesting low-dimensional nanostructures whose unique optical and electronic properties can be exploited for imaging, biosensing, or drug delivery. SiQDs with a diameter of around 4 nm co-doped with boron and phosphorus and evincing fluorescence and dispersibility in aqueous solutions were studied with respect to their impact on different human cells. The level of SiQD cytotoxicity in different types of human cells – osteoblasts, monocytes, macrophages, and mesenchymal stromal cells – was determined. Exposing the cells to increasing concentrations of quantum dots under different conditions and the subsequent evaluation of their cytotoxicity provided an overview of cell-specific reactions to identical doses. The results revealed the importance of cultivation conditions (e.g., the formation of a protein corona on nanoparticles originating from the media supplement) as well as the significant impact of cell type (the increased sensitivity of monocytes to quantum dots in comparison to other cell types).**

## 1. Introduction

Quantum dots (QDs) are used in the field of biology as an alternative to traditional organic dyes due to their high luminescence quantum yields and low photobleaching coefficients.[1,2] Thanks to their optical properties, QDs are particularly suitable for use in single molecule tracking experiments in live cells. However, QDs are mostly made up of heavy metals which can be highly toxic with respect to the biological environment; moreover, this toxicity may influence the results (e.g., the triggering of different reactions such as cell stress resulting in apoptosis (programmed, physiological cell death) or necrosis (accidental, non-physiological cell death). Silicon provides a promising material with respect to QDs due to its high degree of biocompatibility, biodegradability and chemical resistance to pH and temperature changes.[3,4]

Several methods are employed for the introduction of QDs into cells, commonly used is direct addition of QDs to cultivation media *in vitro* or intravenous injection *in vivo*. Particles thus administered firstly interact with the biological environment: *in vitro* – interaction with the various components of the cultivation medium (fetal bovine serum (FBS) as a supplement and a source of proteins, aminoacids, etc.); *in vivo* – interaction with body fluids (plasma as an important component) – prior to coming into contact with the cells. Interaction with the various components of the biological environment allows the particles to acquire a so-called biomolecular corona, that is a layer of molecules (e.g., proteins, lipids, etc.) extracted from the environment that bind to the particles in dependence on their physico-chemical properties (zeta potential, surface termination, shape etc.).[5,6] This layer then provides the "new surface" of particles with an identity which is responsible for cell interaction. By altering the conditions under which QDs are introduced to the cells, it is possible to alter the way in which cells interact with the QDs and so modulate the results.[7] Moreover, biomolecular corona may not only modify the way of cell-nanoparticle interaction but also can cause quenching or enhancing of QDs fluorescence.[8,9]

The cells used in this study consisted primarily of stable cell lines (SAOS-2 human osteoblast cell line and THP-1 human monocytic cell line) and primary cells (hMSCs – human mesenchymal stem cells). SAOS-2 cells were used due to their well-described properties and behavior. The monocytic cell line was employed since, if one considers real application in the field of human medicine, immune cells will be the first cells to interact with the particles. Moreover, this cell line can be used in two stages – suspension monocytes and adherent macrophages.

T. Belinova, L. Vrabcova, Dr. I. Machova, Prof. M. Hubalek Kalbacova
Faculty of Medicine in Pilsen
Biomedical Center
Charles University
Pilsen, Czech Republic
E-mail: marie.kalbacova@lf1.cuni.cz

Dr. A. Fucikova, Prof. J. Valenta
Faculty of Mathematics and Physics
Department of Chemical Physics and Optics
Prague, Czech Republic

Dr. H. Sugimoto, Prof. M. Fujii
Department of Electrical and Electronic Engineering
Graduate School of Engineering
Kobe, Japan

Prof. M. Hubalek Kalbacova
1st Faculty of Medicine
Institute of Pathological Physiology
Charles University
Pilsen, Czech Republic

The ORCID identification number(s) for the author(s) of this article can be found under https://doi.org/10.1002/pssb.201700597.

**DOI: 10.1002/pssb.201700597**

 

Healthy mesenchymal stem cells were then used to test the reaction of primary cells, as opposed to stable lines that are derived from cancerous cells.

This study involved the testing of silicon-based quantum dots co-doped with phosphorus and boron on several types of human cells (monocytes, macrophages, osteoblasts and mesenchymal stem cells) in order to determine their influence on cellular viability (metabolic activity and necrosis detection) and, possibly, the mechanism behind this influence. In addition, the biomolecular corona variable was studied and its importance subsequently proved.

## 2. Results and Discussion

### 2.1. SiQDs

**Figure 1**a depicts a transmission electron microscope (TEM) image of SiQDs placed on a carbon-coated TEM mesh. The QDs were perfectly dispersed throughout the methanol and, thus, no agglomerates are evident in the TEM image. The average diameter of the QDs is 3.9 nm. The lattice fringe visible in the high-resolution TEM image in the inset corresponds to {111} plan of Si crystal. Figure 1b shows the PL spectrum of a methanol solution of SiQDs excited at 405 nm; broad luminescence is observed around 740 nm. This wavelength lies within the near-infrared window in biological tissue and is suitable for bio-imaging. The luminescence peak wavelength is slightly longer than that commonly reported for undoped SiQDs with comparable sizes.[7,10,11]

### 2.2. Cytotoxicity Experiments

#### *2.2.1. Determination of Metabolic Activity*

Metabolic activity reflects the activity of mitochondria, which in other words, reflects cell viability. Different types of cells (osteoblasts, monocytes, macrophages, and human mesenchymal stem cells) were incubated with SiQDs over differing time intervals (6, 24 and 48 h) following which their metabolic activity was measured. The used SiQD concentrations were selected on the basis of our previous study with similar SiQDs.[7] Incubation was performed under standard cultivation conditions (the medium plus 5% FBS) and non-standard conditions (no FBS presence in the first 6 h of incubation) aimed at preventing the formation of biomolecular coronas on the SiQDs – the interaction of the cells with "naked" nanoparticles.

The metabolic activity of osteoblasts (SAOS-2) decreased over time with respect only to the highest concentration of SiQD applied (100 $\mu g\,ml^{-1}$) under standard conditions (**Figure 2**a), and the cytotoxic level (75% of control) was attained as early as following 6 h of incubation.[12] Under non-standard conditions, a decrease in cell metabolic activity was also evident with concern to those cells incubated with 50 $\mu g\,ml^{-1}$ SiQD for 48 h (Figure 2b). The difference between the cell reactions to SiQD under differing conditions might be explained by the presence of biomolecular corona on those SiQD cultivated under standard conditions altering, and possibly preventing, the entering of the particles into the cells and the consequent disruption of cell processes or organelles.[13]

On the other hand, the metabolic activity of hMSCs was comparable to or slightly less than that of the control cells; however, in neither case did they reach cytotoxic levels (Figure 2c,d). Thus, no effects stemming from the formation of biomolecular corona were apparent with respect to these primary cells following 24 h of incubation.

An evaluation of the effect of SiQDs with the immune cell line (THP-1) was conducted employing the two forms thereof, that is a suspension of monocytes (cells freely circulating in blood) and adherent macrophages (cells activated by for example pathogens).

The SiQDs had no impact on monocyte metabolic activity under standard cultivation conditions (Figure 2e); indeed, they even appeared to stimulate the cells within the first 6 h of cultivation. After 24 h under non-standard conditions, however, the cellular metabolic activity decreased to below a cytotoxic level of 75% with concern to both the 50 and 100 $\mu g\,ml^{-1}$ concentrations (Figure 2f) which shows that the presence of corona-forming molecules within the first few hours of incubation is crucial in terms of the fate of such cells. It is apparent that "naked" SiQDs damage monocytes in a concentration-dependent manner. Surprisingly, the significant activation of monocytes' metabolic activity was observed after 6 h, especially under standard cultivation conditions, which may be connected with the commencement of an inflammatory response; however, this supposition must be subjected to further testing.

The adherent-type immune cells – macrophages – exhibited very similar results to those of the suspension monocytes. No reaction to SiQD presence was observed under standard cultivation conditions; however, a decrease was evident in metabolic activity after 24 h under non-standard conditions (Figure 2g,h). The reaction under non-standard conditions was more drastic than in the case of the monocytes, that is even the lowest concentration of SiQDs decreased metabolic activity to below the cytotoxic level. Interestingly, the decrease was not concentration-dependent.

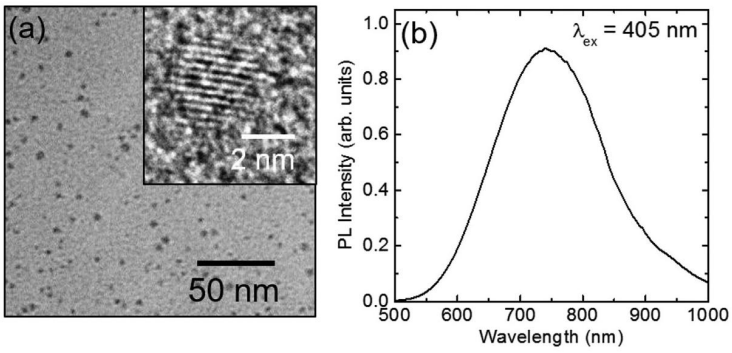


**Figure 1.** a) Transmission electron microscope (TEM) image of SiQDs. Inset: High resolution TEM image of a Si QD. b) Photoluminescence spectrum of Si QDs excited at 405 nm.

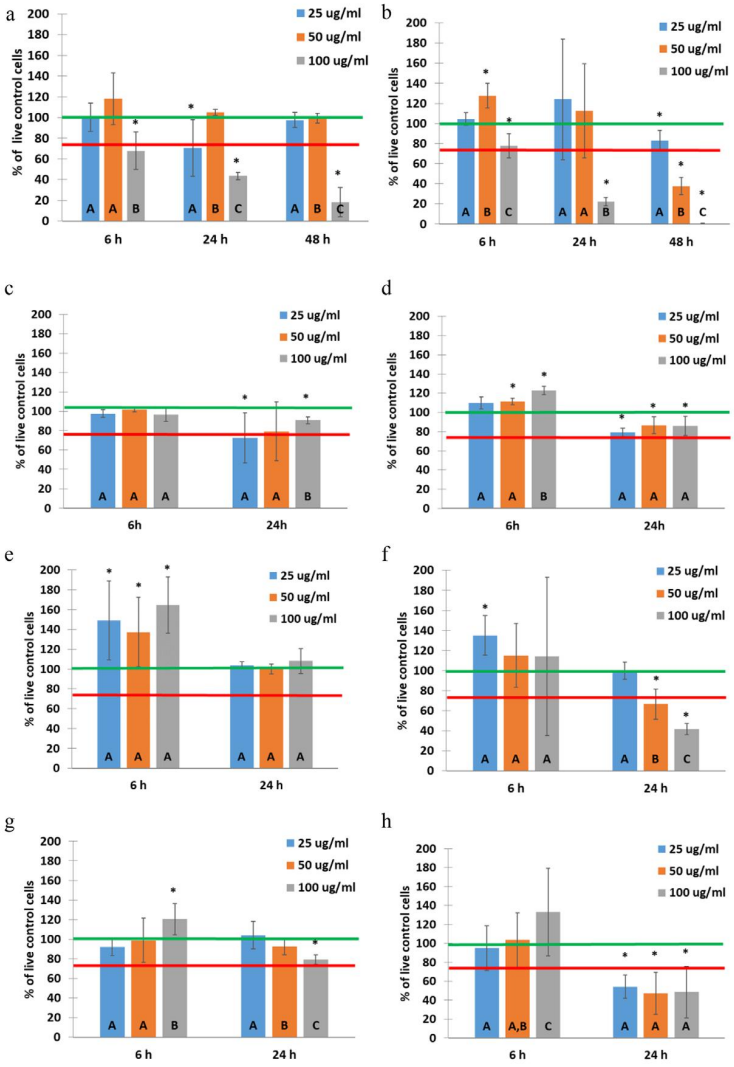


**Figure 2.** Metabolic activity of different cells (a,b) SAOS-2, (c,d) hMSC, (e,f) monocytes THP-1 and (g,h) macrophages THP-1, incubated with SiQD under standard (with FBS – a, c, e, g) and non-standard conditions (without FBS – b, d, f, h). Relative values are expressed as a percentage of control sample (untreated cells in adequate cultivation medium). The star symbol (*) highlights a significant difference from the control in cultivation medium with 5% FBS (Wilcoxon matched-pairs test, $p < 0.05$). Letters (A, B, C) represent grouping according to statistical similarity of the values within one time point (ANNOVA, Fischer LSD test). Green line shows 100% of control (live cells). Red line shows 75% of control (cytotoxicity level).

The presence or absence of FBS in the cultivation medium proved to be a key factor in terms of influencing SiQD-induced metabolic activity. As can be seen in Figure 2, practically no reaction can be observed with concern to most of the tested cell types under standard cultivation conditions in cases where a biomolecular corona is present. Under non-standard conditions, the situation changed, that is the reaction of the cells was very much dependent on cell type. The primary hMSCs evinced no significant reaction to these SiQDs; however, the stable cell lines (THP-1 and SAOS-2) responded to the presence of SiQDs after 24 h with a decrease in metabolic activity. This discrepancy may be due to the fact that immortalized cell lines are of cancerous origin and thus have different properties to primary mesenchymal stem cells extracted from healthy donors. Our results confirm that the biomolecular corona exerts a significant impact on the cytotoxicity of nanoparticles.[7,14]

### 2.2.2. Determination of Cell Death (Necrosis)

In order to determine the mechanism of the reduction effect of SiQDs on metabolic activity, the presence of lactate dehydrogenase (LDH) in the supernatants of osteoblasts and hMSCs was examined (**Figure 3**). LDH is an enzyme present inside all living cells and is detectable in the culture media only when cellular membrane is disrupted, which is typical hallmark of necrosis (accidental cell death). For positive control, the cells were killed using 10% Triton X and the level of detected LDH was set at 100% (black column). Untreated cells were used for the negative control (green column). With concern to the SAOS-2 cells, a certain level of LDH was detectable in all the samples; while a significant increase was detected in comparison to the negative control regarding only the highest concentration (100 μg ml$^{-1}$) after 48 h under standard conditions and at the same concentration, it occurred significantly earlier (24 h) under non-standard conditions. A comparison of the results from metabolic activity of these cells (Figure 2a,b) with those of LDH led to an interesting discovery. Even though metabolic activity decreased significantly with the highest SiQD concentration after 24 h under both conditions, the level of detected LDH proved that no necrosis occurred. The results obtained under non-standard conditions after 48 h subsequently showed a decrease in metabolic activity as well as high levels of LDH in the cell supernatant. Therefore, it might be concluded that the cells were significantly stressed and underwent apoptosis after 24 h of incubation, but that after 48 h, necrosis provided the metabolic activity decrease mechanism.

Napierska et al. stated that small nanoparticles (under 15 nm in diameter) rapidly affect cellular viability.[15] In our case, however, it seems that the cells initially attempt to "deal with" the particles, but that after longer periods, their toxic impact under non-standard conditions leads to sudden necrotic death.

Only a very low level of LDH comparable with that of the healthy non-treated control was detected in hMSCs (Figure 3c,d). The slight decrease in the metabolic activity of hMSCs and the lack of an increase in the LDH level above the negative control implies that the mechanism of the SiQD effect most probably consists of apoptosis rather than necrosis. Apoptosis induced by silicon-based nanoparticles has been reported previously; thus, this mechanism should be subjected to further study.[16,17]

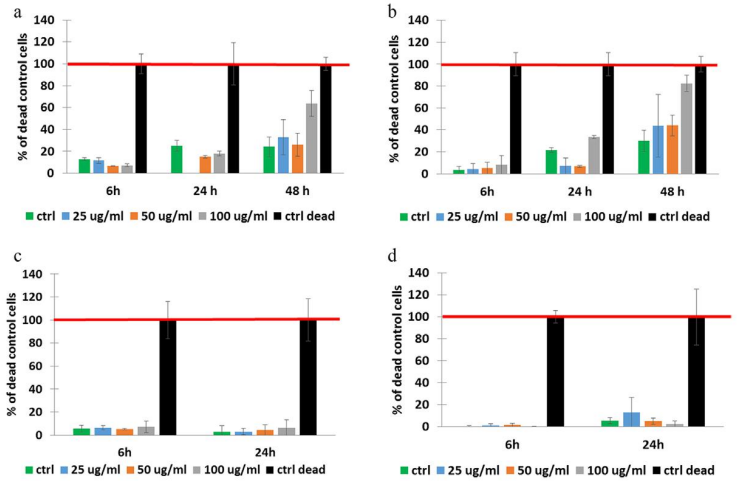


**Figure 3.** Determination of lactate dehydrogenase activity in cell supernatants indicating necrosis. SAOS-2 (a) and hMSC (c) cells with SiQD under standard conditions, SAOS-2 (b) and hMSC (d) under non-standard conditions. Relative values are expressed as a percentage of positive control sample (CTRL dead – cells killed within Triton X). Red line shows 100 % necrosis.

The possible apoptotic cell death caused by the cultivation of cells with SiQDs is supported by the microscopic observation of hMSCs cultivated under non-standard conditions (**Figure 4**). Their morphology apparently changed in relation to increasing concentrations of SiQDs. With respect to the highest SiQD concentration, the cells were present in comparable amounts to the control cells but were shrunken. The observed morphology is commonly known to be related to cellular stress, which, however, was not reflected in terms of metabolic activity. Thus, it might be speculated that the morphology changes may represent the display of the early stage of apoptosis, which is not detectable via methods employed to date. Further experiments are currently underway aimed at proving this supposition.

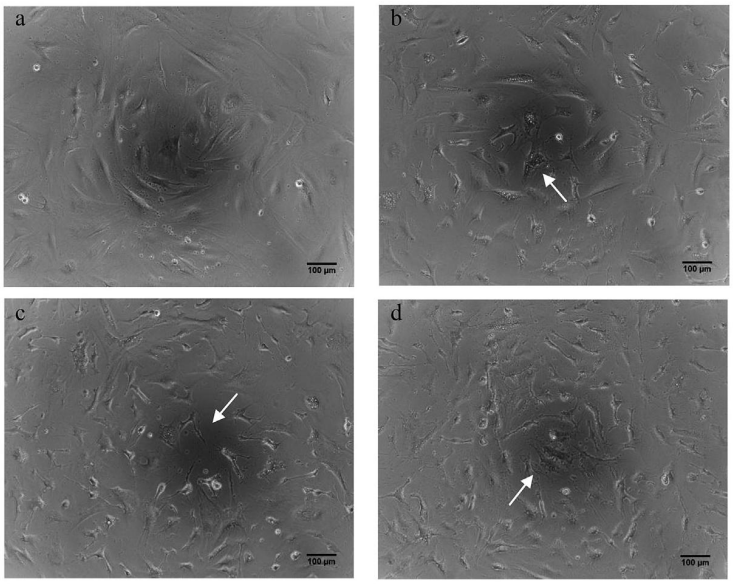


**Figure 4.** Bright field phase-contrast images of hMSC cells after 24 h in non-standard conditions (without FBS). a) Control cells without SiQDs, b) 25 µg ml$^{-1}$ SiQDs, c) 50 µg ml$^{-1}$ SiQDs, d) 100 µg ml$^{-1}$ SiQDs. Arrows mark distinctive changes in cellular morphology.

## 3. Conclusion

The results presented herein provide an interesting overview of the impact of P and B co-doped SiQD on different types of human cells. The importance of the biomolecular corona was demonstrated for all the cell types employed except for hMSCs. The absence of a biomolecular corona led to a significant decrease in cellular metabolic activity. The mechanism of this influence is not yet clear; however, the results obtained imply that cells may undergo apoptosis. Further research will focus on both the specific mechanisms involved in apoptosis induction and on inflammatory response activation of immune cells. The results provide a general insight into the potential biomedical application of these quantum dots.

## 4. Experimental Section

*SiQDs Preparation and Characterization*: The SiQDs co-doped with phosphorus and boron were prepared by means of previously reported technique.[10,18,19] Co-doped SiQDs can be dispersed in polar solvents (water, alcohol) due to the negative surface potential (zeta potential: −50 mV) induced in the highly phosphorus and boron co-doped surface, and they exhibit bright size-controllable luminescence in water over a wide pH range. The surface of co-doped SiQDs immediately following preparation is hydrogen-terminated and slowly oxidizes during storage in the solution, thus the SiQDs were stored in methanol for more than 30 days prior to use to replace completely of surface hydrogen atoms with oxygen atoms and rendered the surface inactive. This replacement was previously confirmed by FT-IR data that showed almost complete absence of hydrogen atoms on the surface.[20]

The TEM observation of SiQDs was performed using JEM-2100F electron microscope (JEOL Ltd.) operated at 200 kV. The SiQD solution was drop-casted on a carbon coated TEM mesh in order to obtain viewable sample. The PL spectra were excited by monochromatized Xenon lamp at 405 nm. Detection was performed by photomultiplier at 500–850 nm and an InGaAs photodiode at 800–1400 nm using spectrophotometer (Fluorolog-3, HORIBA Jobin Yvon).

*Cultivation Conditions*: SAOS-2 osteoblastic cell line (DSMZ, Germany) was seeded at a concentration of 10 000 cells cm$^{-2}$ in McCoy's 5A medium (GE Healthcare – HyClone) supplemented with 15% FBS (Biosera), L-glutamine (Life technologies), 10 000 U ml$^{-1}$ penicillin and 10 µg ml$^{-1}$ streptomycin (both Sigma-Aldrich).

Human MSC obtained from bone marrow blood aspirated from the posterior iliac crest from healthy donors after they had provided informed, written consent, were seeded at the same concentration in alpha-MEM with phenol red (Thermo Fischer Scientific), L-glutamine (Life

Technologies) and 10 000 U ml$^{-1}$ penicillin and 10 µg ml$^{-1}$ streptomycin (both Sigma-Aldrich) and supplemented with 10% FBS (Biosera).

A human monocytic cell line THP-1 (suspension monocytes) was seeded at a concentration of 25 000 cells cm$^{-2}$ in RPMI 1640 medium (Biowest) supplemented with 10% FBS (Biosera), L-glutamine (Life Technologies), 10 000 U ml$^{-1}$ penicillin and 10 µg ml$^{-1}$ streptomycin (both Sigma-Aldrich). In order to obtain adherent macrophages, 160 000 cells cm$^{-2}$ of monocytic THP-1 was seeded on 6-well plate (Techno Plastic Products) and cultivated for 72 h in a standard cultivation medium additionally supplemented with 100 nM phorbol 12-myristate13-acetate (PMA, Sigma-Aldrich). Following the subsequent stimulation, the macrophages were seeded at a concentration of 25 000 cells cm$^{-2}$.

The cells were pre-cultivated on 96-well plates in a $CO_2$ incubator at 37 °C for 24 h, then they were washed with pre-warmed phosphate buffer saline (PBS, Thermo Fisher Scientific – Gibco) and the SiQDs were added.

Particles provided in methanol were mixed with deionized water and placed in a dry bath at 70 °C to allow for the evaporation of the methanol and thus form an aqueous stock for immediate usage. The stock particles were diluted in the appropriate cultivation medium (DMEM for SAOS-2 cells, alpha-MEM for hMSCs and RPMI for THP-1 cells) supplemented with 5% FBS (or not supplemented) and added to the cells for 6, 24 and 48 h. After 6 h, FBS was added to the non-supplemented wells so as to attain a final concentration of 5% FBS aimed at avoiding cell inhibition and damage due to a lack of nutrients.

*Metabolic Activity Measurements*: Colorimetric assay (MTS, Cell Titer96® AqueousOne, Promega) based on the reduction of tetrazolium in metabolically active cells to formazan was used to establish metabolic activity. After 6, 24 and 48 h, the supernatant was stored at −20 °C for the subsequent determination of LDH. The cells were washed with PBS followed by the addition of 10% MTS solution in the corresponding media. In the case of the THP-1 cell suspension, the MTS was added directly to the samples to form a 10% solution inside the plate. Optical density was measured by means of a microplate reader (Synergy 2, BioTek Instruments, Inc.) at 490 nm, subtracting the background at 655 nm. The values obtained were related to the corresponding controls (non-treated cells) in terms of percentage.

*Microscopy Observations*: Bright field phase-contrast images for the visual evaluation of cellular conditions were acquired using a Nikon Eclipse Ti-S with a Nikon DS-Qi1Mc camera and a Nikon Plan Fluor 10x Ph1 DL objective.

*Detection of Necrosis*: A Cytotoxicity Detection Kit (LDH, Roche applied sciences) was used for the determination of the lactate dehydrogenase activity of the cell supernatants (markers of disrupted cell membranes and cell death) according to the manufacturer's instructions. Optical density was measured using a microplate reader (Synergy 2, BioTek Instruments, Inc.) at 490 nm, subtracting the background at 600 nm. The values obtained were related to the corresponding controls (the positive control was acquired *via* treatment with 10% Triton X (Sigma Aldrich) – dead cells).

*Statistical Analysis*: The data presents the means of all the experiments with error bars representing standard deviations. The non-parametric Wilcoxon matched pairs test and ANOVA (Fischer LSD test) were used for significance determination (P value of 0.05 and less) and grouping respectively. The statistical analysis was performed using STATISTICA software (StatSoft, Inc.).

## Acknowledgements

This study was supported by the V4J Joint Research Program Nr. 8F15001, by the project of National Sustainability Program I No. LO1503, both provided by Ministry of Education, Youth and Sports of the Czech Republic and by PROGRES Q26 and SVV 260390 provided by Charles University. This study is also partly supported by JSPS KAKENHI Grant Number 16H03828.

## Conflict of Interest

The authors declare no conflict of interest.

## Keywords

cytotoxicity, necrosis, quantum dots, silicon

Received: October 27, 2017
Revised: March 9, 2018
Published online: April 3, 2018

[1] J. Li, J.-J. Zhu, *Analyst* **2013**, *138*, 2506.
[2] A. Valizadeh, H. Mikaeili, M. Samiei, S. M. Farkhani, N. Zarghami, *Nanoscale Res. Lett.* **2012**, *7*, 1.
[3] E. J. Anglin, M. P. Schwartz, V. P. Ng, L. a. Perelman, M. J. Sailor, *Langmuir* **2004**, *20*, 11264.
[4] I. I. Slowing, J. L. Vivero-Escoto, C.-W. Wu, V. S.-Y. Lin, *Adv. Drug Deliv. Rev.* **2008**, *60*, 1278.
[5] M. P. Monopoli, C. Aberg, A. Salvati, K. A. Dawson, *Nat. Nanotechnol.* **2012**, *7*, 779.
[6] E. Casals, V. F. Puntes, *Nanomedicine (Lond.)* **2012**, *7*, 1917.
[7] L. Ostrovska, A. Broz, A. Fucikova, T. Belinova, H. Sugimoto, T. Kanno, M. Fujii, J. Valenta, M. H. Kalbacova, *RSC Adv.* **2016**, *6*, 63403.
[8] L. Shang, G. U. Nienhaus, *Mater. Today* **2013**, *16*, 58.
[9] M. M. Yallapu, N. Chauhan, S. F. Othman, V. Khalilzad-sharghi, C. Ebeling, S. Khan, M. Jaggi, S. C. Chauhan, *Biomaterials* **2015**, *46*, 1.
[10] H. Sugimoto, M. Fujii, K. Imakita, S. Hayashi, K. Akamatsu, *J. Phys. Chem. C* **2013**, *117*, 11850.
[11] M. Fujii, H. Sugimoto, K. Imakita, *Nanotechnology* **2016**, *27*, 262001.
[12] E. Flahaut, M. C. Durrieu, M. Remy-Zolghadri, R. Bareille, C. Baquey, *Carbon (N.Y.)* **2006**, *44*, 1093.
[13] G. Caracciolo, S. Palchetti, V. Colapicchioni, L. Digiacomo, D. Pozzi, A. L. Capriotti, G. La Barbera, A. Lagan, *Langmuir* **2015**, *31*, 10764.
[14] A. Lesniak, F. Fenaroli, M. P. Monopoli, C. Åberg, K. A. Dawson, A. Salvati, *ACS Nano* **2012**, *6*, 5845.
[15] D. Napierska, L. C. J. Thomassen, V. Rabolli, D. Lison, L. Gonzalez, M. Kirsch-volders, J. A. Martens, P. H. Hoet, *Small* **2009**, *5*, 846.
[16] J. S. Nowak, D. Mehn, P. Nativo, C. P. García, S. Gioria, I. Ojea-jiménez, D. Gilliland, *Toxicol. Lett.* **2014**, *224*, 84.
[17] Y. Wu, W. Tang, P. Wang, C. Liu, Y. Yuan, J. Qian, *Part. Part. Syst. Charact.* **2015**, *32*, 779.
[18] M. Fujii, H. Sugimoto, K. Imakita, *Nanotechnology* **2016**, *27*, 262001.
[19] H. Sugimoto, M. Fujii, K. Imakita, S. Hayashi, K. Akamatsu, *J. Phys. Chem. C* **2013**, *117*, 6807.
[20] T. Kojima, H. Sugimoto, M. Fujii, *J. Phys. Chem. C* **2018**, *122*, 1874.

**Publication C**

**Bělinová, Tereza**, Iva Machová, David Beke, Anna Fučíková, Adam Gali, Zuzana Humlová, Jan Valenta, and Marie Hubálek Kalbáčová. "**Immunomodulatory Potential of Differently-Terminated Ultra-Small Silicon Carbide Nanoparticles.**" Nanomaterials 10, no. 3 (2020), IF = 4.324

*nanomaterials*

MDPI

*Article*

# Immunomodulatory Potential of Differently-Terminated Ultra-Small Silicon Carbide Nanoparticles

**Tereza Bělinová [1], Iva Machová [1], David Beke [2,3], Anna Fučíková [4], Adam Gali [2,3], Zuzana Humlová [5], Jan Valenta [4] and Marie Hubálek Kalbáčová [1,5,*]**

1 Biomedical Center, Faculty of Medicine in Pilsen, Charles University, 323 00 Pilsen, Czech Republic; tereza.belinova@lfp.cuni.cz (T.B.); iva.machova@lfp.cuni.cz (I.M.)
2 Wigner Research Centre for Physics, 1121 Budapest, Hungary; beke.david@wigner.mta.hu (D.B.); gali.adam@wigner.mta.hu (A.G.)
3 Department of Atomic Physics, Budapest University of Technology and Economics, 1111 Budapest, Hungary
4 Department of Chemical Physics and Optics, Faculty of Mathematics and Physics, Charles University, 121 16 Prague, Czech Republic; anna.fucikova@email.cz (A.F.); jan.valenta@mff.cuni.cz (J.V.)
5 Institute of Pathological Physiology, 1st Faculty of Medicine, Charles University, 128 53 Prague, Czech Republic; zuzana.humlova@lf1.cuni.cz
* Correspondence: marie.kalbacova@lf1.cuni.cz

Received: 2 March 2020; Accepted: 19 March 2020; Published: 22 March 2020


**Abstract:** Ultra-small nanoparticles with sizes comparable to those of pores in the cellular membrane possess significant potential for application in the field of biomedicine. Silicon carbide ultra-small nanoparticles with varying surface termination were tested for the biological system represented by different human cells (using a human osteoblastic cell line as the reference system and a monocyte/macrophage cell line as immune cells). The three tested nanoparticle surface terminations resulted in the observation of different effects on cell metabolic activity. These effects were mostly noticeable in cases of monocytic cells, where each type of particle caused a completely different response ('as-prepared' particles, i.e., were highly cytotoxic, –OH terminated particles slightly increased the metabolic activity, while $–NH_2$ terminated particles caused an almost doubled metabolic activity) after 24 h of incubation. Subsequently, the release of cytokines from such treated monocytes and their differentiation into activated cells was determined. The results revealed the potential modulation of immune cell behavior following stimulation with particular ultra-small nanoparticles, thus opening up new fields for novel silicon carbide nanoparticle biomedical applications.

**Keywords:** nanoparticles; silicon carbide; cytotoxicity; immune cells; osteoblasts

## 1. Introduction

The knowledge of nanoparticles (NPs) and their potential application in the field of biomedicine as drug delivery [1,2], therapeutic [3–5], and diagnostic platforms and imaging devices [6] have improved significantly over recent years. While particles of different materials and sizes have been studied in detail, only a limited numbers of studies on ultra-small NPs, with sizes of less than 5 nm, have been reported [7–9]. Ultra-small silicon carbide NPs, the study of which remains exceptional, are particularly interesting not only due to their biocompatibility and biodegradability [10–12] but also due to their extremely small size (approximately 4 nm). The potential use of such particles in biomedicine is, however, only partially understood; only a small number of isolated studies taking advantage of their natural fluorescence have been conducted to date [11,13,14]. Moreover, the differing surface termination

of otherwise identical NPs is of particular interest due to the potential for further modification and cluster formation as well as in terms of their influence on the overall cellular response [15–18].

As soon as any NP is administered into a biological fluid (a cultivation medium in vitro or blood in vivo), the particles form a new identity from the various components of the surrounding environment that is widely known as the biomolecular or protein corona (PC) since it is formed by biomolecules and, principally, by proteins [19]. This new identity then serves as a particle-cell interaction mediator [20–22]. While in in vivo experiments the PC is present constantly and changes over time, the interaction of NPs with cells in vitro can also be tested without the PC (incubation in the medium without fetal bovine serum (FBS) supplementation) which may assist in the understanding of the impact of the NP material itself. Naturally, the commonly presented PC concept cannot be applied in the case of ultra-small NPs since they are mostly of the same size or smaller than the individual components (proteins) that usually form the corona; however, their interaction with FBS proteins should not be overlooked [23].

Any application conducted in vivo should be preceded by a complex study of NP–cell interaction in vitro that must not only take into account the response of tissue-specific cells but also include a broader view of the future administration of the particles into living organisms (e.g., ingestion, inhalation, or intravenous application). Regardless of the administration method, immune cells are likely to be the first type of cells to respond to the presence of NPs in the body since their purpose is to find and react with foreign agents. The method used to introduce NPs into the living organism determines the types of immune cells that respond—monocytes (cells freely circulating in the blood), dendritic cells (cells mostly found in diverse epithelia), or macrophages (tissue-specific cells). Numerous studies have been conducted regarding the influence of various NPs on the immune cell metabolism, the mitochondrial state, and overall viability [24,25], as well as their response to allergic and inflammatory reactions [26–28]. Such data is able to assist in both revealing the potential cytotoxicity of NPs and elucidating the mechanisms via which NPs influence cells. Although NPs are viewed primarily as simple carriers, recent studies have reported their immunomodulating properties [5,29–31].

Herein, three size-identical ultra-small silicon carbide (SiC-based) NPs varying only in their surface termination—NPs as prepared (SiC–x), NPs with $NH_2$ groups (SiC–$NH_2$) and NPs with OH groups (SiC–OH) on their surface—were studied in the scope of the biological environment. These NPs are shown to have a different impact on various cell types (osteoblasts, monocytes, and macrophages). Influence on the cellular metabolic activity as well as on the state of mitochondria and production of cytokines in short term cultivation is shown with respect to immune cells, indicating the possibilities for further applications of such NPs and showing the crucial importance of surface termination of such NPs.

## 2. Materials and Methods

### *2.1. Nanoparticle Preparation and Characterization*

SiC nanocrystals were prepared via the wet chemical etching method, as reported previously [32,33]. The particles were then terminated with a variety of oxygen-containing species with a high concentration of carboxyl groups [33]. The preparation of the OH-terminated nanoparticles (SiC–OH) involved the reduction of SiC–x NPs via $NaBH_4$ in an aqueous solution [34]. The SiC–OH were then silanized for the preparation of the SiC–$NH_2$ particles. Briefly, after changing the solvent from deionized water to ethanol with a 1kDa Pall Macrosep ( Pall Co., New York, NY, USA) filter, 10 µL/mL of (APDMES, Sigma-Aldrich, St. Louis, MO, USA) was added to the solution at 40 °C for 2 h. The excess reactant was removed, and the solvent was changed back to DI water with a 1kDa Pall Macrosep filter. Size distribution of NPs was measured by means of atomic force microscopy (AFM, Bruker Dimension Icon atomic force microscope using Bruker (Bruker, Palaiseau, France) Tapping mode and Bruker MPP-11100-10 probe (Bruker, Palaiseau, France), Pall Macrosep). Fourier transform infrared spectra (FTIR) was measured using Bruker Tensor37 (Bruker Co., Billerica, MA, USA) spectrometer equipped with a zinc selenide horizontal multi bounce attenuated total internal reflection accessory, and nuclear magnetic resonance spectra (NMR) was measured using Varian NMR System (Varian, Palo Alto, CA, USA), 600 MHz.

### *2.2. Zeta Potential Determination*

The zeta potential (ζ) of the SiC-based NPs was determined in water (standard solution), DMEM and RPMI 1640 media as well as in both the media with the addition of 5% FBS. The differing NPs in the same amount were pre-incubated overnight in the respective solutions under constant rotation at room temperature (RT). The NPs were centrifuged at 13,000 g for 30 min at RT. The pellet was washed in phosphate buffer saline (PBS) and centrifuged; the process was repeated six times. The final pellet was resuspended in 100 µL of PBS and subsequently diluted with distilled water to achieve a maximal conductivity of 1.5 mS/cm and measured immediately. The ζ was measured using a Zetasizer Nano Series and software Malvern Zetasizer software ver. 7.13 (Malvern Pananalytical Ltd., Malvern, UK).

### *2.3. Cell Culture*

The human osteoblastic cell line (SAOS-2, DSMZ, Braunschweig, Germany) was cultured in McCoy's 5 A medium (GE Healthcare – HyClone, Sigma-Aldrich, St. Louis, MO, USA) supplemented with 15% FBS (Biosera, Nuaille, France), L-glutamine (Life Technologies, Thermo Fischer Scientific, Waltham, MA, USA), 10,000 U/mL of penicillin and 10 µg/mL of streptomycin (both Sigma-Aldrich, St. Louis, MO, USA) in a $CO_2$ humidified incubator at 37 °C. The human monocytic cell line (suspension, THP-1, ATCC) was cultured in RPMI 1640 medium (Biowest, Nuaillé, France) supplemented with 10% FBS (Biosera, Nuaille, France), L-glutamine (Life Technologies, Thermo Fischer Scientific, Waltham, MA, USA), 10,000 U/mL of penicillin and 10 µg/mL of streptomycin (both Sigma-Aldrich, St. Louis, MO, USA). The differentiation of the suspension monocytic THP-1 cells into adherent macrophage-like cells was performed via the following method. The cells were seeded at a concentration of 160,000 cells/cm$^2$ on 6-well plate and cultivated for 72 h in a standard cultivation medium supplemented with 1 µM of phorbol 12-myristate13- acetate (PMA, Sigma-Aldrich, St. Louis, MO, USA). The adherent THP-1 were then trypsinized and used for further experiments. The differentiation of the suspension monocytes into dendritic-like cells was induced via the cultivation of the cells in 2 ml of standard cultivation medium supplemented with 0.1 µg/mL of GM-CSF and 0.1 µg/mL of IL-4 (both Thermo Fischer Scientific, Waltham, MA, USA) for 72 h, whereupon 1 ml of fresh standard cultivation medium supplemented with GM-CSF and IL-4 was added followed by cultivation for further 48 h (5 days of treatment in total).

### *2.4. Metabolic Activity Determination*

The adherent cells were pre-seeded in the respective standard cultivation medium at a concentration of 10,000 cells/cm$^2$ in 96-well plates for 24 h. The cells were then washed with pre-warmed PBS and the NPs (25, 50, and 100 µg/mL) in the corresponding medium (DMEM for SAOS-2 and RPMI 1640 for adherent THP-1), supplemented with 5% FBS or non-FBS-supplemented, were added to the cells; corresponding blanks were also prepared (only the medium with the NPs). After 6 h, the medium with the NPs was replaced with the corresponding NP-free medium supplemented with 5% FBS and cultivation continued up to 24 h. The medium was then discarded and fresh medium with 10% MTS solution was added to the wells. MTS colorimetric assay (Cell Titer961®Aqueous One, Promega, Madison, WI, USA) was used for metabolic activity testing purposes. The optical density was measured (Labsystem Multiskan MS, Vantaa, Finland) at 492 nm and 620 nm as the reference. The corresponding blanks were subtracted and the data was presented as a percentage of the control values (untreated cells).

In the case of the THP-1 suspension (monocytes), the cells were seeded on 96-well U bottom plate at a concentration of 10,000 cells/cm$^2$ in 90 µL of medium supplemented with 5% FBS and with no FBS supplementation. Subsequently, 10 µL of NPs diluted in the corresponding medium were added so as to attain final concentrations of 25, 50, and 100 µg/mL. The cells were incubated in a humidified $CO_2$ incubator at 37 °C on a shaker. After 6 h, the appropriate amount of FBS was added to the non-supplemented wells (non-standard conditions) so as to attain a final concentration of 5% FBS, and the shaker was switched off. With respect to the MTS measurement, the plates were centrifuged (210 g, 5 min, RT) and 50 µL of the supernatant was aspirated and stored in a freezer for further processing

(cytokine detection assay). 50 µL of 20% MTS solution in 5% RPMI was then added so as to attain a final concentration of 10% MTS in the sample. The cells were slightly resuspended and incubated for 2 h in the humidified $CO_2$ incubator at 37 °C. The optical density was measured as described above.

### *2.5. Flow Cytometry Determination of the Cell Number, Mitochondrial Mass, and Potential*

The suspension THP-1 cells were cultured and treated as described above with a volume of 250 µL (8250 cells/well) for the cell number analysis. The 96-well U bottom plate was transferred after the desired incubation time to a flow cytometer (BD FACS Canto, Franklin Lakes, NJ, USA) and the total cell count in a volume of 50 µL was calculated.

The cells were cultured in 6-well plates at a concentration of 10,000 cells/cm$^2$ (without FBS supplementation) with 100 µg/mL of NPs for the detection of the mitochondrial mass and potential. The cells were incubated in the humidified $CO_2$ incubator at 37 °C on a shaker. After 6 h, the appropriate amount of FBS was added so as to attain a final concentration of 5% FBS, and the shaker was switched off; cultivation continued up to 24 h. The cells were then transferred to FACS tubes and stained using MitoTracker™ probes. The mitochondrial mass was detected using MitoTracker™ Green FM (M7514, Invitrogen, Carlsbad, CA, USA) and the mitochondrial potential using MitoTracker™ Red FM (M22425, Invitrogen, Carlsbad, CA, USA). The incubation time of the cells with both probes was 30 min in the humidified $CO_2$ incubator. The positive control (cells with an uncoupled mitochondrial membrane potential) was first treated with 1 mM of carbonyl cyanide-4-(trifluoromethoxy)phenylhydrazone (FCCP, Sigma Aldrich, St. Louis, MO, USA) in the cultivation medium for 30 min in the humidified $CO_2$ incubator at 37 °C and then stained employing the aforementioned procedure. The stained samples were analyzed using flow cytometry (BD FACS Canto, 20,000 cells per sample). The data obtained were processed via FlowJo software (FlowJo LLC, version 10.6.1, Franklin Lakes, NJ, USA ).

### *2.6. Histological Staining for the Morphological Analysis*

The suspension THP-1 cells were seeded at a concentration of 10,000 cells/cm$^2$ in 6-well dishes in RPMI medium with 5% FBS containing 100 µg/mL of particles. The cells were cultured for 4 days, whereupon 0.5 ml of RPMI medium with 50% FBS was added so as to provide sufficient nutrients. The cultivation proceeded for other 3 days. Then the cells remaining in the suspension were spun (300 g, 10 min, RT) and the adherent cells harvested using a standard procedure. All the acquired cells were mixed together, spun (300 g, 10 min, RT) and resuspended in PBS. An approximately 10 µL drop of cell suspension was smeared on a glass slide and allowed to dry. The slides were then fixed in methanol (5 min, RT) and stained employing May–Gründwald–Giemsa–Romanowski staining. The slides were analyzed by means of light microscopy (Olympus IX71, Tokio, Japan) with a color camera (Olympus DP74, 100x UPlanPI objective with oil immersion, Tokio, Japan).

### *2.7. Cytokine Detection*

Supernatants from the metabolic activity tests were used for cytokine detection purposes. The positive control (monocytes stimulated to inflammation) involved the treatment of the cells with lipopolysaccharide (LPS, 50 µg/mL, E. Coli O111:B4, Sigma-Aldrich, St. Louis, MO, USA) in the same manner as the NP-treated cells. A Human Cytokine Antibody Array (ab133997, Abcam, Cambridge, United Kingdom) was used according to the manufacturer's manual. The chemiluminescence data was acquired using the ChemiDoc MP (BioRad) system and the data was processed using ImageLab software (BioRad, version 6.0.1., Hercules, CA, USA). The data were normalized and expressed as a percentage of the untreated control.

### *2.8. Statistical Analysis*

All the data were presented in the form of the means of all the experimental values related to the control from three biologically independent experiments running in duplicate (at least) with error bars representing the standard deviations. The data were statistically processed using Statistica

software (StatSoft Inc., version 12, Tulsa, OK, USA). Remote and outlier values were subtracted based on box graph visualization. The statistical significance against the control was calculated using the non-parametric Wilcoxon matched-pairs test with $p$-values of 0.05 and less.

## 3. Results

### *3.1. Nanoparticle Preparation and Characterization*

The preparation of SiC–x and SiC–OH NPs has been reported previously [32–34]. SiC–$NH_2$ NPs were prepared from SiC–OH NPs via silanization as described in Materials and Methods. Figure 1A shows the infrared spectra of all the SiC-based NPs. In the case of the SiC–x NPs, the majority of the surface groups are carboxyl groups (COOH). Following the elimination of the carboxyl groups using $NaBH_4$, reduction is clearly visible from the disappearance of the peak at 1724 $cm^{-1}$, and the shift and shrinkage of the OH related peak at around 3000 $cm^{-1}$ renders the surface hydroxyl terminated (blue curve—SiC–$NH_2$). The presence of 3-aminopropyl(diethoxy)methylsilane (APDMES) used for the preparation of the SiC–$NH_2$ enhances the C–O–Si related peak at around 1040 $cm^{-1}$. New peaks appear due to the presence of C-C, C-H and N-H bonds at around 1400–1500, 2800–300, and 1550–1650 $cm^{-1}$, respectively.

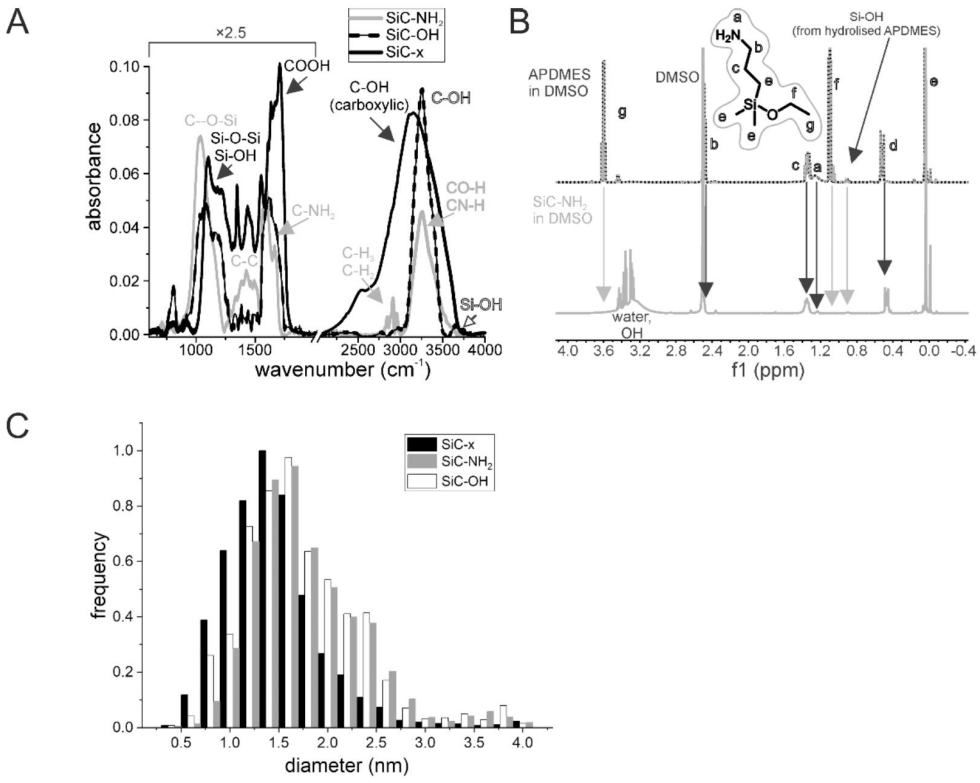


**Figure 1.** Characterization of the SiC-based NPs. The FTIR spectra (**A**) and size distribution (**C**) of the SiC-based NPs with differing surface terminations based on AFM measurement of individual NPs height. The NMR spectra of APDMES and SiC–$NH_2$ (**B**).

Nuclear magnetic resonance (NMR) also indicated the presence of APDMES (Figure 1C). The disappearance of the detectable ethoxy part indicates that all the APDMES hydrolyzed during the reaction, and the lack of the existence of Si–OH groups indicates that the APDMES is linked to the surface. Hydrolyzed but non-linked APDMES has an Si–OH group that was detectable only in the control, i.e., not in the SiC–$NH_2$ NP sample, thus indicating successful surface modification.

Atomic force microscopy (AFM, over 300 particles for each particle type) measurements revealed that the height of SiC-based NPs was under 5 nm (Figure 1B). No significant changes were observed following surface modification, with the exception that the mean size shifted slightly from 1.5 nm to 1.7 and 1.8 nm for the SiC–OH and SiC–$NH_2$ respectively, which was caused by a certain degree of aggregation. Nevertheless, the mean sizes of the SiC-based NPs applied in this study were 1.5 nm, 1.7 nm, and 1.8 nm for the SiC–x, SiC–OH, and SiC–$NH_2$ NPs respectively.

### 3.2. Determination of Zeta Potential in Different Solutions

The behavior of NPs is closely related to their zeta potential (ζ), which reflects the stability of the colloidal suspension of the NPs. By approaching parameter ζ to 0 mV, the colloidal stability worsens, as the NPs attract each other and agglomerate. The NPs used herein were prepared as a stock solution in water and the influence of the biomolecules that originated from the cell cultivation media on the ζ was assessed. Thus, Dulbecco's modified Eagle medium (DMEM) (experimental cultivation medium for osteoblasts) and RPMI 1640 medium (a standard cultivation medium for monocytes/macrophages) were used as appropriate solutions for the estimation of ζ under biological conditions—in particular cases supplemented with FBS. All the NP types in water exhibited approximately the same ζ, i.e. around −35 mV (Figure 2). The transfer of NPs into the cell cultivation media shifted the ζ to around -45 mV. Parameter ζ decreased only for the SiC–OH NPs in the RPMI medium that evinced into low colloidal stability. The value of ζ of the SiC–x NPs in the DMEM medium is not presented since the SiC–x NPs evinced such a high surface charge (ζ of higher than ±50mV) that they could not be centrifuged out and analyzed. The media supplemented with 5% FBS resulted in a shift in the ζ back to approximately -30 mV, which is considered to be the colloidal stability level [35,36].

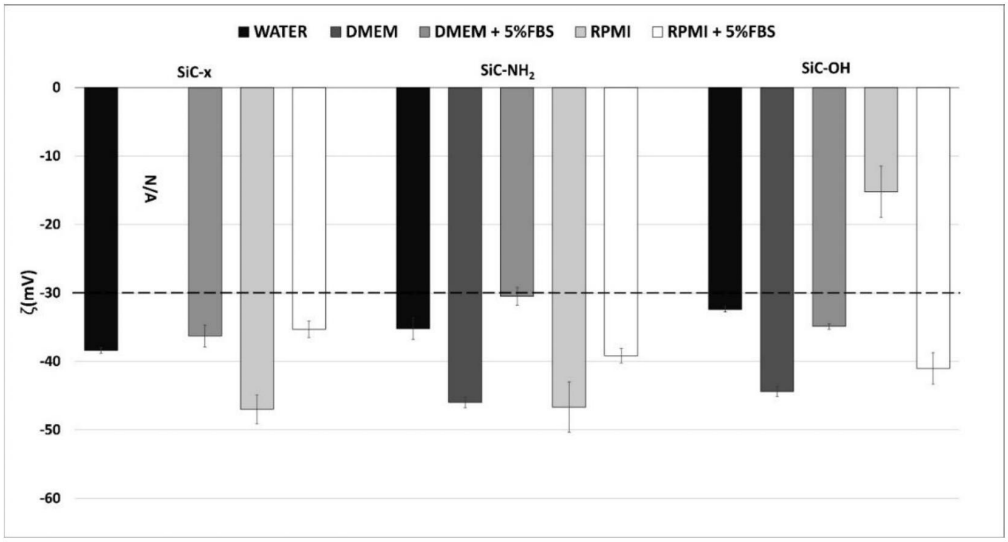


**Figure 2.** Value of ζ for the SiC-based NPs in different solutions. Parameter ζ was measured on NPs in water, DMEM and RPMI 1640 with and without the addition of 5% FBS.

### 3.3. Metabolic Activity of the Different Cells Following NP Treatment

The metabolic activity of the different cells (human osteoblasts—SAOS-2; and monocyte/macrophages —THP-1) following their exposure to SiC-based NPs was measured using the MTS test under standard (5% FBS in the medium from the outset) and non-standard (no FBS in the medium for the first 6 h followed by incubation in the medium supplemented with 5% FBS) conditions.

Figure 3A shows that the metabolic activity of a well-described and established osteoblastic cell line under standard conditions was not affected by any of the concentrations and types of NPs used. The metabolic activity was approximately at the same level as the control (untreated) cells in all cases.

In the case of non-standard conditions (Figure 3B), the metabolic activity after 6 h was comparable to that under standard cultivation conditions. However, after 24 h of incubation, the cellular metabolic activity of the SiC–$NH_2$ and SiC–OH NPs at higher concentrations increased significantly.

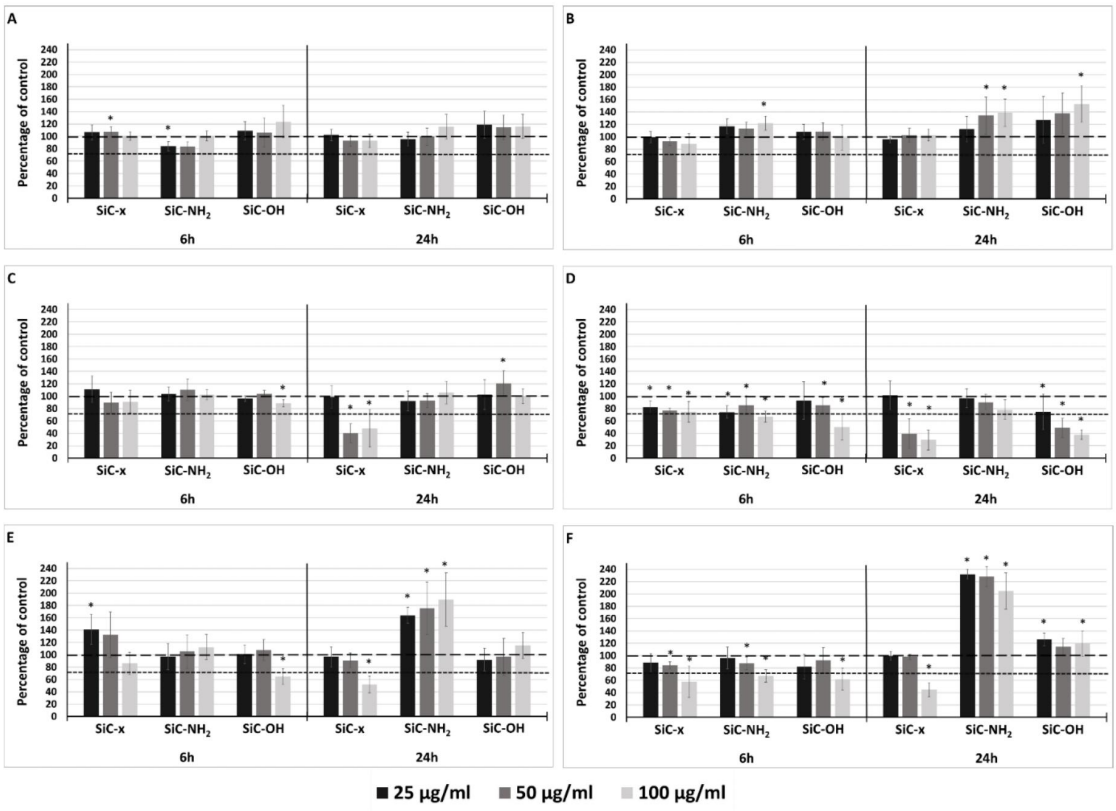


**Figure 3.** Metabolic activity of human cells treated with SiC-based NPs. Osteoblasts (SAOS-2) (**A**,**B**), adherent THP-1 (macrophage-like cells) (**C**,**D**), and suspension THP-1 (monocytic cells) (**E**,**F**) under standard cultivation conditions (**A**,**C**,**E**) and non-standard cultivation conditions (**B**,**D**,**F**). The data is presented in the form of means, deviation marks represent the standard deviation, the star symbol (*) denotes statistically significant changes against the control levels (Wilcoxon matched-pairs test, $p < 0.05$). The long dashed line shows 100% of the untreated control, the short dashed line shows 75% of the untreated control (cytotoxic level).

The human monocytic cell line—THP-1—was cultivated in two forms, i.e., as a suspension of monocytes and as substrate-adherent macrophage-like cells. Both these types of immune cells were tested for their metabolic activity following the administration of the differing SiC-based NPs.

In the case of tissue-specific, macrophage-like cells, the obvious effect of FBS medium supplementation was observed. Within the first 6 h of incubation under standard conditions, none of the NPs (with PCs) significantly affected the cellular metabolic activity (Figure 3C). A visible cytotoxic effect (metabolic activity under 75% of the control [37]) was observed later (after 24 h of incubation) with respect only to the two highest SiC–x NP concentrations. Under non-standard conditions (bare NPs), the metabolic activity was significantly reduced after 6 h by all the NP types and concentrations (Figure 3D). Moreover, all the NPs had attained the cytotoxic level at this time point at the highest concentration applied. After 24 h of incubation, substantial differences were observed between the differing NP types. After 6 h, the negative impact of the SiC–$NH_2$ NPs on the cells was insignificant; these NPs appeared to be harmless. Conversely, the SiC–x and SiC–OH NPs were significantly cytotoxic with the effect being dose-dependent.

With respect to the monocytes under the standard cultivation conditions (Figure 3E), after 6 h most of the NPs had not induced any changes in the cell metabolic activity, with two exceptions. The SiC–OH

NPs at the highest concentration reduced the metabolic activity to the cytotoxic level and the SiC–x NPs at the lowest concentration significantly increased the metabolic activity of the monocytes. After 24 h, the SiC–x NPs at the highest concentration reduced the monocytic metabolic activity to the cytotoxic level. The metabolic activity of the cells treated with SiC–OH NPs remained at or returned to the level of the untreated control cells. However, the SiC–$NH_2$ NPs markedly increased the metabolic activity of the monocytes (to around 200% of the control) after 24 h. Under non-standard conditions (Figure 3F), the metabolic activity was slightly reduced in all the cases after 6 h; however, after 24 h the situation was similar to that of the standard cultivation conditions. Again, the only cytotoxic NPs consisted of the SiC–x NPs at the highest concentration applied, whereas the SiC–OH NPs were at the level of the control cells and the SiC–$NH_2$ treated cells again, surprisingly, doubled their metabolic activity compared to the control.

The tested NPs induced such significant differences in the metabolic activity of the suspension monocytes that further experiments were initiated focusing on these cells as treated with the highest applied NP concentration under non-standard cultivation conditions for 24 h.

### *3.4. Cell Number, Mitochondrial Mass, and Mitochondrial Potential*

On that account these monocytes were further characterized with respect to the cell number (Figure 4B), mitochondrial mass (Figure 4C) and mitochondrial potential (Figure 4D) because each of them can influence the metabolic activity determined by used method (MTS assay). This method is based on the conversion of a tetrazolium compound to a colored formazan product which is presumably accomplished by NADPH or NADH produced by dehydrogenase enzymes in metabolically active cells. These dehydrogenases are located in mitochondria as well as in cytosol. In spite of their differing metabolic activities (Figure 4A), the number of monocytes was comparable following treatment with differently-terminated SiC-based NPs (Figure 4B). Even though the SiC–x NP treated cells demonstrated a statistically significant decrease in their number (to 95% of the control cells), it did not reflect the significant decrease in their metabolic activity (to 50% of the control cells) (Figure 4A).

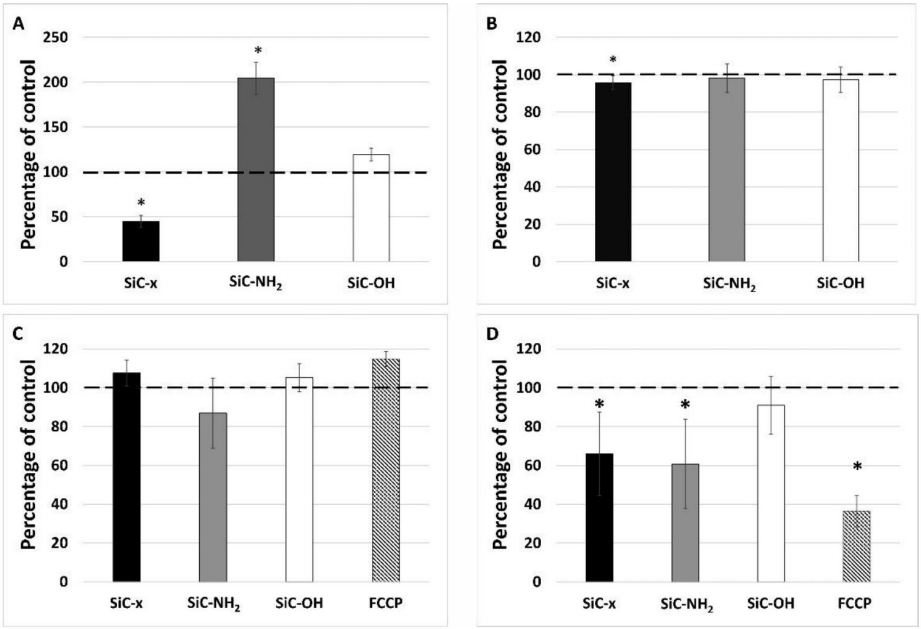


**Figure 4.** Metabolic activity (**A**), cell number (**B**), mitochondrial mass (**C**), and mitochondrial potential (**D**) after the 24-hour treatment of monocytes with differing SiC-based NPs. The data is presented in the form of means, deviation marks representing the standard deviation, the star symbol (*) denotes statistically significant changes against the control levels (Wilcoxon matched-pairs test, $p < 0.05$). The dashed line shows 100% of the untreated control.

In order to monitor the role of mitochondria in the increased metabolic activity, the overall mitochondrial mass and membrane potential were evaluated using flow cytometry. Figure 4C shows no significant differences in the mitochondrial mass (determined using a fluorescent probe independent of the mitochondrial potential) observed for the cells treated with all three types of NPs tested over 24 h. The determination of the mitochondrial membrane potential was conducted in the same manner as that of the detection of the mitochondrial mass; however, the probe accumulation in mitochondria is highly dependent on their membrane potential as confirmed via FCCP, which was used as an uncoupling agent. As shown in Figure 4D, the SiC–x NPs significantly decreased the mitochondrial potential of the monocytes. Surprisingly, the same phenomenon was also observed in the cells incubated with SiC–$NH_2$ particles whose metabolic activity (Figure 4A) was particularly high. The SiC–OH NP treated cells evinced a non-significant decrease in their mitochondrial potential that was comparable to the untreated control.

### *3.5. Cytokine Release from the Monocytes Following Treatment with Differing SiC-Based NPs*

Cytokines play a key role in cell signaling and this role is even more important in the immune system in terms of mediating its response to different irritating agents. A broad panel of 42 cytokines was tested in order to determine the most important molecules related to the effect of SiC-based NPs on monocytes. Following normalization to the NP untreated control, various cytokine profiles induced by differently-terminated SiC-based NPs were detected (Figure 5). The release of all the detected cytokine types from the cells treated with SiC–x NPs was generally lower than those treated with SiC–$NH_2$ and SiC–OH NPs. The pro-inflammatory cytokine interleukin 8 (IL-8) was the only cytokine released at a significant level by the SiC–x NP stimulated cells. High levels of IL-8 were also detected in the cells treated with other types of NPs. Moreover, treatment with SiC–$NH_2$ and SiC–OH NPs induced a significant increase in a variety of cytokines such as pro-inflammatory MCP-1, RANTES, and IL-1β and pro-mitogenic GRO-α compared to the untreated control and the cells treated with SiC–x NPs. All of these cytokines were also produced by the positive control cells (cells treated with lipopolysaccharide—LPS), but at an elevated level.

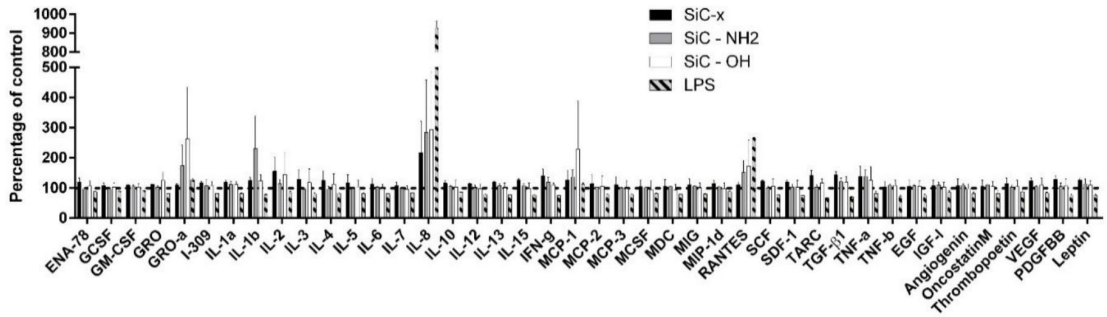


**Figure 5.** Cytokines detected in the supernatant from the suspension THP-1 monocytes. Cells were treated with 100 μg/mL of SiC-based NPs or LPS under non-standard conditions. After 24 h of incubation, cell supernatant was harvested and analyzed for the presence of a broad panel of cytokines. The data was normalized and is presented as a percentage of the untreated control supernatant levels. The error bars show standard deviation. The dashed line shows 100% of the untreated control.

### *3.6. Morphological Changes in the Cells Following Long-Term Treatment with SiC-Based NPs*

Since no change was observed in the monocyte morphology following short-term incubation (24 h) with NPs of differing surfaces, the long term (7 days) influence of the various SiC-based NPs (100μg/mL) on the monocytic cells was determined; Figure 6 shows the representative morphology of the most commonly-found cells. The control monocytes (Figure 6D) were treated in the same way as the other NP-treated cells (6 h incubation in FBS-free medium, the rest of the incubation time in the medium

supplemented with 5% FBS). After 7 days, the cells demonstrated only slight changes in the cytoplasm content compared to fresh THP-1 cells sub-cultured in the standard way (Figure 6F). More dramatic changes were observed in all of the NP-treated cells. All of the SiC–x NP treated cells were found to be dead and only cell debris could be observed (Figure 6A). Treatment with SiC–$NH_2$ (Figure 6B) induced an increase in the total number of cells (data not shown) compared to all the other samples, and a significant number of adhered cells with a macrophage-like morphology similar to the cells that were chemically-differentiated into macrophage-like cells (Figure 6G). However, a high number of cells remained in suspension with a morphology similar to the control monocytes (Figure 6D). An interesting mixture of morphology types was observed with respect to SiC–OH treatment (Figure $6C_{1\text{-}3}$). While a portion of the cells revealed a macrophage-like morphology (Figure $6C_3$) as in the SiC–$NH_2$ treated cells (Figure 6B), some of the cells also acquired a dendritic cell-like morphology (Figure $6C_1$) similar to the cells that chemically-differentiated into dendritic-like cells (Figure 6E). The remaining cells were either dead (only a small number) or resembled fresh THP-1 cells (Figure $6C_2$).

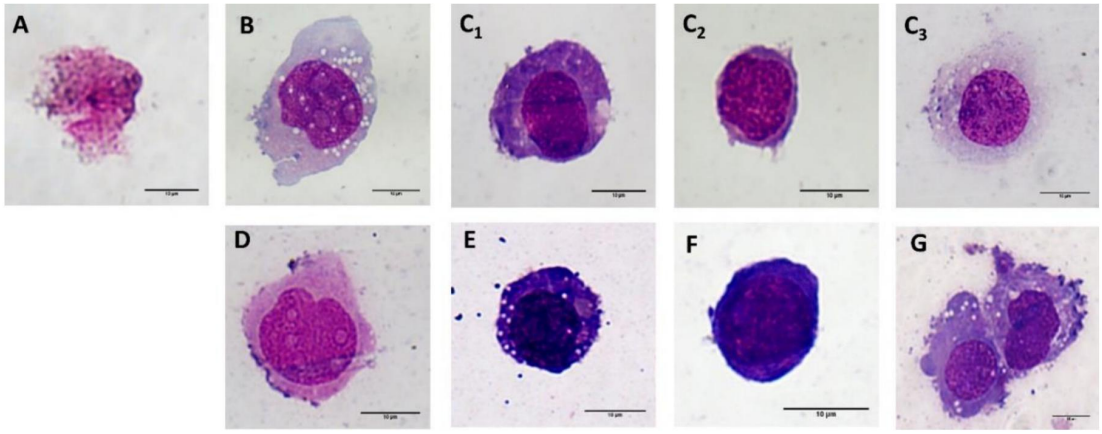


**Figure 6.** Microscopic analysis of the morphological changes on the THP-1. Representative images of the monocytic THP-1 cells after 7 days of incubation with 100 µg/mL SiC–x NPs (**A**), SiC–$NH_2$ (**B**) and SiC–OH (**$C_1$**—dendritic cell-like; **$C_2$**—monocytic; and **$C_3$**—macrophage-like). Control cells (monocytes, incubated in the same manner as the NP-treated cells (10,000 cells/$cm^2$) (**D**), chemically-differentiated monocytes to dendritic-like cell morphology (**E**), monocytes (kept in the culture – 133 000 cells/$cm^2$) (**F**), and chemically-differentiated macrophage-like cells (PMA treatment) (**G**). All the images were captured at 100× magnification; the scale bar represents 10 µm.

## 4. Discussion

It is known that the majority of particles tend to change their ζ following the transition into biological fluids [38,39]. Even though amine-terminated surfaces usually have positive zeta potential in salt-free solutions and acidic pH, the data presented herein showed highly negative ζ in case of SiC–$NH_2$ NPs. This could be explained by incomplete functionalization of the NP surface. SiC-based NPs are rich in surface groups as one can see in the FTIR spectra (Figure 1A). The overall zeta potential is determined by the salinity and counterions in the solution, the pH, and the surface chemistry. Among the amine groups, SiC–$NH_2$ NPs surface likely contains unreacted hydroxyl and silanol groups, and C=C double bonds. This influences the surface potential because of the small distance between particular hydroxyl groups [33], sterical hindrance is expected. The SiC-based NPs presented herein proved to be fully dispersed both in water and in the cultivation medium even when supplemented with FBS, which suggests that the particles remained in the colloid and thus were able to interact with the cells as individual entities. However, a negative ζ may prevent direct contact with a negatively-charged cellular membrane. Nevertheless, the effect induced by the SiC-based NPs on the various cells is apparent, thus indicating the existence of interaction. Moreover, other research has pointed out the potential for NP-cell interaction under such conditions [40–42]. The only exception where the ζ

was shifted to a surface charge range that favored cluster formation involved the SiC–OH particles incubated in the RPMI 1640 medium. This shift was not observed for the DMEM medium and, from the simple comparison of the media composition, it was not possible to determine a clear link. Some ingredients were presented at strikingly different concentrations (e.g., sodium phosphate monobasic in the RPMI compared to the DMEM (800 mg/l and 125 mg/l respectively)), which may have been the reason for such a change. The dramatic drop in the ζ potential of the SiC–OH NPs (to -17 mV) in the RPMI medium was restored to the ζ corresponding to the stable colloidal solution when the NPs were incubated in the RPMI medium supplemented with FBS. Thus, in this case, the FBS inhibited aggregate formation. The aggregation preventive properties of FBS have already been described by Balek et al. concerning nanodiamonds [43].

The concentration gradient of the NPs used herein was based on our previous research on different types of ultra-small silicon-based NPs [42,44]. In both of these studies, said concentration gradients proved to have an impact on metabolic activity of osteoblastic cell line (SAOS-2). Surprisingly, the results showed that irrespective of the NP surface termination, concentration, and cultivation conditions, none of the SiC-based NPs exerted a significant effect on the metabolic activity of these cells in the short-term experiment (24 h). In context of further results presented herein, it seems that used doses of NPs are inert in respect of osteoblasts but cause response in much more responsive cells such as immune cells. Furthermore, the slight elevation in the metabolic activity of the osteoblasts treated with SiC–$NH_2$ and SiC–OH after 24 h of incubation indicated possible cell–NP interactions with potentially longer manifestation times.

The same NPs were also tested with respect to tissue-specific immune cells (adherent THP-1 cells, sometimes referred to as macrophage-like cells). In this case, the initial FBS supplementation of the cultivation medium and, thus, the immediate formation of PCs on the NPs, proved to be the overall key factor that protected the cells from an NP-induced decrease in metabolic activity. This finding corresponds with the previously reported cell-protective impact of protein adsorption onto NPs [20,21,29]. However, this protective effect was not sufficient to prevent a decrease in the metabolic activity of the cells treated with the two highest SiC–x NP concentrations after 24 h. Under non-standard cultivation conditions, the bare NPs (without PCs) initiated a significant decrease in the metabolic activity of these cells after a short incubation period. However, following the removal of the medium containing the NPs and its replacement with a fresh FBS-containing medium (at the 6 h time point), the effect of the SiC–$NH_2$ NPs was neutralized and the cell activity was restored to the level of the untreated cells. A similar protective effect of PC was observed in the cells treated with the lowest concentration of SiC–x NPs. Moreover, the higher SiC–x NP concentration accentuated the harmful effect of these NPs, which could have meant that the SiC–x NPs induced irreversible harm to the cells within the first 6 h of incubation, while the SiC–$NH_2$ NPs were less harmful and may have initiated apoptotic rescue mechanisms [45]. This observed phenomenon implies that a certain critical concentration of SiC–x and SiC–$NH_2$ NPs exists and that, within the first 6 h, it exerts a decisive influence on the fate of cells. The same situation did not apply, however, in the case of the SiC–OH NPs, where an ongoing concentration-dependent toxic effect was observed even after the NP-containing medium had been discarded. In this case, the SiC–OH NPs in the RPMI medium without FBS exhibited the ζ of -17 mV, thus rendering them prone to NP aggregation. Such aggregates cannot be dissolved via the simple addition of FBS and, moreover, are prone to sedimentation. These aggregated sediments cannot easily be discarded in the same manner as the non-clustered particles (SiC–x and SiC–$NH_2$ NPs) which remained in the colloid. Thus, SiC–OH NPs may exert an ongoing negative impact on cellular metabolism which may be caused, for example, by the simple mechanical blocking of the membrane due to the quantity of NP clusters, thus resulting in the occurrence of harmful changes in the cellular membrane phase (i.e., gelation) [46]. Since the ζ of the SiC–OH NPs in the RPMI medium supplemented with FBS was -41 mV, the NPs most probably remained in the colloid and exerted no impact on the cellular metabolism. The statistical significances are not presented since they were not considered to be biologically relevant.

Furthermore, when the NPs were tested with respect to monocytic cells, the protective properties of FBS supplementation were also observed; however, the surface termination of the NPs proved to be highly important. In this case, slightly different cultivation conditions were applied (the NPs remained in the incubation medium throughout the whole of the experiment) since the cultivation of suspension cells requires a different approach. The SiC–x NPs demonstrated a similar effect on cellular metabolism under both standard and non-standard conditions. The SiC–$NH_2$ NPs proved to be harmless under standard conditions (FBS supplemented) within the first 6 h of incubation and, interestingly, longer cultivation times led to a significant increase in the metabolic activity. Under non-standard conditions, the observed impact of the SiC–$NH_2$ NPs on the cellular metabolism was similar to that seen previously with the macrophage-like THP-1. The potential rescue from apoptosis discussed previously concerning these particles manifested itself to a remarkable extent. The SiC–OH NPs exhibited strong FBS-supplementation dependence with regard to their cytotoxic abilities. Under standard cultivation conditions, the monocytic cells responded in the same manner as macrophage-like cells, the explanation for which could be the same as for the previously-described macrophage-like cells, despite monocytic THP-1 cells being non-adherent. As such, the monocytes may have come into contact with the clustered SiC–OH NPs only within the first 6 h since the plate was incubated on a shaker so as to prevent sedimentation. After this time point, the shaker was switched off and, most probably, the clusters so formed sedimented, while the cells remained in suspension and subsequently encountered the NPs. The 24-hour time point confirmed the enormous impact of surface termination on the NP-cell interaction as previously reported [47,48]. This phenomenon was clearly observed particularly under non-standard conditions with the highest concentration of NPs applied.

The MTS assay employed is commonly considered a reflection of the cellular mitochondria function due to the principle thereof (the reduction of the tetrazolium compound into formazan via cellular NAD(P)H dehydrogenase), i.e., the dehydrogenases are most commonly found in the mitochondria. Even though the results of the MTS test suggested that the cellular metabolism differs significantly depending on the type of NP, the other results obtained demonstrated that after 24 h of incubation, the cells treated with all three types of NPs exhibited approximately the same mitochondrial mass. Significant and unexpected changes were, however, identified with respect to the mitochondrial potential. The SiC–$NH_2$ NP-treated cells evinced approximately the same mitochondrial potential as the SiC–x NP-treated cells with completely the opposite metabolic activity detected. As some researchers have pointed out, while the MTS and MTT assays do not necessarily exclusively reflect the mitochondrial NAD(P)H dehydrogenase activity, the other dehydrogenases participate in the chemical reaction to a far lower extent [49,50]. This could indicate that the SiC–$NH_2$ NP treatment led to the switching of the cellular metabolism, most probably from oxidative phosphorylation to glycolysis, concerning which glyceraldehyde 3-phosphate dehydrogenase may have performed the reduction of tetrazolium salt observed via the MTS assay. This switch may, in turn, indicate that the SiC–$NH_2$-stimulated monocytes were directed towards differentiation into activated M1 macrophages, which are known to produce ATP primarily from glycolysis since oxidative phosphorylation is used as an ROS producer to efficiently kill bacteria [51,52].

Since different reactions were observed between the monocytic cells and the various SiC-based NPs tested, it was clear that their reaction with respect to cytokine release should be examined. There is no information in the literature regarding cytokine production following cell stimulation with ultra-small SiC-based NPs, therefore a broader overview was considered necessary. Thus, a panel of 42 cytokines was tested in order to simply and qualitatively determine the presence of certain cytokines. It is common for any foreign material to induce an inflammatory response from immune cells since the surface identity does not usually resemble any naturally-occurring component. A number of studies have reported the production of inflammatory cytokines such as IL-6, IL-1β, and TNF-α related to the nanoparticle treatment of cells [53–55]. The results demonstrated that while all the tested SiC-based NPs induced inflammation to a certain extent, the effect was not as strong as in the positive control (LPS treatment). The observed inflammatory pattern suggests that monocytic THP-1 cells respond and interact with

all types of SiC-based NPs. Moreover, the production of classical pro-inflammatory cytokines, such as IL-1β and TNF-α, supports the potential for M1 macrophage differentiation and polarization since such cytokines are commonly connected to these cells. In addition, the other cytokine species observed at higher levels such as RANTES, IL-8, and MCP-1 indicated that NPs activate monocytes and act as pro-inflammatory agents. Particularly high levels of IL-8 were observed, thus suggesting that these NPs could potentially lead to a granulocytic immune cell response which is known to be one of their most common functions in vivo. IL-8 has also been demonstrated to act as an angiogenesis mediator by inducing chemotactic and proliferative activity in endothelial cells [56]. The presence of IL-8 and MCP-1, however, should be of concern since the combination of these two cytokines is known to attract neutrophils and to promote inflammation. Fortunately, no allergic response (increased levels of IL 4, 5, and 13) was detected via the application of the tested NPs; their presence would have prevented the future use of such NPs in vivo since a strong allergic reaction could result in fatal consequences (e.g., anaphylactic shock in living organisms). Increased attention is being devoted to the role of NPs in the development of new allergies, which is increasingly becoming a subject of concern in human medicine [26,57]. The non-presence of pro-allergic cytokines produced by monocytic THP-1 cells in response to SiC-based NP treatment is thus desirable and indicates that this nanomaterial is harmless in this respect; however, significant concerns with respect to acute inflammation have been raised by high levels of IL-8 and MCP-1. These cytokines also present promising application potential concerning their positive influence on neutrophils. The fact that monocytic cells interact with nanoparticles, while not becoming over-activated, identifies these SiC-based NPs as a potential immunomodulatory material.

Practically no long-term studies of the influence and differentiation abilities of NPs have been conducted to date. in vivo, monocytes possess the ability to differentiate into macrophages or dendritic cells dependent on the needs of the immune system. Since various pro-inflammatory cytokines were detected after 24 h of incubation with the particles, the possible impact on changes in the cellular morphology were studied after a longer period (7 days). The cells cultured with SiC–$NH_2$ and SiC–OH NPs evinced significant changes in their morphology, thus suggesting the application potential of these NPs as immunomodulatory material. Since most of the cells treated with SiC–$NH_2$ particles were transformed into adherent macrophage-like cells and the SiC–OH NPs provided cells that differentiated into macrophage-like and dendritic cell–like morphologies, both of these particles might potentially be employed as ex vivo stimuli for immune cell therapy via long-term treatment as well as for the stimulation (again, ex vivo) of the immune response in immunodeficient individuals. This ex vivo application has been proposed with respect to various silicon-based NPs [54,58]. However, in the case of the SiC–$NH_2$ NPs, further attention should be devoted to the observed increase in the cell count (not published), which could indicate the mean overstimulation of the cells and could possibly lead to an undesirable excessive response. Consequently, SiC–OH NPs might be considered eligible for further ex vivo application as suggested since, although the number of cells did not differ from the control, differentiation was present. Morphological changes were also observed in the control cells that were treated in the same manner as the NP-treated samples. While the cells remained in suspension, they evinced a markedly higher amount of cytoplasm. This change was most probably caused by the suboptimal cultivation conditions (i.e., low cell density) that were applied so as to retain the same conditions as those of the NP-treated cells. Another possible explanation is that standard cultivation (high cell density) was conducted in the medium supplemented with heat inactivated FBS (i.e., inactive complement), while the particle-related experiments (cultivation in low cell density) were conducted in the medium with FBS without heat inactivation (i.e., active complement).

All the aforementioned potential applications must, however, be further tested on primary cells from human donors. The ex vivo stimulation of cells and the subsequent return of such cells into the body presents a further direction for immunomodulation research. Cells stimulated in this way could produce cytokines that positively influence the number and activity of neutrophils, which offers potential with concern to neutrophil-related immunodeficiencies [59].

## 5. Conclusions

Even though different termination of SiC-based NPs does not have a significant effect on their colloidal stability in the cultivation media, it plays a key role in respect to human cells. Monocytes, being a key part of the immune system, produce a variety of cytokines upon contact with these NPs and mark them as a potential immunomodulatory material. Further research regarding changes in metabolic pathways, differentiation capabilities and cytokine productions were however of major interest in order to correctly establish the application potential of these NPs.

**Author Contributions:** Data curation, T.B.; Funding acquisition, M.H.K.; Investigation, T.B., I.M., D.B., and A.F.; Methodology, T.B., D.B., and A.F.; Project administration, M.H.K.; Resources, A.G., J.V., and M.H.K.; Supervision, M.H.K.; Writing—original draft, T.B.; Writing—review and editing, D.B., A.F., A.G., Z.H., J.V., and M.H.K. All authors have read and agreed to the published version of the manuscript.

**Funding:** This study was supported by the project of National Sustainability Program I no. LO1503, provided by Ministry of Education, Youth and Sports of the Czech Republic and by PROGRES Q26, UNCE/SCI/010 and SVV 260390 provided by Charles University, NTP-NFTÖ-18-B-0243 national talent program, the János Bolyai Scholarship of the Hungarian Academy of Sciences, UNKP-19 New National Excellence program, the EU QuantERA Nanospin project (NKFIH grant no. 127902), the National Quantum Technology Project (NKFIH grant no. 2017-1.2.1-NKP-2017-00001), and the NVKP project (NKFIH grant no. NVKP_16-1-2016-0043).

**Conflicts of Interest:** The authors declare no conflict of interest.

## References

1. Lee, M.Y.; Yang, J.A.; Jung, H.S.; Beack, S.; Choi, J.E.; Hur, W.; Koo, H.; Kim, K.; Yoon, S.K.; Hahn, S.K. Hyaluronic acid-gold nanoparticle/interferon alpha complex for targeted treatment of hepatitis C virus infection. *ACS Nano* **2012**, *6*, 9522–9531. [CrossRef] [PubMed]
2. Slowing, I.I.; Vivero-Escoto, J.L.; Wu, C.W.; Lin, V.S. Mesoporous silica nanoparticles as controlled release drug delivery and gene transfection carriers. *Adv. Drug Deliv. Rev.* **2008**, *60*, 1278–1288. [CrossRef] [PubMed]
3. Dasari, B.C.; Cashman, S.M.; Kumar-Singh, R. Reducible PEG-POD/DNA Nanoparticles for Gene Transfer In Vitro and In Vivo: Application in a Mouse Model of Age-Related Macular Degeneration. *Mol. Ther. Nucleic. Acids* **2017**, *8*, 77–89. [CrossRef] [PubMed]
4. Ha, S.W.; Sikorski, J.A.; Weitzmann, M.N.; Beck, G.R., Jr. Bio-active engineered 50 nm silica nanoparticles with bone anabolic activity: therapeutic index, effective concentration, and cytotoxicity profile in vitro. *Toxicol In Vitro* **2014**, *28*, 354–364. [CrossRef] [PubMed]
5. Zang, X.; Zhao, X.; Hu, H.; Qiao, M.; Deng, Y.; Chen, D. Nanoparticles for tumor immunotherapy. *Eur. J. Pharm. Biopharm.* **2017**, *115*, 243–256. [CrossRef] [PubMed]
6. Zhu, P.; Huang, S.; Li, M.; Ding, N.; Peng, B.; Kong, L.; Bo, Y. A sandwiched biological fluorescent probe for the diagnosis of human ovarian tumor based on TiO2 nanoparticles. *J. Fluoresc.* **2011**, *21*, 179–186. [CrossRef]
7. Costo, R.; Bello, V.; Robic, C.; Port, M.; Marco, J.F.; Puerto Morales, M.; Veintemillas-Verdaguer, S. Ultrasmall iron oxide nanoparticles for biomedical applications: improving the colloidal and magnetic properties. *Langmuir* **2012**, *28*, 178–185. [CrossRef]
8. Cassano, D.; Mapanao, A.-K.; Summa, M.; Vlamidis, Y.; Giannone, G.; Santi, M.; Guzzolino, E.; Pitto, L.; Poliseno, L.; Bertorelli, R.; et al. Biosafety and Biokinetics of Noble Metals: The Impact of Their Chemical Nature. *ACS Appl. Bio Mater.* **2019**, *2*, 4464–4470. [CrossRef]
9. Li, C.; Xu, L.; Liu, Z.; Li, Z.; Quan, Z.; Al Kheraif, A.A.; Lin, J. Current progress in the controlled synthesis and biomedical applications of ultrasmall (<10 nm) NaREF4 nanoparticles. *Dalton. Trans.* **2018**, *47*, 8538–8556. [CrossRef]
10. Frewin, C.L.; Locke, C.; Saddow, S.E.; Weeber, E.J. Single-crystal cubic silicon carbide: an in vivo biocompatible semiconductor for brain machine interface devices. *Conf. Proc. IEEE Eng. Med. Biol. Soc.* **2011**, *2011*, 2957–2960. [CrossRef]
11. Beke, D.; Szekrényes, Z.; Pálfi, D.; Róna, G.; Balogh, I.; Maák, P.A.; Katona, G.; Czigány, Z.; Kamarás, K.; Rózsa, B.; et al. Silicon carbide quantum dots for bioimaging. *J. Mater. Res.* **2012**, *28*, 205–209. [CrossRef]
12. Santavirta, S.; Takagi, M.; Nordsletten, L.; Anttila, A.; Lappalainen, R.; Konttinen, Y.T. Biocompatibility of silicon carbide in colony formation test in vitro. *Arch. Orthopaedic Trauma Surgery* **1998**, *118*, 89–91. [CrossRef]

13. Beke, D.; Szekrényes, Z.; Balogh, I.; Veres, M.; Fazakas, É.; Varga, L.K.; Kamarás, K.; Czigány, Z.; Gali, A. Characterization of luminescent silicon carbide nanocrystals prepared by reactive bonding and subsequent wet chemical etching. *Appl. Phys. Lett.* **2011**, *99*. [CrossRef]
14. Dravecz, G.; Janosi, T.Z.; Beke, D.; Major, D.A.; Karolyhazy, G.; Erostyak, J.; Kamaras, K.; Gali, A. Identification of the binding site between bovine serum albumin and ultrasmall SiC fluorescent biomarkers. *Phys. Chem. Chem. Phys.* **2018**, *20*, 13419–13429. [CrossRef]
15. Albanese, A.; Tang, P.S.; Chan, W.C. The effect of nanoparticle size, shape, and surface chemistry on biological systems. *Annu. Rev. Biomed. Eng.* **2012**, *14*, 1–16. [CrossRef]
16. Bhattacharjee, S.; Rietjens, I.M.; Singh, M.P.; Atkins, T.M.; Purkait, T.K.; Xu, Z.; Regli, S.; Shukaliak, A.; Clark, R.J.; Mitchell, B.S.; et al. Cytotoxicity of surface-functionalized silicon and germanium nanoparticles: the dominant role of surface charges. *Nanoscale* **2013**, *5*, 4870–4883. [CrossRef]
17. Frohlich, E. The role of surface charge in cellular uptake and cytotoxicity of medical nanoparticles. *Int. J. Nanomed.* **2012**, *7*, 5577–5591. [CrossRef]
18. Herd, H.; Daum, N.; Jones, A.T.; Huwer, H.; Ghandehari, H.; Lehr, C.M. Nanoparticle geometry and surface orientation influence mode of cellular uptake. *ACS Nano* **2013**, *7*, 1961–1973. [CrossRef]
19. Monopoli, M.P.; Aberg, C.; Salvati, A.; Dawson, K.A. Biomolecular coronas provide the biological identity of nanosized materials. *Nat. Nanotechnol.* **2012**, *7*, 779–786. [CrossRef]
20. Escamilla-Rivera, V.; Uribe-Ramirez, M.; Gonzalez-Pozos, S.; Lozano, O.; Lucas, S.; De Vizcaya-Ruiz, A. Protein corona acts as a protective shield against Fe3O4-PEG inflammation and ROS-induced toxicity in human macrophages. *Toxicol. Lett.* **2016**, *240*, 172–184. [CrossRef]
21. Lesniak, A.; Fenaroli, F.; Monopoli, M.P.; Aberg, C.; Dawson, K.A.; Salvati, A. Effects of the presence or absence of a protein corona on silica nanoparticle uptake and impact on cells. *ACS Nano* **2012**, *6*, 5845–5857. [CrossRef] [PubMed]
22. Wang, F.; Yu, L.; Monopoli, M.P.; Sandin, P.; Mahon, E.; Salvati, A.; Dawson, K.A. The biomolecular corona is retained during nanoparticle uptake and protects the cells from the damage induced by cationic nanoparticles until degraded in the lysosomes. *Nanomedicine* **2013**, *9*, 1159–1168. [CrossRef] [PubMed]
23. Erickson, H.P. Size and shape of protein molecules at the nanometer level determined by sedimentation, gel filtration, and electron microscopy. *Biol. Proced. Online* **2009**, *11*, 32–51. [CrossRef] [PubMed]
24. Sukwong, P.; Kongseng, S.; Chaicherd, S.; Yoovathaworn, K.; Tubtimkuna, S.; Pissuwan, D. Comparison effects of titanium dioxide nanoparticles on immune cells in adaptive and innate immune system. *IET Nanobiotechnol.* **2017**, *11*, 759–765. [CrossRef]
25. Chen, Q.; Wang, N.; Zhu, M.; Lu, J.; Zhong, H.; Xue, X.; Guo, S.; Li, M.; Wei, X.; Tao, Y.; et al. TiO2 nanoparticles cause mitochondrial dysfunction, activate inflammatory responses, and attenuate phagocytosis in macrophages: A proteomic and metabolomic insight. *Redox. Biol.* **2018**, *15*, 266–276. [CrossRef]
26. Hirai, T.; Yoshioka, Y.; Izumi, N.; Ichihashi, K.; Handa, T.; Nishijima, N.; Uemura, E.; Sagami, K.; Takahashi, H.; Yamaguchi, M.; et al. Metal nanoparticles in the presence of lipopolysaccharides trigger the onset of metal allergy in mice. *Nat. Nanotechnol.* **2016**, *11*, 808–816. [CrossRef]
27. Cho, W.S.; Duffin, R.; Poland, C.A.; Duschl, A.; Oostingh, G.J.; Macnee, W.; Bradley, M.; Megson, I.L.; Donaldson, K. Differential pro-inflammatory effects of metal oxide nanoparticles and their soluble ions in vitro and in vivo; zinc and copper nanoparticles, but not their ions, recruit eosinophils to the lungs. *Nanotoxicology* **2012**, *6*, 22–35. [CrossRef]
28. Nemmar, A.; Albarwani, S.; Beegam, S.; Yuvaraju, P.; Yasin, J.; Attoub, S.; Ali, B.H. Amorphous silica nanoparticles impair vascular homeostasis and induce systemic inflammation. *Int. J. Nanomed.* **2014**, *9*, 2779–2789. [CrossRef]
29. Caracciolo, G.; Palchetti, S.; Colapicchioni, V.; Digiacomo, L.; Pozzi, D.; Capriotti, A.L.; La Barbera, G.; Lagana, A. Stealth effect of biomolecular corona on nanoparticle uptake by immune cells. *Langmuir* **2015**, *31*, 10764–10773. [CrossRef]
30. Lappas, C.M. The immunomodulatory effects of titanium dioxide and silver nanoparticles. *Food Chem. Toxicol.* **2015**, *85*, 78–83. [CrossRef]
31. Liu, Y.; Hardie, J.; Zhang, X.; Rotello, V.M. Effects of engineered nanoparticles on the innate immune system. *Semin. Immunol.* **2017**, *34*, 25–32. [CrossRef] [PubMed]
32. Beke, D.; Szekrényes, Z.; Balogh, I.; Czigány, Z.; Kamarás, K.; Gali, A. Preparation of small silicon carbide quantum dots by wet chemical etching. *J. Mater. Res.* **2012**, *28*, 44–49. [CrossRef]

33. Szekrényes, Z.; Somogyi, B.; Beke, D.; Károlyházy, G.; Balogh, I.; Kamarás, K.; Gali, A. Chemical Transformation of Carboxyl Groups on the Surface of Silicon Carbide Quantum Dots. *J. Phys. Chem. C* **2014**, *118*, 19995–20001. [CrossRef]
34. Beke, D.; Jánosi, T.Z.; Somogyi, B.; Major, D.Á.; Szekrényes, Z.; Erostyák, J.; Kamarás, K.; Gali, A. Identification of Luminescence Centers in Molecular-Sized Silicon Carbide Nanocrystals. *J. Phys. Chem. C* **2015**, *120*, 685–691. [CrossRef]
35. Hanaor, D.; Michelazzi, M.; Leonelli, C.; Sorrell, C.C. The effects of carboxylic acids on the aqueous dispersion and electrophoretic deposition of ZrO2. *J. Eur. Ceramic Soc.* **2012**, *32*, 235–244. [CrossRef]
36. O'Brien, R.W.; Midmore, B.R.; Lamb, A.; Hunter, R.J. Electroacoustic studies of moderately concentrated colloidal suspensions. *Faraday Discuss. Chem. Soc.* **1990**, *90*. [CrossRef]
37. Flahaut, E.; Durrieu, M.C.; Remy-Zolghadri, M.; Bareille, R.; Baquey, C. Study of the cytotoxicity of CCVD carbon nanotubes. *J. Mater. Sci.* **2006**, *41*, 2411–2416. [CrossRef]
38. Sikora, A.; Shard, A.G.; Minelli, C. Size and ζ-Potential Measurement of Silica Nanoparticles in Serum Using Tunable Resistive Pulse Sensing. *Langmuir* **2016**, *32*, 2216–2224. [CrossRef]
39. Branda, F.; Silvestri, B.; Costantini, A.; Luciani, G. The fate of silica based Stober particles soaked into growth media (RPMI and M254): A DLS and zeta-potential study. *Colloids Surf B Biointerfaces* **2015**, *135*, 840–845. [CrossRef]
40. Lin, J.; Alexander-Katz, A. Cell membranes open "doors" for cationic nanoparticles/biomolecules: insights into uptake kinetics. *ACS Nano* **2013**, *7*, 10799–10808. [CrossRef]
41. Jiang, Y.; Huo, S.; Mizuhara, T.; Das, R.; Lee, Y.W.; Hou, S.; Moyano, D.F.; Duncan, B.; Liang, X.J.; Rotello, V.M. The Interplay of Size and Surface Functionality on the Cellular Uptake of Sub-10 nm Gold Nanoparticles. *ACS Nano* **2015**, *9*, 9986–9993. [CrossRef]
42. Ostrovska, L.; Broz, A.; Fucikova, A.; Belinova, T.; Sugimoto, H.; Kanno, T.; Fujii, M.; Valenta, J.; Kalbacova, M.H. The impact of doped silicon quantum dots on human osteoblasts. *RSC Adv.* **2016**, *6*, 63403–63413. [CrossRef]
43. Balek, L.; Buchtova, M.; Kunova Bosakova, M.; Varecha, M.; Foldynova-Trantirkova, S.; Gudernova, I.; Vesela, I.; Havlik, J.; Neburkova, J.; Turner, S.; et al. Nanodiamonds as "artificial proteins": Regulation of a cell signalling system using low nanomolar solutions of inorganic nanocrystals. *Biomaterials* **2018**, *176*, 106–121. [CrossRef]
44. Belinova, T.; Vrabcova, L.; Machova, I.; Fucikova, A.; Valenta, J.; Sugimoto, H.; Fujii, M.; Hubalek Kalbacova, M. Silicon Quantum Dots and Their Impact on Different Human Cells. *Phys. Status Solidi (b)* **2018**. [CrossRef]
45. Tang, H.L.; Yuen, K.L.; Tang, H.M.; Fung, M.C. Reversibility of apoptosis in cancer cells. *Br. J. Cancer* **2009**, *100*, 118–122. [CrossRef]
46. Wei, X.; Jiang, W.; Yu, J.; Ding, L.; Hu, J.; Jiang, G. Effects of SiO2 nanoparticles on phospholipid membrane integrity and fluidity. *J. Hazard. Mater.* **2015**, *287*, 217–224. [CrossRef]
47. Lankoff, A.; Arabski, M.; Wegierek-Ciuk, A.; Kruszewski, M.; Lisowska, H.; Banasik-Nowak, A.; Rozga-Wijas, K.; Wojewodzka, M.; Slomkowski, S. Effect of surface modification of silica nanoparticles on toxicity and cellular uptake by human peripheral blood lymphocytes in vitro. *Nanotoxicology* **2013**, *7*, 235–250. [CrossRef]
48. Guller, A.E.; Generalova, A.N.; Petersen, E.V.; Nechaev, A.V.; Trusova, I.A.; Landyshev, N.N.; Nadort, A.; Grebenik, E.A.; Deyev, S.M.; Shekhter, A.B.; et al. Cytotoxicity and non-specific cellular uptake of bare and surface-modified upconversion nanoparticles in human skin cells. *Nano Res.* **2015**, *8*, 1546–1562. [CrossRef]
49. Bernas, T.; Dobrucki, J. Mitochondrial and nonmitochondrial reduction of MTT: interaction of MTT with TMRE, JC-1, and NAO mitochondrial fluorescent probes. *Cytometry* **2002**, *47*, 236–242. [CrossRef]
50. Berridge, M.V.; Tan, A.S. Characterization of the cellular reduction of 3-(4,5-dimethylthiazol-2-yl)-2,5-diphenyltetrazolium bromide (MTT): subcellular localization, substrate dependence, and involvement of mitochondrial electron transport in MTT reduction. *Arch. Biochem. Biophys.* **1993**, *303*, 474–482. [CrossRef]
51. Freemerman, A.J.; Johnson, A.R.; Sacks, G.N.; Milner, J.J.; Kirk, E.L.; Troester, M.A.; Macintyre, A.N.; Goraksha-Hicks, P.; Rathmell, J.C.; Makowski, L. Metabolic reprogramming of macrophages: glucose transporter 1 (GLUT1)-mediated glucose metabolism drives a proinflammatory phenotype. *J. Biol. Chem.* **2014**, *289*, 7884–7896. [CrossRef]
52. Palsson-McDermott, E.M.; O'Neill, L.A. The Warburg effect then and now: from cancer to inflammatory diseases. *Bioessays* **2013**, *35*, 965–973. [CrossRef]

53. Choi, J.; Zhang, Q.; Reipa, V.; Wang, N.S.; Stratmeyer, M.E.; Hitchins, V.M.; Goering, P.L. Comparison of cytotoxic and inflammatory responses of photoluminescent silicon nanoparticles with silicon micron-sized particles in RAW 264.7 macrophages. *J. Appl. Toxicol.* **2009**, *29*, 52–60. [CrossRef]
54. Gomez, D.M.; Urcuqui-Inchima, S.; Hernandez, J.C. Silica nanoparticles induce NLRP3 inflammasome activation in human primary immune cells. *Innate. Immun.* **2017**, *23*, 697–708. [CrossRef]
55. Chou, C.C.; Chen, W.; Hung, Y.; Mou, C.Y. Molecular Elucidation of Biological Response to Mesoporous Silica Nanoparticles in Vitro and in Vivo. *ACS Appl. Mater. Interfaces* **2017**, *9*, 22235–22251. [CrossRef]
56. Li, A.; Dubey, S.; Varney, M.L.; Dave, B.J.; Singh, R.K. IL-8 directly enhanced endothelial cell survival, proliferation, and matrix metalloproteinases production and regulated angiogenesis. *J. Immunol.* **2003**, *170*, 3369–3376. [CrossRef]
57. Himly, M.; Mills-Goodlet, R.; Geppert, M.; Duschl, A. Nanomaterials in the Context of Type 2 Immune Responses-Fears and Potentials. *Front. Immunol.* **2017**, *8*, 471. [CrossRef]
58. Kishimoto, T.K.; Maldonado, R.A. Nanoparticles for the Induction of Antigen-Specific Immunological Tolerance. *Front. Immunol.* **2018**, *9*, 230. [CrossRef]
59. Lakshman, R.; Finn, A. Neutrophil disorders and their management. *J. Clin. Pathol.* **2001**, *54*, 7–19. [CrossRef]


**Publication D**

Reznickova, A., N. Slavikova, Z. Kolska, K. Kolarova, **T. Belinova**, M. Hubalek Kalbacova, M. Cieslar, and V. Svorcik. "**Pegylated Gold Nanoparticles: Stability, Cytotoxicity and Antibacterial Activity**." Colloids and Surfaces A: Physicochemical and Engineering Aspects 560 (2019): 26-34, IF = 2.829

Colloids and Surfaces A 560 (2019) 26–34

Contents lists available at ScienceDirect

Colloids and Surfaces A

journal homepage: www.elsevier.com/locate/colsurfa

# PEGylated gold nanoparticles: Stability, cytotoxicity and antibacterial activity

A. Reznickova[a,*], N. Slavikova[a], Z. Kolska[b], K. Kolarova[a], T. Belinova[c], M. Hubalek Kalbacova[c,d], M. Cieslar[e], V. Svorcik[a]

[a] Department of Solid State Engineering, University of Chemistry and Technology, 166 28 Prague, Czech Republic
[b] Faculty of Science, J. E. Purkyne University, 400 96 Usti nad Labem, Czech Republic
[c] Biomedical Center, Faculty of Medicine in Pilsen, Charles University in Prague, 323 00 Pilsen, Czech Republic
[d] Institute of Pathological Physiology, 1st Faculty of Medicine, Charles University in Prague, 128 02 Prague, Czech Republic
[e] Faculty of Mathematics and Physics, Charles University, 121 16 Prague, Czech Republic

## GRAPHICAL ABSTRACT

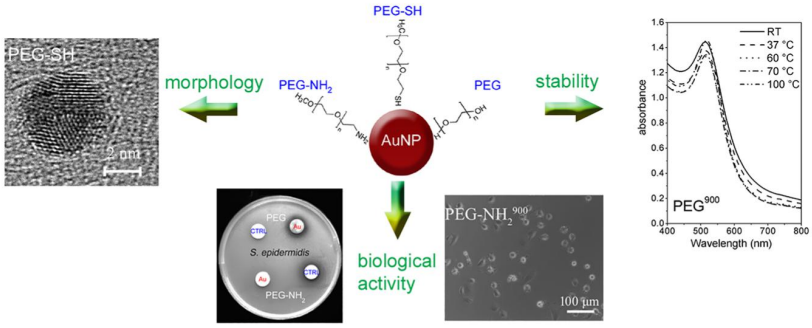


## ARTICLE INFO

*Keywords:*
Nanoparticle
Sputtering
Polyethylene glycol
Stability
Cytotoxicity
Antibacterial activity

## ABSTRACT

Designing safe nanomaterials is nowadays a critical issue. A way to prepare PEGylated Au NPs by sputtering of Au into pure (PEG), thiol (PEG-SH) and amine terminated polyethylene glycols ($PEG\text{-}NH_2$) was explored. Structural characterizations, aging and thermal stability were performed using transmission electron microscope (TEM/HRTEM) and UV–vis spectroscopy. By TEM we observed that spherical Au NPs were successfully prepared with average diameter of 1.5–5.9 nm. HRTEM revealed that a majority of them is rather of a round or irregular shape with a frequent multiple twinning. Dynamic light scattering as well as TEM confirmed that Au NPs have monodal size distribution. According to atomic absorption spectroscopy, concentration of gold increases with sputtering time and does not change with aging time. PEG-SH exhibited loss of SPR absorption band in UV–vis spectrum because of the small NP size (1.5 nm). PEG and $PEG\text{-}NH_2$ showed good thermal and aging stability. No significant antibacterial effect of any type of the studied Au NPs has been discovered. Cytotoxic effect on osteoblasts was determined only with the highest concentration of Au NP with PEG and $PEG\text{-}NH_2$ stabilization. Au NPs stabilized by PEG-SH showed the overall optimal physical and biological properties for drug delivery applications.

* Corresponding author.
*E-mail address:* alena.reznickova@vscht.cz (A. Reznickova).

https://doi.org/10.1016/j.colsurfa.2018.09.083
Received 30 June 2018; Received in revised form 24 September 2018; Accepted 27 September 2018
Available online 03 October 2018

## 1. Introduction

Nano-sized materials, especially gold nanoparticles (Au NPs) have broad spectrum of applications, from electronics and catalysis to drug carriers and bioimaging. Au NPs in particular are widely used because of their unique properties such as size, shape, optical properties, and low toxicity [1–5]. Two fundamental factors, both related to the size of individual nanocrystals, are responsible for their properties. The first is the large surface to volume ratio, and the second factor is the quantum confinement effect [6]. Nanoparticles can be prepared by either chemical or physical route (physical vapor deposition, laser ablation and γ irradiation) [7–9]. The methods can be complementary to each other; each has its specific advantages and disadvantages [10,11]. Cathode sputtering is one of the well-established techniques for preparation of metal nanostructures. The substrate type and its properties are crucial parameters in this method. Sputtering of metals onto surface of particular type of liquids generates dispersed metal clusters/NPs in the capturing media [10,12]. This method is regarded as an excellent process for the generation of clean NPs because neither chemical reactions nor additional stabilizing agents are needed except the capture medium [13].

Besides size and shape of Au NPs, surface ligands (capturing medium) and their density on NP surface play crucial role in bio-applications [14,15]. Functionalization of Au NPs surface with polyethylene glycol (PEG) is one of the ubiquitously used techniques, which significantly reduces nonspecific binding towards cells and serum proteins, and greatly extends the circulation half-life of Au NPs *in vivo*. These effects are often explained by PEGylation preventing formation of a protein corona so that the NPs are not recognized by the immune system [16]. Minimizing nonspecific interactions as much as possible *via* steric stabilization and control of surface charge is the key to prevent nanoparticle loss to undesired locations *i.e.* the liver, spleen or bone marrow [17–19]. PEG is inexpensive, versatile and it is approved by FDA [19]. It is also commercially available in many forms - from different molecular weight ratios to various functional groups - thiols, amines or even enzymes or vitamins *etc.*

Because of the above-mentioned properties, PEG is the most used polymer and the gold standard for stealth polymers in the emerging field of polymer based drug delivery. PEGylated drugs, liposomes, and nanocarriers are characterized by reduced renal filtration, decreased uptake by the reticuloendothelial system, and diminished enzymatic degradation. For this reason, PEGylated drugs show a prolonged half-life in the body and, thus, an enhanced bioavailability [20].

In this study, we tried to prepare uniform and stable, non-cytotoxic PEGylated Au NPs for potential drug delivery carriers. The influence of the PEG terminal functionalization (pure, thiol or amine) on cytotoxicity and antibacterial activity is compared. This paper builds on our previous study of PEGylated Au NPs [21].

**Table 1**
Size of PEGylated Au NPs (in nm; together with relative error) determined by TEM and DLS methods. Polydispersity index (PDI) of colloidal systems determined from DLS analysis.

| Sample | Size (nm) | | PDI |
|---|---|---|---|
| | TEM | DLS | |
| **PEG$^{300}$** | 5.6 ± 1.9 | 9.2 ± 1.5 | 0.429 |
| **PEG$^{900}$** | 5.9 ± 0.8 | 8.8 ± 2.2 | 0.201 |
| **PEG–SH$^{300}$** | 1.5 ± 0.3 | 3.1 ± 0.7 | 0.565 |
| **PEG–SH$^{900}$** | 1.6 ± 0.3 | 5.4 ± 0.6 | 0.524 |
| **PEG–NH$_2$$^{300}$** | 2.5 ± 0.8 | 4.3 ± 0.9 | 0.214 |
| **PEG–NH$_2$$^{900}$** | 2.9 ± 0.8 | 4.4 ± 1.1 | 0.252 |

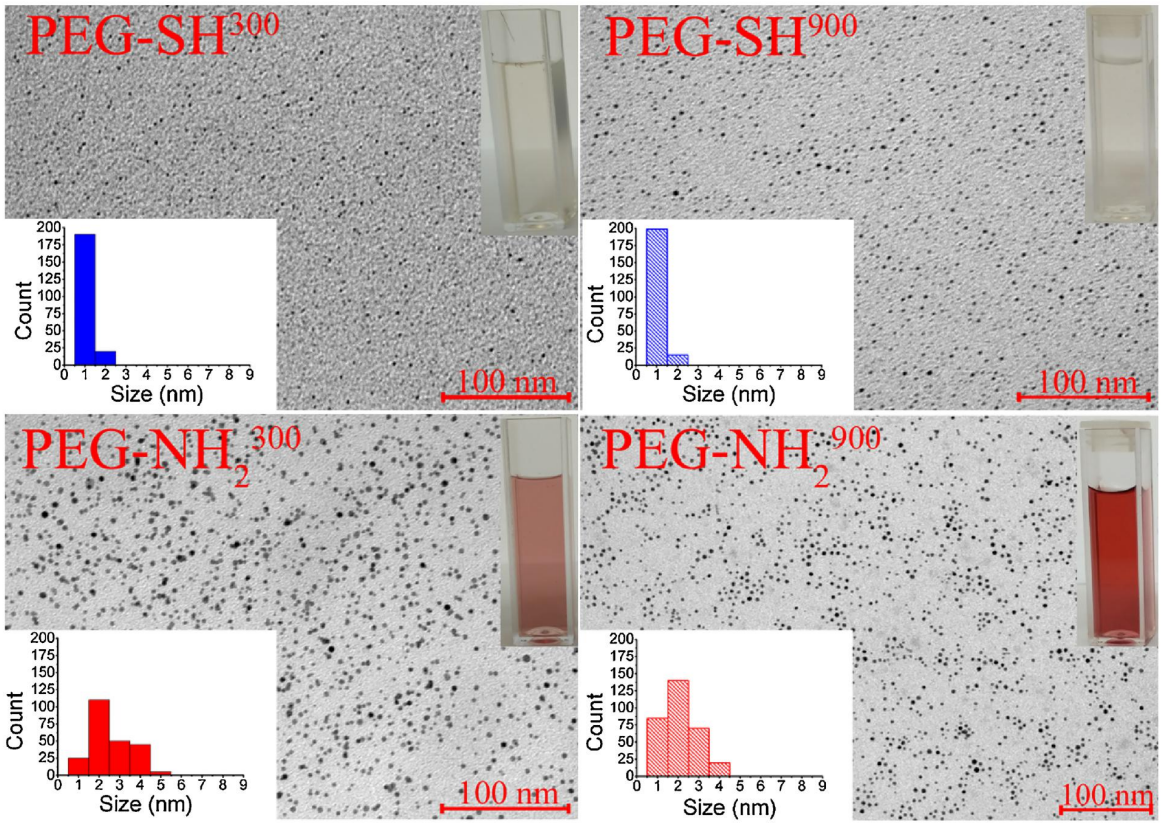


**Fig. 1.** TEM and cuvette images (inset on the right) of PEGylated Au NPs prepared by different time of Au sputtering into PEG–SH (300 s – top left; 900 s - top right) and PEG–NH$_2$ (300 s – bottom left; 900 s – bottom right). Histograms of Au NPs size distribution (from TEM analysis) are shown in the inset on the left.

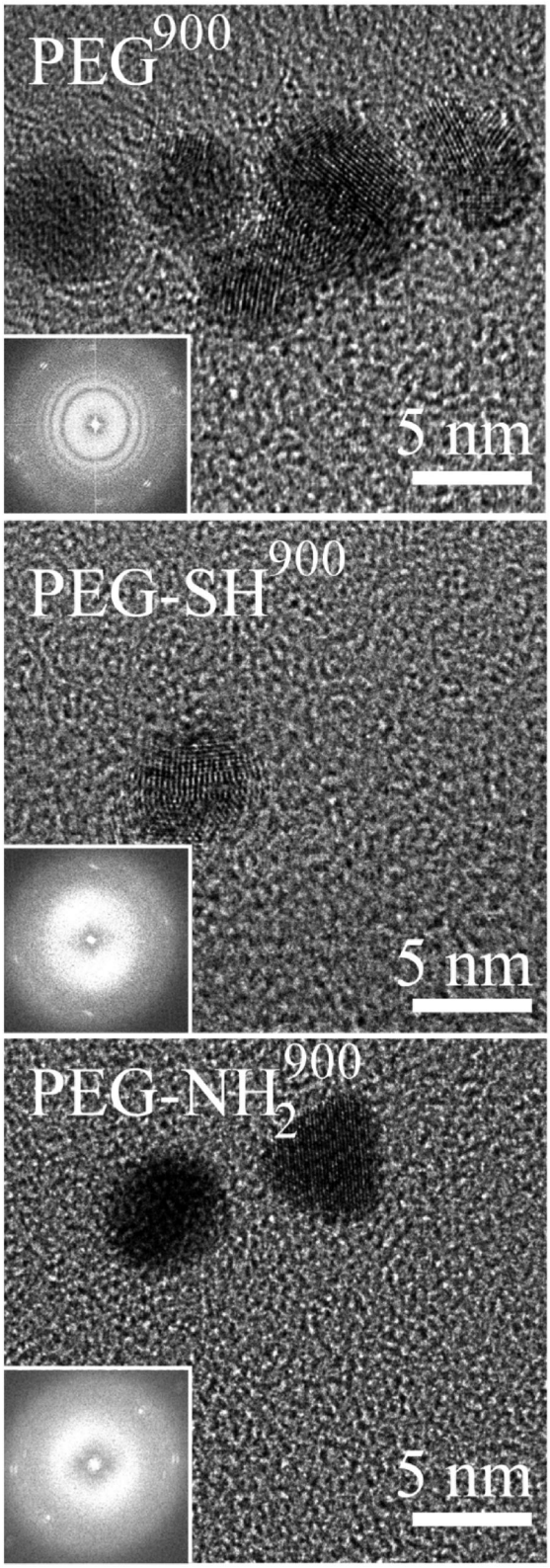


**Fig. 2.** HRTEM images and FFT plane projection (in the insets) of PEGylated Au NPs prepared by 900 s of Au sputtering into $PEG^{900}$, $PEG–SH^{900}$ and $PEG–NH_2{}^{900}$.

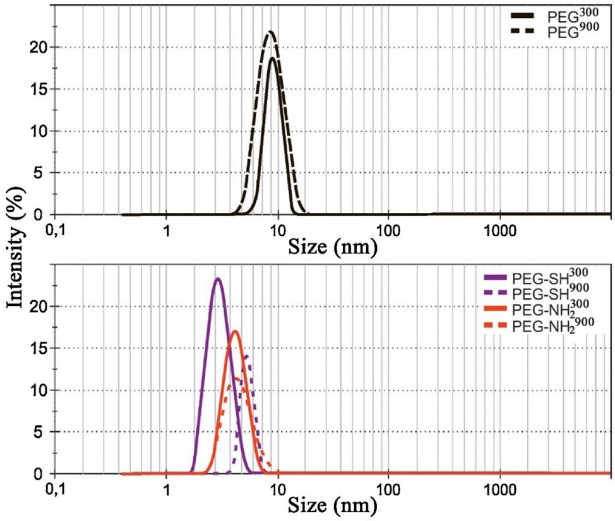


**Fig. 3.** Size and distribution characterization of prepared PEGylated Au NPs by DLS after sputtering of Au into: PEG (300 s – solid black line; 900 s – dashed black line), PEG–SH (300 s – solid red line; 900 s – dashed red line), $PEG–NH_2$ (300 s – solid purple line; 900 s – dashed purple line) (For interpretation of the references to colour in this figure legend, the reader is referred to the web version of this article).

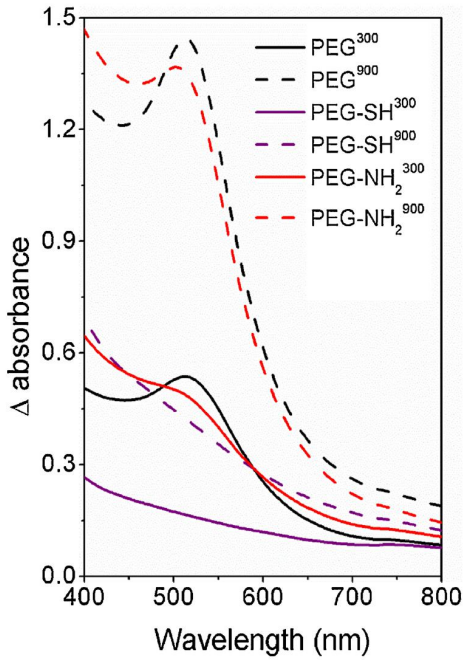


**Fig. 4.** UV–vis spectra of PEGylated Au NPs prepared by different time of sputtering of Au into PEG (300 s solid black line; 900 s – dashed black line), PEG–SH (300 s solid red line; 900 s – dashed red line) and $PEG–NH_2$ (300 s – solid purple line; 900 s – dashed purple line) (For interpretation of the references to colour in this figure legend, the reader is referred to the web version of this article).

## 2. Experimental section

### 2.1. Materials

Gold sputtering was performed by Sputter Coater SCD 050 (BAL-TEC, Pfaeffikon Balzers, LI) using Au target (purity 99.99%, provided by Safina a.s., CZ). Sputtering was accomplished at room temperature

**Table 2**
Concentration of Au (mg/l) in water-PEG solutions (1:9 by volume) with aging time (from 1st to 14th day) determined by AAS spectroscopy.

| Sample | Au concentration (mg/l) | | |
|---|---|---|---|
| | 1st day | 6th day | 14th day |
| **$PEG^{300}$** | 30.0 | – | – |
| **$PEG^{900}$** | 90.4 | 91.8 | 93.6 |
| **PEG–$SH^{300}$** | 27.3 | – | – |
| **PEG–$SH^{900}$** | 79.2 | 81.2 | 84.5 |
| **PEG–$NH_2{}^{300}$** | 31.8 | – | – |
| **PEG–$NH_2{}^{900}$** | 82.8 | 83.3 | 85.4 |

(25 °C), sputtering time of 300 and 900 s, current of 30 mA, voltage of 420–430 V, total argon pressure of 10 Pa (gas purity 99.996%, supplied by Siad a.s., CZ), an electrode distance of 5 cm. As a capturing media for preparation of metal NPs we used polyethyleneglycol (PEG, $M_w$ = 400 g $mol^{-1}$, ρ = 1.128 g $cm^{-3}$), polyethyleneglycol methyl ether thiol (PEG–SH, $M_w$ = 800 g $mol^{-1}$) and polyethyleneglycol methyl ether amine (PEG–$NH_2$, $M_w$ = 500 g $mol^{-1}$) supplied by Sigma-Aldrich Corp., US.

### 2.2. Preparation of PEGylated gold nanoparticles

The Petri dish of 4 cm inner diameter was filled with 2 ml of polyethylene glycol. Au was sputtered for 300 and 900 s directly into (i) pure PEG, (ii) PEG–SH and (iii) PEG–$NH_2$ (the weight ratio of PEG: PEG–SH and PEG: PEG–$NH_2$ was 20: 1). PEGylated Au NPs synthesized by Au sputtering for 300 and 900 s into PEG, PEG-SH and PEG-$NH_2$ will be in the text labelled as $PEG^{300}$/$PEG^{900}$, PEG-$SH^{300}$/PEG-$SH^{900}$ and PEG-$NH_2{}^{300}$/PEG-$NH_2{}^{900}$. $PEG^{300}$ and $PEG^{900}$ samples are used in this paper as a control. The procedure of NP preparation by Au sputtering into PEG is described in detail in Ref. [21]. The PEG with sputtered Au was poured into 25 ml vials and diluted in distilled water in a volume ratio of 1:9 [22]. Temperature stability of colloidal dispersion prepared by Au sputtering for 900 s at 4, 37, 60, 70 and 100 °C for 1 h was tested in closed vials using a hot plate (IKA® C-MAG HS 7, IKA®-Werke GmbH & Co. KG, DEU). The aging tests were performed on samples with Au sputtered for 900 s and stored at room temperature (RT).

### 2.3. Analytical methods

The samples for TEM were prepared by the deposition of a 6 µL drop of colloidal dispersion of Au NPs onto a carbon-coated copper grid. Excessive solution was removed and grids were dried by Whatman filtration paper. The samples were observed by TEM (JEM-1010; JEOL Ltd., JPN) at an accelerating voltage of 80 kV and 300,000 magnification. Pictures were taken by SIS MegaView III digital camera (Soft Imaging Systems, DEU) and analyzed by AnalySIS v. 2.0 software (Münster, DEU). Average size of the prepared NPs was determined based on AnalySIS v. 2.0 software calculation of 300 particles. More detailed structural characterization of PEGylated Au NPs was performed using the high - resolution transmission electron microscope HRTEM (JEOL JEM-2200FS, JEOL Ltd., JPN) operated at 220 kV and 800,000 magnification. Arrangements of Au atom in each nanoparticle has been determined from angle between projections calculated from Fast Fourier Transform (FFT) by using ImageJ software.

DLS was employed for determination of the hydrodynamic size and size distribution of the nanoparticle colloids and for the electrokinetic potential (zeta potential). The analysis of the samples was performed by Zetasizer ZS90 (Malvern Instruments Ltd., UK, Zetasizer Ver. 6.32 device, and Malvern software was used for data evaluation) and Malvern software was used for data evaluation (*i.e.* size, polydispersity index (PDI) and zeta potential). A diode pumped solid-state laser (50 mW, 366 nm) was used as a light source. The measurements were performed

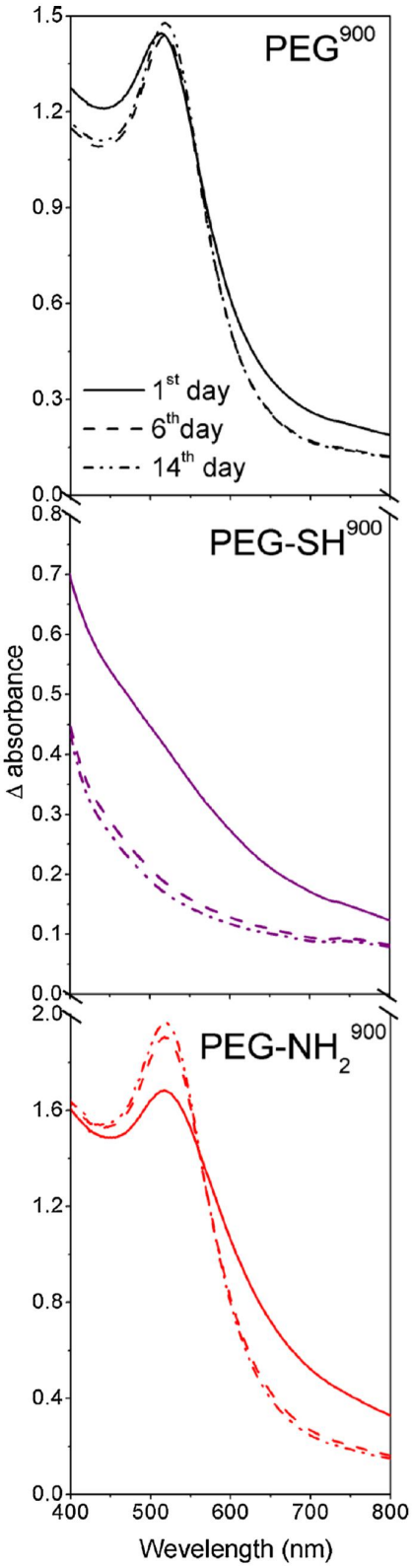


**Fig. 5.** Aging stability (from 1st to 14th day) of PEGylated Au NPs prepared by 900 s of Au sputtering into $PEG^{900}$, PEG–$SH^{900}$ and PEG–$NH_2{}^{900}$ determined by UV–vis spectroscopy.

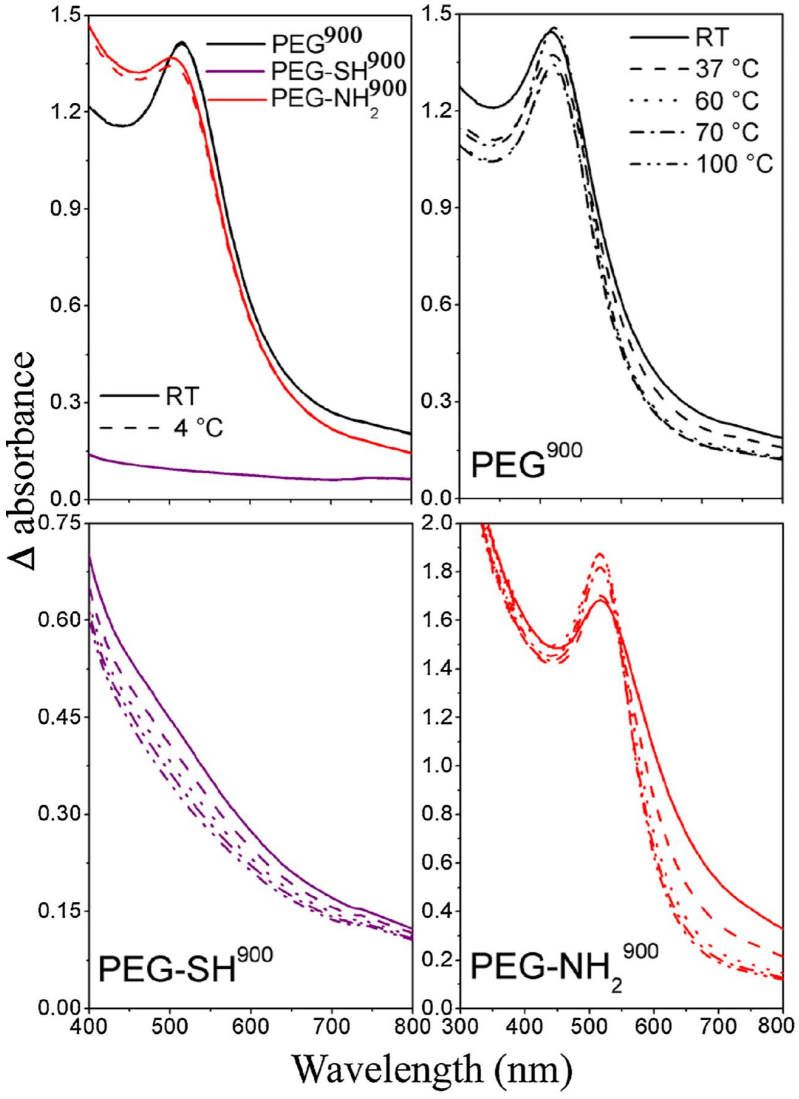


**Fig. 6.** Temperature stability (from 4 to 100 °C for 1 h) of PEGylated Au NPs prepared by 900 s of Au sputtering into $PEG^{900}$, $PEG–SH^{900}$ and $PEG–NH_2{}^{900}$ determined by UV–vis spectroscopy.

**Table 3**
Zeta potential (mV) of PEGylated Au NPs (together with relative error) with aging time (from 1st to 14th day) determined by Zetasizer.

| Sample | Zeta potential (mV) | | |
|---|---|---|---|
| | 1st day | 6th day | 14th day |
| **$PEG^{900}$** | −24.7 ± 4.5 | −22.3 ± 2.7 | −23.2 ± 7.5 |
| **$PEG–SH^{900}$** | −29.2 ± 1.6 | −30.6 ± 0.4 | −22.6 ± 1.5 |
| **$PEG–NH_2{}^{900}$** | −47.0 ± 1.3 | −55.5 ± 0.4 | −47.5 ± 4.9 |

in polystyrene cuvettes at RT and all samples were analyzed in 24 h after the preparation. Viscosity values of $\eta_{PEG400}$ = 119.0 mPa·s (for pure PEG) and for $\eta_{PEG/H2O}$ = 2.1 mPa·s (for PEG solutions) were used for DLS calculations of NP size and zeta potential.

Au concentration was determined using atomic absorption spectrometry using AAS spectrometer Varian AA 880 (Varian Inc., US). Determination was performed by flame atomization at a wavelength of 242.8 nm. AAS is used as an analytical characteristic absorption of radiation by free atoms of the reference element. For creation (generation) of free atoms in AAS is the most commonly used flame, which accordingly to the type of fuel and oxidizing agent reaches temperatures up to 3000 K.

UV-Vis spectroscopy was used to characterize the optical properties, aging (1st, 6th and 14th day) and thermal (4, 37, 60, 70 and 100 °C) stability of the samples. Absorbance was measured using Lambda 25 spectrophotometer (Perkin Elmer Inc., US) in a 10 mm polystyrene cuvette in a spectral range of 400–800 nm.

### 2.4. Biological tests

#### 2.4.1. Cytotoxicity

The human osteoblast-like cell line (SAOS-2) (DSMZ GmbH, DEU) was cultivated in McCoy's 5 A medium (PromoCell GmbH, DEU) and supplemented with 15% heat-inactivated fetal bovine serum (FBS) (PAA Laboratories GmbH, AUT), penicillin (20 U $mL^{-1}$, Sigma-Aldrich Corp., US) and streptomycin (20 µg $mL^{-1}$, Sigma-Aldrich Corp., US) at 37 °C and in a 5% $CO_2$ atmosphere. Cells were seeded onto 96-well plate (Techno Plastic Products AG, CH) at a density of 1 × $10^4$ cells $cm^{-2}$ and cultivated in this medium for 24 h. After 24 h, different concentration of PEGylated nanoparticles (1, 7, 14 mg/l) was pipetted into precisely counted volume of cultivation medium in order to obtain the required

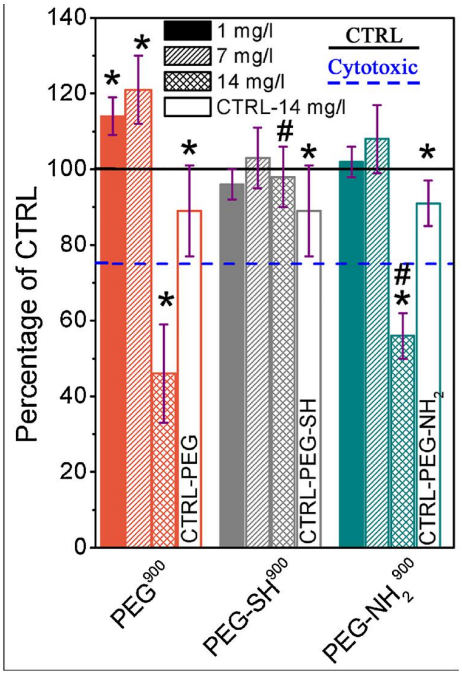


**Fig. 7.** Metabolic activity of osteoblasts incubated with different concentrations (1, 7 and 14 mg/l) of PEGylated Au NPs for 24 h. Relative values are expressed as a percentage of untreated cells (100%) (* represents significant difference to CTRL according to Wilcoxon matched-pairs test at $p < 0.05$; # represents significant difference to each PEG only treated cells (CTRL-14 mg/l) according to Wilcoxon matched-pairs test at $p < 0.05$.

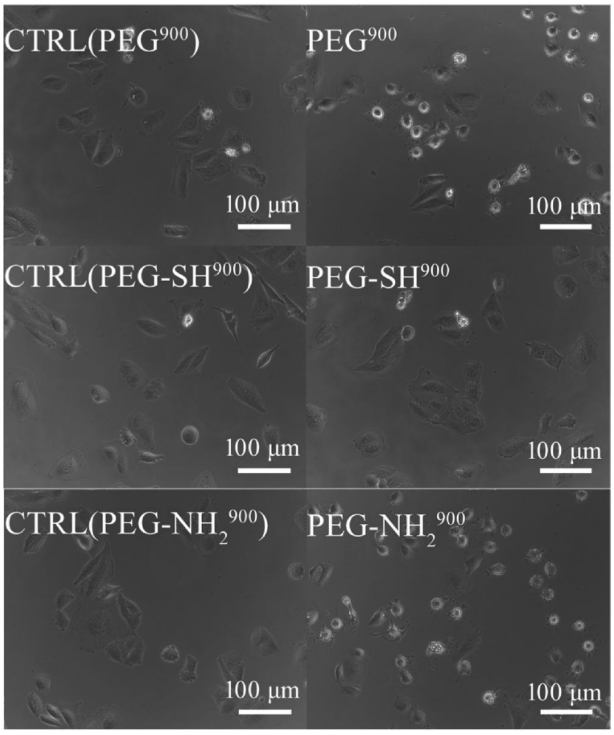


**Fig. 8.** Microscopic images of osteoblasts incubated with 14 mg/l concentrations of Au for 24 h prepared by 900 s of Au sputtering into $PEG^{900}$, PEG–$SH^{900}$ and PEG–$NH_2{}^{900}$. Relative values are presented as a percentage of untreated cells (CTRL).

dilution in the required volume. Such mixture was vortexed well prior to addition to cells. The medium from adhered cells on 96-well dish was discarded and the new medium mixed with PEGylated nanoparticles was added to the cells. The cells were then returned to incubator for 24 h treatment. Next, the images were taken and metabolic activity was determined.

Phase contrast images of the cells were acquired using an Eclipse Ti-S microscope (Nikon Inc., JPN) with a Plan Fluor 10x (N.A. 0.30) objective and DS-U2 digital camera (Nikon Inc., JPN).

The cell metabolic activity test (Cell Titer 96 AQueous One Solution Cell Proliferation Assay, MTS, Promega Corp., US) was performed according to the standard protocol. Absorbance was determined using a multi-detection micro-plate reader (Synergy™ 2, BioTek Instruments, Inc., US). The results were normalized (in percentage) with respect to the control cells with no NPs added.

Statistical analysis was performed using STATISTICA (StatSoft, s.r.o., CZ) software from two independent experiments performed in triplicate. The nonparametric Wilcoxon matched pairs test was used in order to determine significant differences (P values of less than 0.05) between the datasets of the untreated control and the rest of the variables and between datasets of the particular PEG treated control and the corresponding Au NPs modified by PEG.

### 2.4.2. Antibacterial activity

We have tested *in vitro* antibacterial activity of PEGylated Au NP stabilized by PEG, PEG-SH and PEG-$NH_2$. As a control (CTRL) of antibacterial activity, the stabilization media without NPs were used. The antibacterial screening was performed by disc diffusion method (zone of inhibition) similarly as described in Bauer et al. against gram-negative environmental bacterial strain of *Escherichia coli* (DMB 3138) and gram-positive environmental bacterial strain of *Staphylococcus epidermidis* (DBM 3179) [23]. Bacterial culture was grown overnight in Luria–Bertani (LB) broth medium at 37 °C in orbital shaker and optical density at 590 nm was measured. The culture in exponential phase of growth was serially diluted in fresh LB broth medium. The bacterial suspension with optical density of 1.0 was aseptically spread onto Petri dishes (using a sterile swab) containing pre-dried LB agar for E coli and PCA for SE. After air-drying, the tested soaked sterile discs for microbiology (diameter of 10 mm, Sigma Aldrich) were placed at the seeded plates. Then the plates were incubated for 24 h under static conditions at laboratory temperature (24 °C) for *E. coli* and 37 °C for *S. epidermidis*. The diameter of zone of inhibition produced by the tested materials was measured after 24 h using. Each sample was used in triplicate for the determination of antibacterial activity.

## 3. Results and discussion

This work was aimed to determine the optimum sputtering conditions for preparation of stable and non-cytotoxic PEGylated Au NPs for possible drug delivery applications. Preparation of the PEGylated Au NPs was carried out using the Au cathode sputtering into pure, thiol and amine terminated PEGs method.

TEM images in Fig. 1 shows the Au NPs prepared in all the functionalized PEG types. In all the samples the nanoparticles had a spherical shape, but the different functionalization showed an effect on the concentration and size of the nanoparticles as can be seen in Table 1 and in Fig. 1 insets. The deposition of Au for 300 s and 900 s into pure PEG led to NPs of 5.6 and 5.9 nm diameter in average. TEM images show that these nanoparticles have the worst size distribution and they create agglomerates. TEM images $PEG^{300}$ and $PEG^{900}$ are part of our previous study (see Ref. [21]. The Au NPs sputtered into the solution of PEG-SH for 300 and 900 s had average diameter of 1.5 and 1.6 nm, respectively. Both PEG–$SH^{300}$ and PEG–$SH^{900}$ NPs exhibit extremely high homogeneity of size distribution. Sputtering of Au into PEG–$NH_2$ leads to NPs with average diameter of 2.5 and 2.9 nm and the size distribution gets wider. Gold concentration in the colloid

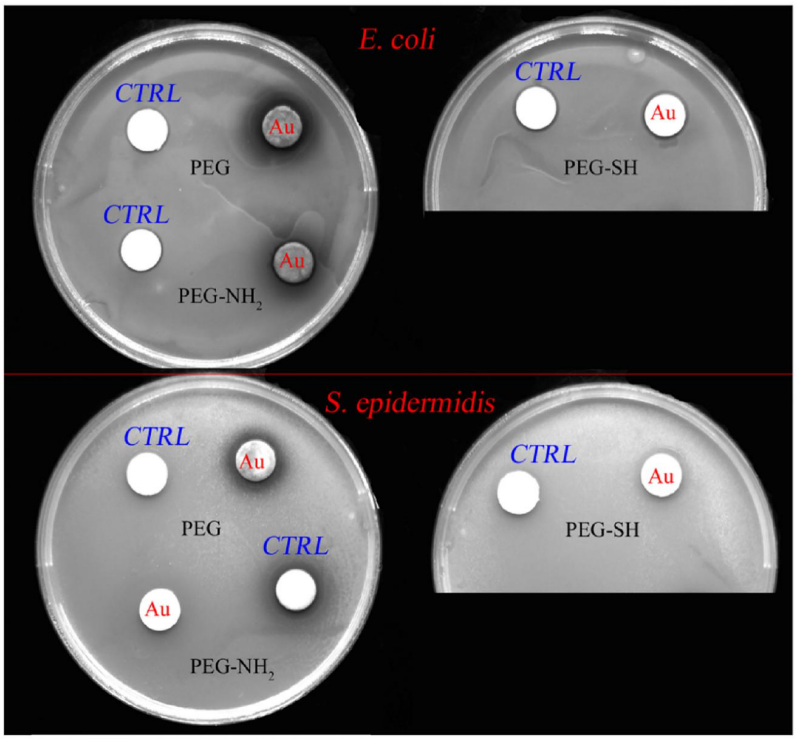


**Fig. 9.** Photographs of antibacterial disc tests of PEGylated Au NPs prepared by 900 s of Au sputtering into $PEG^{900}$, $PEG–SH^{900}$ and $PEG–NH_2{}^{900}$.

dispersion influences optical properties of each sample. When Au NPs are exposed to light, the electromagnetic radiation causes the free electrons of the Au NP to collectively coherently oscillate and absorb the light of appropriate wavelength. This is called surface plasmon resonance (SPR) [24]. Thus, gold colloids can appear in red, blue, green, or brown color according to the particle size and shape. The extinction coefficients of gold nanoparticles are typically four or five orders of magnitude higher than those of conventional dyes [25]. In our case the sputtering of Au into thiol or amine terminated PEG resulted in change of the solution color from brown to red (lighter or darker according to the Au NPs concentration). HRTEM images of Au NPs sputtered into $PEG^{900}$, $PEG–SH^{900}$ and $PEG–NH_2{}^{900}$ are presented in Fig. 2. At higher resolution, the arrangement of gold atoms in PEGylated NP can be observed. HRTEM showed that some of the Au NPs have icosahedral shape [26]. Although this is one of the most common shape of NPs prepared by vapor deposition and electrochemical methods [27–29], the majority of observed NPs have round or irregular shape often with signs of multiple twinning. However, more detailed study of particles morphology was limited by a fast contamination of particles under the electron beam.

To confirm results of NPs' size and distribution obtained from TEM measurements, dynamic light scattering (DLS) analysis was performed (see Fig. 3). Size of PEGylated Au NPs and their polydispersity index is listed in Table 1. The prepared PEGylated Au NPs were found to have very narrow distribution of sizes (see Table 1). No apparent aggregation of the NPs was observed, which was shown in TEM images as well (Fig. 1). The advantage of the DLS method is that all particles in the colloidal dispersions are included in the calculation, which leads to more statistically significant values. The results of DLS analysis are very sensitive to presence of large Au NP agglomerates since the analysis leads to intensity-weighted values. Another reason for disparity between the DLS and the TEM results is that the DLS method measures the size of NPs including their solvation shell as well and so the detected NP sizes are also influenced by the PEG corona [30]. Number weighted averages could in this case influence the obtained data significantly. Other research groups have obtained similar results for these systems [31].

The UV–vis absorption spectra of the prepared PEGylated Au NPs (fresh dispersions) are presented in Fig. 4. The resonance frequency of SPR depends on particle shape, size, and inter-particle distance and the surrounding environment [32]. The single narrow SPR band in the spectrum suggests presence of spherical NPs of 3–50 nm diameter. UV–vis spectra of $PEG^{300}$ and $PEG^{900}$ are used for comparison as a standard. SPR band of $PEG^{300}$ and $PEG^{900}$ is located at 513 nm. The disappearance of plasmon related absorption in the case of $PEG–SH^{300}$ and $PEG–SH^{900}$ results from NPs' size. Au NPs (or Au clusters) of size below 3 nm lose the metallic behavior and a gap between their conduction and valence orbitals originating from the small particle size (Kubo gap) appears. [32]. Decreasing particle size leads to an exponential increase of surface to volume ratio, thus making the nanomaterial surface more reactive to (i) other particles (aggregation) and (ii) its surrounding environment (biological components). Stabilization of Au NPs by $PEG–NH_2$ resulted in blue shift of SPR band to 501 nm. This shift can be attributed to change of refractive index of the solvent and especially the solvation shell. Moreover, differences in width of SPR bands of each sample were observed as well. Generally, it can be stated that the broader is the SPR band the worse is the size distribution (see Fig. 1). Values of absorbance (optical properties) depend not only on metal concentration in colloidal dispersion, but also on the type/chemical composition of the capturing media (PEG, PEG–SH and $PEG–NH_2$).

Results of AAS study of Au concentration in the prepared colloids with aging time ($1^{st}$, $6^{th}$ and $14^{th}$ day) is in Table 2. The concentration of Au grows linearly with rising deposition time and does not change over the aging time. Slight deviations of Au concentration in samples with the same sputtering and aging time are within measurement error. Color and absorption spectra of the colloids are affected by the Au concentration (see Figs. 1 and 4).

One of many important factors for possible biological application of PEGylated Au NPs is their stability. To investigate aging and temperature stability of the samples, we have chosen the AuNP colloids with sputtering time of 900 s, since these samples have suitable Au concentration for biological testing. Aging stability of PEGylated Au NPs in the period from 1st to 14th day has been studied by UV–vis spectroscopy (see Fig. 5). During the aging of $PEG^{900}$ a slight red shift from 513 to 519 nm has occurred. This is caused by formation of Au NPs agglomerates (*i.e.* increase of particle diameter) in the colloidal solution over the aging process [33]. In the $PEG\text{-}SH^{900}$ sample a modest decrease of absorbance with aging is observed – a minor instability of $PEG\text{-}SH^{900}$ dispersion was detected. In contrast to that, an increase of absorbance of $PEG\text{–}NH_2{}^{900}$ sample during the aging occurred. The change in absorbance might be attributed to the surrounding environment and its dielectric properties or to changes in NPs' size distribution. Increase of absorbance might be caused by change of refractive index on the Au NP/PEG–$NH_2$ interface because of amine groups on NPs' surface density increase during the aging process.

For drug delivery, and biomedical applications in general, it is important to know the temperature stability of colloidal dispersions. For temperature stability of the PEGylated Au NPs, six different temperatures were chosen: 4 °C (storage temperature), RT (standard), 37 °C (simulation of body temperature), 60 °C, 70 °C and 100 °C (sterilization temperature). The progress of the studied samples' thermal stability measurement (after 1 h) is documented by UV–vis absorption spectra in Fig. 6. The top left picture shows that all studied Au dispersions are stable at 4 °C. The absorbance does not change during the procedure and the spectra for RT and 4 °C overlap. The $PEG^{900}$ and $PEG\text{-}SH^{900}$ samples showed good temperature stability and only mild decrease of absorbance. An increase of absorbance of PEG-$NH_2$ might be caused by increase of optical density of solvation shell of the NPs that might be accelerated during temperature stress, as was stated before. However, a longer-term study of the temperature stress of the PEGylated Au NPs needs to be done.

The stability of the systems can be also characterized by the zeta potential values, which is commonly used as an indicator of stability of particle suspensions and colloidal samples. In principle, a high zeta potential (either positive or negative) should provide sufficient repulsive energy to the particles to maintain particle distance and protect sample stability by preventing flocculation and aggregation. If the absolute value of zeta potential is high, for example 50 mV, the dispersions are very stable due to electrostatic repulsion forces between the particles. Conversely, if the zeta potential is low, close to zero, particle coagulation is very fast and causes rapid sedimentation. Systems with zeta potential around ± 30 mV present moderate stability, around ± 50 mV a good stability and ≥ ± 60 mV an excellent stability [14,30,34,35]. The data in the Table 3 suggest all the tested systems should be sufficiently stable. Introduction of the polar groups (thiol- and especially amino-) leads to improvement of the system stability. During the aging, the colloid dispersions measurement remained stable except a slight decrease of stability in the case of PEG–SH. These results are in agreement with the results obtained by UV–vis (see Fig. 5).

To test possible application of PEGylated Au NP for drug delivery *in vitro* or *in vivo*, prepared nanoparticles were administered to human cell line of osteoblasts and possible cytotoxic effect of different NP concentrations was evaluated after 24 h (Fig. 7). The controls for each nanoparticle concentration with just PEG solutions without nanoparticles were performed and are stated in Fig. 7 as a control columns. It is apparent that control solution does not cause cytotoxicity (metabolic activity is bigger than 75% of CTRL (cells without any treatment)). The results obtained from the control solution measurements were compared with the results obtained for the samples with the highest concentration of PEGylated Au NPs (*i.e.* 14 mg/l). Stimulation of metabolic activity by low concentrations of nanoparticles (7 mg/l) for $PEG^{900}$ and PEG-$NH_2{}^{900}$ was observed. With respect to doubling time of these cells, which is 48 h, 24 h time interval when we see the increase of cell metabolic activity (activity of mitochondrial dehydrogenases) cannot be caused by increased cell proliferation but by different mitochondrial activity (respiration). Experiments with mitochondrial specific fluorescent dyes can provide an explanation, but these tests would reach out of the scope of this study. Cytotoxic effect (reduction of metabolic activity under 75% of control [36]) was determined only in the cells treated with the highest concentration (14 mg/l) of $PEG^{900}$ and $PEG\text{–}NH_2{}^{900}$, whereas no cytotoxic effect was apparent for $PEG\text{–}SH^{900}$. These effects can be related to the size of the particles, which is crucial for NP-cell interactions [37]. It can be speculated that tested NPs of different sizes (larger $PEG^{900}$ and $PEG\text{–}NH_2{}^{900}$ of diameter about 3 and 6 nm, respectively, and smaller $PEG\text{–}SH^{900}$ of diameter about 1.5 nm) can enter the cell by different way and thus affect the cells differently. For bigger particles, endocytic pathway influencing cellular metabolic activity can be proposed, however for ultra-small NPs the direct penetration through the membrane can be employed. Moreover, Au NPs with hydrodynamic size less than 5 nm were described to gain access to the cell nucleus [38], thus their effect can be observable after longer time than currently used 24 h interval. Another possible explanation of determined effect can be related to the charge of the PEGylated Au NPs. Despite detected negative zeta potential in water (Table 3), zeta potential in physiological media, including cell growth medium can be different (closer to zero) [39] thus decreased stability of the colloids can be induced. It was also observed that PEGylation of Au NPs contributed to minimal uptake of such particles into different cell types [40]. However, positive amine group (–$NH_2$) on PEGylated NPs induced their increased uptake to various cell lines (phagocytic and non-phagocytic) [41].

Cytotoxic effect detected by metabolic activity determination (Fig. 8) was proved also by light microscopy, where round and very bright cells were detected in samples treated with $PEG^{900}$ and $PEG\text{–}NH_2{}^{900}$, while healthy looking cells were presented in sample treated with $PEG\text{-}SH^{900}$ and all the controls (solutions of only PEG, PEG–SH and PEG–$NH_2$ without Au NPs). These solutions were used as internal controls for individual PEGylated Au NPs, at exactly the same volume of different PEG solutions as in case of the highest concentration of Au NPs in the particular PEG solution. In Fig. 8 it is demonstrated that the reduced metabolic activity was determined in all PEG only solution samples. Interestingly, solution of $PEG\text{–}SH^{900}$ reduced metabolic activity of the cells more than Au NP in this solution, whereas solution of $PEG\text{–}NH_2{}^{900}$ was less toxic than Au NP in this particular solution. Statistically there was no difference between reduction of metabolic activity of $PEG^{900}$ solution and Au NP in this solution.

For drug delivery applications besides cytotoxicity of PEGylated Au NPs knowledge of antibacterial properties of NPs is also important. Bactericide tests were performed against *E. coli* and *S. epidermidis* as the most common representatives of gram (-) and gram (+) bacterial strains. Results of antibacterial disc tests of PEGylated Au NPs prepared by 900 s of Au sputtering into $PEG^{900}$, $PEG\text{–}SH^{900}$ and $PEG\text{–}NH_2{}^{900}$ are shown in Fig. 9. As a control (CTRL) of antibacterial activity, each polyethylene glycols without NPs were used. Neither of the AuNP types showed any significant antibacterial action. Dark areas near the $PEG^{900}$ and $PEG\text{–}NH_2{}^{900}$ samples are due to diffusion of the colloid from disc into the agar (not an actual inhibition zone of bacterial growth around the disc). Diffusion of the colloid was not observed for the $PEG\text{-}SH^{900}$ sample because the colloid appeared colorless in this case. On the other hand, $PEG\text{-}SH^{900}$ showed a mild antibacterial effect. This type of the prepared NPs was identified by TEM as the smallest (see Table 1). According to the literature, NPs of smaller sizes show a stronger antibacterial effect [42,43]. Nevertheless, Au NPs have generally a negligible antibacterial effect compared to the Ag NPs, which depends on the size and size distribution of the nanoparticles [44].

## 4. Conclusion

The main goal of this work was to determine the optimal sputtering conditions for preparation of stable and non-cytotoxic PEGylated Au NPs

for possible drug delivery applications. Sputtering of Au for 300 and 900 s into pure, thiol and amine terminated PEGs leads to Au NPs with solvation shells composed of the used PEGs. The successful formation of the spherical NPs was observed by TEM/HRTEM. The size of the prepared Au NPs was found to be 1.5–5.9 nm and is dependent on the functionalization of the used PEG. DLS measurement confirmed results of NPs' size and size distribution (polydispersity index) obtained from TEM analysis. The characteristic SPR absorption was lost in the case of NPs smaller than 3 nm because of the small NP which loses its metallic character. Stabilization of Au NPs by PEG–$NH_2$ resulted in blue shift of SPR band to 501 nm. Blue shift of SPR band can be attributed to change of refractive index of the solvent and especially the solvation shell. AAS analysis showed that the Au concentration increases linearly with increasing deposition time and does not change over the aging time. During the aging of $PEG^{900}$ and PEG-$SH^{900}$ samples a slight red shift and modest absorption decrease was observed. On contrary, an increase of absorbance of PEG–$NH_2{}^{900}$ sample during the aging occurred. Since AAS analysis proves that Au concentration did not change over the aging time, the change in absorbance might be due to: (i) the surrounding environment and (ii) increase of density of amine groups on NPs' surface during the aging. UV–vis spectra showed that all studied Au dispersions are stable at 4 °C. The absorbance does not change during the procedure and the spectra for RT and 4 °C overlap. The $PEG^{900}$ and PEG-$SH^{900}$ samples showed good temperature stability and only mild decrease of absorbance. Increase of absorbance of PEG-$NH_2$ was observed during the thermal stability test as well. Zeta potential measurements confirmed that during the aging, the dispersions remained stable except for a slight instability of PEG–SH sample. Cytotoxic effect on osteoblastic cells was determined only with the highest concentrations of Au NPs stabilized by $PEG^{900}$ and PEG-$NH_2{}^{900}$ used, however Au PEG-$SH^{900}$ particles did not affected metabolic activity and viability of these cells. No significant antibacterial effect of any type of PEGylated Au NPs has been demonstrated. PEGylated Au NPs stabilized by PEG-SH showed the highest size and shape homogeneity, good temperature and aging stability, no cytotoxicity and antibacterial activity, which makes them very promising candidates for drug delivery carriers.

## Conflict of interest

The authors declare no competing financial interest.

## Acknowledgements

The authors gratefully acknowledge the Czech Science Foundation (GA CR) (Grant No. 17-00939S) for the financial support of this research work. Authors are also thankful for the financial support of Ministry of Health of Czech Republic under the project 15-32497A and PROGRES Q26 provided by Charles University.

## References

[1] Y.C. Yeh, B. Creran, V.M. Rotello, Gold nanoparticles: preparation, properties, and applications in bionanotechnology, Nanoscale 4 (2012) 1871–1880.
[2] I. Capek, Polymer decorated gold nanoparticles in nanomedicine conjugates, Adv. Colloid Interface Sci. 249 (2017) 386–399.
[3] X. Liu, M. Knauer, N.P. Ivleva, R. Niessner, C. Haisch, Synthesis of core-shell surface-enhanced Raman tags for bioimaging, Anal. Chem. 82 (2010) 441–446.
[4] T.L. Doane, Y. Cheng, A. Babar, R.J. Hill, C. Burda, Electrophoretic Mobilities of PEGylated gold NPs, J. Am. Chem. Soc. 132 (2010) 15624–15631.
[5] Y. Cheng, A.C. Samia, J.D. Meyers, I. Panagopoulos, B. Fei, C. Burda, Highly efficient drug delivery with gold nanoparticle vectors for *in Vivo* photodynamic therapy of cancer, J. Am. Chem. Soc. 130 (2008) 10643–10647.
[6] E. Roduner, Size matters: why nanomaterials are different, Chem. Soc. Rev. 35 (2006) 583–592.
[7] G. Mie, Beiträge zur optik trüber medien, speziell colloidaler metallösungem, Ann. Phys. 25 (1908) 377–445.
[8] J. Turkevich, P.C. Stevenson, J. Hillier, A study of the nucleation and growth processes in the synthesis of colloidal gold, discuss, Faraday Soc. 11 (1951) 55–75.
[9] M. Brust, M. Walker, D. Bethell, D.J. Schiffrin, R. Whyman, Synthesis of thiol-derivatized gold nanoparticles in a 2-phase liquid-liquid system, J. Chem. Soc. Chem. Comm. 7 (1994) 801–802.
[10] H. Wender, P. Migowski, A.F. Feil, S.R. Teixeira, J. Dupont, Sputtering deposition of nanoparticles onto liquid substrates: recent advances, Coord. Chem. Rev. 257 (2013) 2468–2483.
[11] Y. Hatakeyama, J. Kato, T. Mukai, K. Judai, K. Nishikawa, Effect of adding a thiol stabilizer on synthesis of Au nanoparticles by sputter deposition onto poly(ethylene glycol), Bull. Chem. Soc. Jpn. 87 (2014) 773–779.
[12] T. Torimoto, K. Okazaki, T. Kiyama, K. Hirahara, N. Tanaka, S. Kuwabata, Sputter deposition onto ionic liquids: simple and clean synthesis of highly dispersed ultrafine metal nanoparticles, Appl. Phys. Lett. 89 (2006) 243117.
[13] Y. Hatakeyama, T. Morita, S. Takahashi, K. Onishi, K. Nishikawa, Synthesis of Gold Nanoparticles in liquid polyethylene glycol by sputter deposition and temperature effects on their size and shape, J. Phys. Chem. C 115 (2011) 3279–3285.
[14] T.L. Doane, C.H. Chuamg, R.J. Hill, C. Burda, Nanoparticle ζ-potentials, Acc. Chem. Res. 45 (2012) 317–326.
[15] A. Reznickova, Z. Novotna, O. Kvitek, Z. Kolska, V. Svorcik, Gold, silver and carbon nanoparticles grafted on activated polymers for biomedical applications, J. Nanosci. Nanotechnol. 15 (2015) 10053–10073.
[16] B. Pelaz, P. del Pino, P. Maffre, R. Hartmann, M. Gallego, S. Rivera-Fernandez, J.M. de la Fuente, G.U. Nienhaus, W.J. Parak, Surface functionalization of nanoparticles with polyethylene glycol: Effects on protein adsorption and cellular uptake, ACS Nano 9 (2015) 6996–7008.
[17] F. Lu, T.L. Doane, J.J. Zhu, C. Burda, A method for separating PEGylated Au nanoparticle ensembles as a function of grafting density and core size, Chem. Commun. 50 (2014) 642–644.
[18] A. Albanese, P.S. Tang, W.C.W. Chan, The effect of nanoparticle size, shape, and surface chemistry on biological systems, Annu. Rev. Biomed. Eng. 14 (2012) 1–16.
[19] G.Y. Liu, Q.Q. Luo, H.B. Wang, W.H. Zhuang, Y.B. Wang, In situ synthesis of multidentate PEGylated chitosan modified gold nanoparticles with good stability and biocompatibility, RSC Adv. 5 (2015) 70109–70116.
[20] K. Knop, R. Hoogenboom, D. Fischer, U.S. Schubert, Poly(ethylene glycol) in drug delivery: pros and cons as well as potential alternatives, Angew. Chem. Int. Ed. 49 (2010) 6288–6308.
[21] A. Reznickova, P. Slepicka, N. Slavikova, M. Staszek, V. Svorcik, Preparation, aging and temperature stability of PEGylated gold nanoparticles, Colloid. Surf. A 523 (2017) 91–97.
[22] P. Slepicka, R. Elashnikov, P. Ulbrich, M. Staszek, Z. Kolska, V. Svorcik, Stabilization of sputtered gold and silver nanoparticles in PEG colloid solutions, J. Nanopart. Res. 17 (2015) 1–15.
[23] A.W. Bauer, W.M. Kirby, J.C. Sherris, M. Turck, Antibiotic susceptibility testing by a standardized single disk method, Am. J. Clin. Pathol. 45 (1966) 493–496.
[24] X. Huang, M.A. El-Sayed, Gold nanoparticles: optical properties and implementations in cancer diagnosis and photothermal therapy, J. Adv. Res. 1 (2010) 13–28.
[25] P.K. Jain, K.S. Lee, I.H. El-Sayed, M.A. El-Sayed, The influence of size, shape, and dielectric environment, J. Phys. Chem. B 110 (2006) 7238–7248.
[26] M.J. Yacamán, J.A. Ascencio, H.B. Liu, J. Gardea-Torresdey, Structure shape and stability of nanometric sized particles, J. Vac. Sci. Technol. B 19 (2001) 1091–1103.
[27] J.L. Gardea-Torresdey, K.J. Tiemann, G. Gamez, K. Dokken, S. Tehaucanero, M.J. Yacaman, Gold nanoparticles obtained by bio-precipitation from gold(III) solutions, J. Nanopart. Res. 1 (1999) 397–404.
[28] R. de Wit, Partial disclinations, J. Phys. C: Solid State Phys. 5 (1972) 529–534.
[29] Y.H. Chui, G. Grochola, I.K. Snook, S.P. Russo, Molecular dynamics investigation of the structural and thermodynamic properties of gold nanoclusters of different morphologies, Phys. Rev. B 75 (2007) 033404.
[30] V. Uskokovic, Dynamic light scattering based microelectrophoresis: main prospects and limitations, J. Dispersion Sci. Technol. 33 (2012) 1762–1786.
[31] T.G.F. Souza, V.S.T. Ciminelli, N.D.S. Mohallem, A comparison of TEM and DLS methods to characterize size distribution of ceramic nanoparticles, J. Phys. Conf. Ser. 733 (2016) 012039.
[32] E. Boisselier, D. Astruc, Gold nanoparticles in nanomedicine: preparations, imaging, diagnostics, therapies and toxicity, Chem. Soc. Rev. 38 (2009) 1759–1782.
[33] A. Mayoral, H. Barron, R. Estrada-Salas, A. Vazquez-Duran, M.J. Yacamán, Nanoparticle stability from the nano to the meso interval, Nanoscale 2 (2010) 335–342.
[34] M. Kosmulski, Chemical Properties of Material Surfaces, Marcel Dekker Inc., New York, 2001.
[35] P. Hiemenz, R. Rajagopalan, Principles of Colloid and Surface Chemistry, Marcel Dekker Inc., New York, 1997.
[36] E. Flahaut, M.C. Durrieu, M. Remy-Zolghadri, R. Bareille, C. Baquey, Investigation of the cytotoxicity of CCVD carbon nanotubes towards human umbilical vein endothelial cells, Carbon 44 (2006) 1093–1099.
[37] M.C. Senut, Y.H. Zhang, F.C. Liu, A. Sen, D.M. Ruden, G.Z. Mao, Size-dependent toxicity of gold nanoparticles on human embryonic stem cells and their neural derivatives, Small 12 (2016) 631–646.
[38] Y.J. Gu, J.P. Cheng, C.C. Lin, Y.W. Lam, S.H. Cheng, W.T. Wong, Nuclear penetration of surface functionalized gold nanoparticles, Toxicol. Appl. Pharm. 237 (2009) 196–204.
[39] A.C. Sabuncu, J. Grubbs, S. Qian, A. Beskok, Probing nanoparticle interactions in cell culture media, Colloid. Surface B 95 (2012) 96–102.
[40] K. Kettler, K. Veltman, D. Van De Meent, A. van Wezel, A.J. Hendriks, Cellular uptake of nanoparticles as determined by particle properties, experimental conditions and cell type, Environ. Toxicol. Chem. 33 (2014) 481–492.
[41] M.R. Lorenz, V. Holzapfel, A. Musyanovych, K. Nothelfer, P. Walther, H. Frank, K. Landfester, H. Schrezenmeier, V. Mailander, Uptake of functionalized, fluorescent-labeled polymeric particles in different cell lines and stem cells, Biomaterials 27 (2006) 2820–2828.
[42] E. Lima, R. Guerra, V. Lara, A. Guzman, Gold nanoparticles as efficient antimicrobial agents for Escherichia coli and Salmonella typhi, Chem. Cent. J. 7 (2013) 11.
[43] Y. Rao, G.K. Inwati, M. Singh, Green synthesis of capped gold nanoparticles and their effect on Gram-positive and Gram-negative bacteria, Future Sci. OA 3 (2013) FSO239.
[44] J. Siegel, K. Kolarova, V. Vosmanska, S. Rimpelova, J. Leitner, V. Svorcik, Antibacterial properties of green-synthesized noble metal nanoparticles, Mater. Lett. 113 (2013) 59–62.

**Publication E**

Machova, Iva, Martin Hubalek, **Tereza Belinova**, Anna Fucikova, Stepan Stehlik, Bohuslav Rezek, and Marie Hubalek Kalbacova. "**The Bio-Chemically Selective Interaction of Hydrogenated and Oxidized Ultra-Small Nanodiamonds with Proteins and Cells**." Carbon (2020), IF = 8.821

Carbon 162 (2020) 650–661

Contents lists available at ScienceDirect

Carbon

journal homepage: www.elsevier.com/locate/carbon

# The bio-chemically selective interaction of hydrogenated and oxidized ultra-small nanodiamonds with proteins and cells

Iva Machova [a], Martin Hubalek [b, *], Tereza Belinova [a], Anna Fucikova [c], Stepan Stehlik [d], Bohuslav Rezek [e], Marie Hubalek Kalbacova [a, f, **]

[a] Biomedical Center, Faculty of Medicine in Pilsen, Charles University, Pilsen, 32300, Czech Republic
[b] Institute of Organic Chemistry and Biochemistry of the Czech Academy of Sciences, Prague, 16610, Czech Republic
[c] Department of Chemical Physics and Optics, Faculty of Mathematics and Physics, Charles University, Prague, 21216, Czech Republic
[d] Institute of Physics of the Czech Academy of Sciences, Prague, 18221, Czech Republic
[e] Faculty of Electrical Engineering, Czech Technical University, Prague, 16627, Czech Republic
[f] Institute of Pathological Physiology, First Faculty of Medicine, Charles University, Prague, 12853, Czech Republic

ARTICLE INFO

*Article history:*
Received 3 January 2020
Received in revised form
18 February 2020
Accepted 20 February 2020
Available online 27 February 2020

ABSTRACT

Ultra-small nanoparticles of a size smaller than or comparable to cell membrane pores (1–5 nm) offer significant potential in the field of biomedicine. This study presents a systematic *in vitro* investigation of fundamental bio-chemical interactions of such ultra-small hydrogenated and oxidized detonation nanodiamonds (DNDs) with biomolecules and human cells. We apply mass spectrometry methods (LC-MS/MS) for the qualitative and quantitative analysis of the protein corona as a function of the surface chemistry and size of DNDs. We observe that protein interactions with DNDs are more related to their surface chemistry (H/O-termination) rather than size. Bioinformatics characterization of the identified proteins points to the strong influence of electrostatic interaction between proteins and DNDs depending on their termination. Such specific interaction leads to formation of different protein corona on 2 nm DNDs, which influences also interaction with cells including different level of cytotoxicity.



## 1. Introduction

Nanoparticles (NPs) of various materials offer the potential to enable key advancements in the field of modern medicine and are currently being subjected to investigation with respect to a range of applications. The fundamental parameters that need to be considered in terms of the application of NPs consist of size, shape, surface chemistry and charge, all of which predetermine the properties of NPs and their behaviour in various environments [1].

Detonation nanodiamonds (DNDs) comprise an outstanding nanomaterial that provides the superior properties of bulk diamonds at the nanoscale. Nowadays, the DNDs are routinely produced by detonation of oxygen-deficient explosives such as trinitrotoluene and hexogen mixture (40:60) in a detonation chamber in inert environment such as Argon atmosphere. The DNDs are available at competitive price and are characteristic by a complex structure given by their detonation origin. A DND nanoparticle is often approximated by a diamond core, including various lattice defects, transient $sp^3/sp^2$ layer, and $sp^2$ surface shell that may carry various surface functional groups [2]. The biocompatibility, chemical stability, large surface area and broad possibilities of surface chemistry modification of DNDs in particular predetermine them for use in various biomedical applications *in vitro* [3] and *in vivo* [4] including imaging, drug and gene delivery, radiotherapy, etc. [2,5]. Conventional ~5 nm DNDs exhibit a very narrow size distribution range, are very stable and are less toxic than other carbon nanoparticles [6,7]. It was recently demonstrated that nanodiamonds remain structurally stable down to a size of 1 nm [8]. In addition, a high yield ultra-small (1–3 nm) DND preparation and characterization method is now available [9,10]. Such ultra-small nanodiamonds provide a non-toxic surface-tuneable nanoparticle model system with active and stable diamond lattice-related fluorescent abilities, that can be potentially used in a

* Corresponding author. Institute of Organic Chemistry and Biochemistry of the Czech Academy of Sciences, Prague, 16610, Czech Republic.
** Corresponding author. Institute of Pathological Physiology, First Faculty of Medicine, Charles University, Prague, 12853, Czech Republic.
*E-mail addresses:* martin.hubalek@uochb.cas.cz (M. Hubalek), marie.kalbacova@lf1.cuni.cz (M.H. Kalbacova).

https://doi.org/10.1016/j.carbon.2020.02.061
0008-6223/

broad range of biomedical applications such as molecular-like fluorescent marker [11].

With concern to medical applications, NPs interact with very complex media such as blood that consists of a large number of different molecules including proteins, amino acids, lipids, metabolites and electrolytes [12] and all these interactions exert a major influence on the properties and functions of NPs. Generally, the surfaces of most NPs are capable of the spontaneous binding of various biomolecules thus forming a so-called biomolecular corona and, in the case of proteins, a protein corona [13–15]. The encapsulation of NPs by the protein corona results in changes in the physicochemical properties of NPs and modulates their interaction with cells, which differs from interaction with bare NPs [15–17]. Moreover, adsorption of biomolecules onto NP surface from biological media and possible formation of NP aggregates cause difficulties in definition and measurement of NP size in the context of biology and other research is necessary [18]. *In vitro,* the standard cell cultivation medium is usually supplemented with fetal bovine serum (FBS) as the source of key cell growth modulating factors (growth factors, hormones, etc.), with various antibiotics and other specific cell-essential supplements. FBS comprises a natural mixture of proteins with differing characteristics that vary in terms of their amount, amino acid sequence, structural motifs, size and other physicochemical properties. Each of the characteristics determine the interaction of a given protein with NPs. Nevertheless, a thorough knowledge of the behaviour of ultra-small DNDs in the biological environment and the identification of proteins that spontaneously associate with their surface is essential with respect to their application in the field of biomedicine.

While the currently applied protein methodology allows for the identification of highly-presented proteins, cells are able to react specifically via ligand-receptor binding to proteins that are presented only in a small number of molecules. This very specific reaction may exert an important effect on cell behaviour and thus should be considered. The study of protein corona on NPs employs direct methods for the determination of protein adsorption, protein composition and protein quantification. Without the need to disrupt the NP-protein complexes, the structural arrangement of protein corona can be analysed using electron microscopy (transmission and scanning), atomic force microscopy (AFM) and variety of other methods [19]. The most straightforward technique for the qualitative identification of proteins consists of gel electrophoresis (SDS-PAGE) coupled with tandem mass spectrometry MS/MS [19]. The quantitative analysis of the composition of proteins is usually performed via liquid chromatography coupled with mass spectrometry (LC-MS/MS) [19,20]. The current stage of the development of the methodology allows the combination of the high sensitivity of protein identification with a label-free quantification strategy such as SWATH-MS (the sequential window acquisition of all the theoretical fragment ion spectra mass spectrometry) [21] for use in the corona analysis [22].

The protein corona is a dynamic system that is able to adapt to its environment over time via changes in its composition [23] and/or in the conformation of the protein, which may cause adverse biological effects including inflammation or complement activation [24,25]. NPs are able to induce structural changes in adsorbed proteins [26–28] which, in turn, play a significant role in cell signal transduction [26]. The interaction of proteins with NPs potentially plays two very distinct roles. On the one hand, due to repulsive forces between proteins they are capable of stabilizing nanoparticles in a colloidal solution (for example BSA is used to stabilize gold nanoparticles [29]), while, on the other, attraction or depletion forces may dominate and the proteins may drive the aggregation of the particles, which again changes the size and density of the particle protein complexes [30]. Moreover, the formation of large NP-protein aggregates may trap proteins that do not directly adsorb on the NP surface, i.e. they do not form part of the hard corona but "artificially" cover the particle and thus allow a broad spectrum of differing interactions with cells. Thus, investigation of composition of protein corona and protein-NPs interactions is fundamental for understanding of their biological effects.

Proteins in biological fluids typically have dimensions of 5–20 nm, whereas the size of commonly used NPs is in the range 10–100 nm (individual NPs or aggregates of small NPs). Therefore, the properties and interactions of proteins vary primarily with respect to the size of the NP, the surface chemistry and the material. Large NPs (above 20 nm) are larger than many proteins [31] and their extensive surface area allows for interaction with a large number of protein molecules. Conversely, small (<10 nm) or even ultra-small NPs (1–3 nm in diameter) are theoretically able to bind to just a single protein due to steric reasons [32]. In other words, the size of the NP may provide for selectivity for certain proteins. Ultra-small NPs of a diameter of 1–3 nm may potentially address specific epitopes on the protein surface or even the active centre of the enzyme [31,32]. In principle, the smaller the NP the more it is possible to consider targeted interaction. Nevertheless, experimental evidence of this behaviour is lacking and according to the NP characteristics (e.g. high surface energy) some ultra-small NPs can form clusters after their interaction with serum proteins. To date, only theoretical calculations have indicated the binding of single proteins to single NPs [24,32], whereas, in reality, this may not be the case even in solutions of single proteins since other factors (ionic strength, protein concentration, etc.) become involved. Moreover, the binding of one protein may mediate the binding of another protein and thus, in reality, clusters of proteins (even those not directly connected to NPs) may be formed, a development that cannot easily be predicted by theoretical studies. Several authors have demonstrated the higher level of protein association to smaller NPs, indicating that the surface area and curvature form the initiating properties for the capacity of proteins to bind to NPs [33].

The size of ultra-small NPs is *per se* ideal in terms of biomedical applications due to their potential ability to directly enter cells or even cell nuclei [34]. Furthermore, ultra-small NPs offer the potential advantage that they can be efficiently cleared from the organism via the renal system, i.e. NPs of a hydrodynamic diameter ($D_h$) of less than ~6 nm [35]. However, the adsorption of proteins, particularly the most abundant proteins present in serum, i.e. serum albumin (~7 nm) or immunoglobulin (~14 nm), may lead to an increase in the $D_h$ to such an extent that renders them too large for renal clearance [36,37]. Thus, it is necessary that the formation of the protein corona on NPs, especially on ultra-small NPs, as well as the effects of aggregation in cell culture media is experimentally characterised.

Therefore, this study investigated interactions between ultra-small 2 nm DNDs with differing surface chemistries and zeta potential (hydrogenated/positive and oxidized/negative) and a standard cell cultivation medium and, consequently, with cells. We conducted a thorough study of the composition of the protein corona that forms on the surfaces of DNDs as a function of the surface chemistry of ultra-small DNDs following interaction with complex materials such as FBS, but not following that with single proteins, so as to best approximate to *in vitro* conditions. Employing the LC-MS/MS approach, that reveals the diverse distribution (type and quantity) of proteins on hydrogenated and oxidized ultra-small DNDs, we observed qualitative as well as quantitative differences in terms of protein binding. We also investigated the effect of hydrogenated and oxidized ultra-small DNDs with and without protein corona on osteoblastic cell behaviour so as to observe the impact of specific protein corona and bare ultra-small DND surfaces on NP-cell interactions.

## 2. Experimental

### 2.1. The synthesis of ultra-small nanodiamonds

The preparation and characterization of water colloidal dispersions of ultra-small ~2 nm DNDs with oxidized and hydrogenated surfaces have been described elsewhere [9,10]. Briefly, a DND powder (New Metals and Chemicals, Japan) consisting of aggregated 4–6 nm DND particles was annealed at 450 °C for 30 min (surface oxidation) or at 520 °C for 50 min (size reduction + surface oxidation), thus resulting in ~4 and 2 nm oxidized O-DNDs, respectively. Such treated DND powders were then further hydrogenated by means of annealing in hydrogen at 600 °C for 6 h at the atmospheric pressure of pure hydrogen gas, resulting in 4 and 2 nm H-DNDs. Colloidal solutions of DNDs were prepared via the ultrasonication of the DND powder in deionized water (10 mg/mL) via a sonotrode (Hielscher UP200S, 1h, 200 W) and, subsequently, two-step centrifugation (Eppendorf Mini Plus, 1 + 1.5 h at 14000 RCF) in a 2 mL Eppendorf-type tube, following which 1 mL of the supernatant was separated using a micropipette.

### 2.2. Zeta potential and size determination

The DNDs (160 μg) were incubated overnight in DMEM and DMEM + 5% FBS under constant rotation conditions, whereupon the DND samples were washed five times in PBS by means of sequential centrifugation (1 x 2630 RCF, 1 x 10510 RCF and 3 x 20590 RCF). The resulting pellets were dissolved in 100 μl of PBS and further diluted in 1 ml of deionized water and analysed on a Malvern Zetasizer Nano ZS for ZP analysis purposes. Following initial measurement of such samples (denoted as "before sonication") the samples were sonicated softly for 15 min (reduction of waves to 10–20% of original intensity) and the ZP was measured once more (denoted as "after sonication") (Table 1). The size of DNDs with biomolecular corona originating from cell cultivation media was determined by dynamic light scattering (DLS) at angle of 173° on the same sample using the same Malvern Zetasizer Nano ZS DLS data processing was performed by the Malvern Zetasizer Nano ZS software and the volumetric size distributions were obtained (Supplementary Table 1).

### 2.3. Sample preparation for protein corona characterization

The conditions of protein corona characterisation were selected with the respect to the conditions of zeta potential determination. We made especially sure that the ratio of DNDs (both H- and O-terminated) and proteins (FBS concentration) was the same for both experiments. The H-DND and O-DND water suspensions were sonicated for 15 min in a sonication bath (Utrasonic Cleanar, UCE ultrasonic co, LDd. China, ultrasonic frequency - 40 kHz) prior to use. 80 μg of DND was mixed and incubated with 500 μl of DMEM medium with 5% FBS overnight under constant rotation conditions. The nanoparticles were pelleted via centrifugation (10 510 RCF, 30 min, 4 °C), washed in 500 μl PBS and centrifuged (10 510 RCF, 30 min, 4 °C). Washing in 500 μl PBS (20 590 RCF, 30 min 4 °C) was repeated three more times and the vials were changed after the first three centrifugation steps. Proteins attached to the nanoparticles were removed via the addition of 30 μl of 2x Laemmli sampling buffer (4% w/v SDS, 20% w/v glycerol, 3% v/v 2-mercaptoethanol, 100 mM Tris-HCl, pH 6.8, bromophenol blue) to the nanoparticle pellets. The samples were then heated for 15 min at 95 °C and sonicated for 15 min in an ultrasound bath. The combination of Laemmli buffer and heat disrupted the protein-nanoparticle non-covalent bonds thus allowing the protein analysis.

### 2.4. LC-MS/MS

Trypsin filter digestion in form of a eFASP (enhanced Filter-aided sample preparation) method [38] was employed for the analysis of the proteins associated with the DNDs. Briefly, the samples were reduced, alkylated and digested by trypsin on Microcon filters YM-10. The resulting peptides were then desalted on a C18 SPE column (PepClean, Thermo). The peptides were separated during LC-MS/MS using a nano-LC system (Ultimate 3000 RSLC nano, Dionex) on an Acclaim PepMap C18 column (75 μm Internal Diameter, 250 mm length) applying a 70 min acetonitrile elution gradient in 0.1% formic acid. The chromatographic column was connected via nanoESI to a tandem mass spectrometer (TripleTOF 5600, Sciex). The aim was to collect data for both the identification and quantification of the proteins in one measurement sequence; however, it was first necessary to calculate the optimal variable window length across the mass range ($m/z$ 350–1250) so as to maximize the performance of the measurement. We measured representative samples in a data-dependent manner in a mass range of $m/z$ 350–1250. The variable window calculator (Sciex) created a method consisting of 50 consecutive mass windows, the aim of which was to collect fragmentation spectra in a mass range of $m/z$ 100–1600. Employing two methods using the same chromatographic parameters but different mass spectrometric data collection setups (the first the data-dependent analysis (DDA) method and the second the data independent method (DIA – SWATH), we measured the samples in sequences of three consecutive runs of each sample (the first run aimed at collecting DDA data for protein identification purposes and the second and third for the collection of DIA data for the quantification thereof).

**Table 1**
**Zeta potential and FWHM of DNDs incubated in various solutions.** Values of zeta potential are presented as the mean ± s.d. from three measurements in water.

| | Before sonication | | | |
|---|---|---|---|---|
| | 2 nm O-DND | | 2 nm HDND | |
| | ZP (mV) | FWHM (mV) | ZP (mV) | FWHM (mV) |
| DND in water | −62.1 ± 1.0 | 7.6 | 61.9 ± 0.6 | 6.2 |
| DND in DMEM | −37.2 ± 1.3 | 9.0 | 4.9 ± 0.8 | 8.5 |
| DND in DMEM + 5% FBS | −33.6 ± 0.9 | 6.5 | −18.7 ± 0.3 | 4.0 |
| | After sonication | | | |
| | 2 nm O-DND | | 2 nm HDND | |
| | ZP (mV) | FWHM (mV) | ZP (mV) | FWHM (mV) |
| DND in water | −39.9 ± 1.0 | 6.7 | 57.6 ± 1.3 | 6.3 |
| DND in DMEM | −37.0 ± 0.1 | 8.1 | 14.3 ± 0.4 | 4.8 |
| DND in DMEM + 5% FBS | −34.3 ± 2.4 | 8.3 | −13.8 ± 5.3 | 5.3 |

### 2.5. Mass spectrometry data processing

The resulting DDA spectra were analysed by means of Protein Pilot software 4.5 (Sciex), and the Bos taurus reference Proteome UP000009136 database with the UniRef 100% identity (downloaded on 2 October 2018) was employed for protein identification purposes. All the samples were investigated independently in order to be able to evaluate the number of identified proteins separately for each sample. Conversely, the DDA data was investigated together so as to compile a complete library of the various proteins, peptides and fragments identified; the library was used for SWATH processing in PeakView 2.2 (Sciex). The retention time was aligned in all the samples by means of selecting the peptides common across the retention time range for all the samples. Up to 30 peptides per protein, 6 transitions per peptide, peptide confidence of 95% with a false discovery rate threshold of 1% were selected for quantitation purposes. All the peptides were manually confirmed and only proteins with at least 2 unique (not shared) peptides were allowed to remain in the data set. An error of 30 ppm and an extraction window of 3 min were selected. The final processing step resulted in an intensity of transitions, peptides and proteins. The final protein table was processed in MarkerView (Sciex) in order to compile a statistical evaluation. The Student T-test was performed on the monitored groups followed by the conducting of a principal component analysis.

The list of differently attached proteins was organized according to the respective biological process employing the gene ontology classification generated from the Panther [39] classification system database (PANTHER14.1 released 19-12-2018). The theoretical physicochemical properties of the proteins were calculated based on their protein sequences. The isoelectric point (pI) and molecular weight (MW) were computed via https://web.expasy.org/compute_pi/ [40] and the GRAVY index via http://www.gravy-calculator.de/index.php.

### 2.6. Cell cultivation

Human osteoblastic cells (SAOS-2, DSMZ, Germany) were cultivated over the long-term in standard McCoy's 5A medium (GE Healthcare - HyClone) supplemented with 15% of FBS (Biosera), L-glutamine (Life Technologies), 10 000 U $ml^{-1}$ of penicillin and 10 μg/ml of streptomycin (both Sigma-Aldrich) in a $CO_2$ humidified incubator at 37 °C.

### 2.7. Cytotoxicity (metabolic activity) determination

For the purposes of cytotoxicity testing, the osteoblastic cells were seeded in the standard cultivation medium at a concentration of 10 000 cells/$cm^2$ on 96-well plates and incubated for 24 h. The cells were then washed in phosphate buffer saline (PBS, Thermo Fisher Scientific - Gibco) followed by the addition of the appropriate DND-containing medium (5, 10, 25, 50 and 100 μg/ml). DNDs with both terminations were mixed either in Dulbecco's Modified Eagle Medium (DMEM, Thermo Fisher Scientific - Gibco) supplemented with 5% of FBS, or in the non FBS-supplemented medium, following which they were both added to cells which were then cultivated for 6 and 24 h. The medium containing the DNDs was discarded at each time point and fresh medium with 10% of tetrazolium stain (MTS, Cell Titer961 AqueousOne, Promega) was added to the cells, which were then incubated for 2 h in a $CO_2$ incubator at 37 °C. The optical density was measured by means of a microplate reader (Labsystem Multiskan MS) at 492 nm, subtracting the background at 620 nm. The values obtained were related to the corresponding controls (non-treated cells) in terms of percentage. In order to avoid cell inhibition and death caused by a lack of nutrients, FBS was added to all the non-supplemented samples after 6 h of incubation so as to attain a final concentration of 5%. The results obtained were statistically evaluated using the Statistica program (extreme and remote value subtraction based on box graphs, the non-parametric Wilcoxon matched-pairs test).

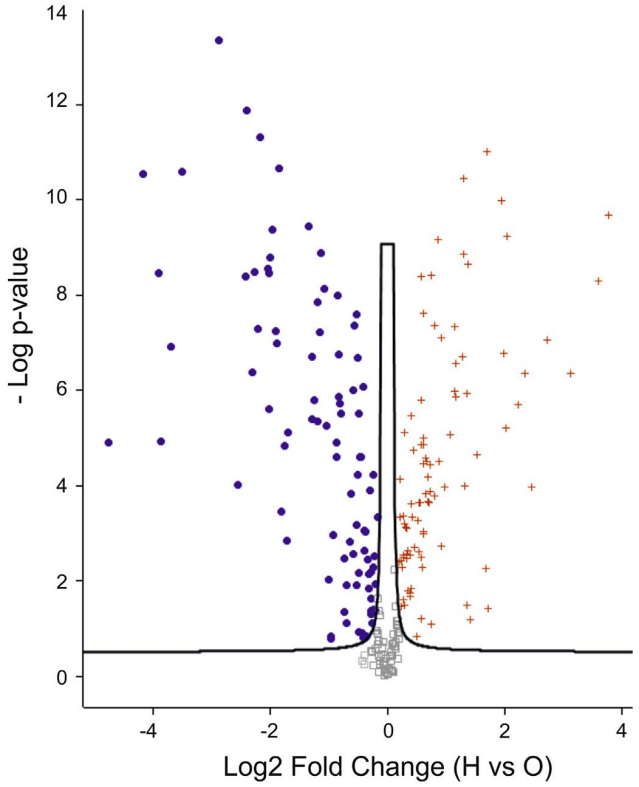


**Fig. 1. Mass spectrometry analysis.** Protein quantitative LC-MS/MS analysis depicted by Volcano plot that compares the fold change (Log2 Fold Change) of each identified protein and statistical significance (-Log p-value). The data of 242 proteins included in the SWATH library is presented. Blue dots represent proteins that are enriched on 2 nm H-DND, red crosses represent proteins enriched on 2 nm O-DND. Grey squares represent proteins that were found non-significantly on both DNDs. The analysed proteins originate from FBS.

### 2.8. Scanning electron microscopy (SEM)

For SEM measurement purposes, SAOS-2 cells were precultivated on 13 mm glass cover slides in 6-well plate in the standard cultivation medium for 24 h at a concentration of 10 000 cells/$cm^2$. The cells were then washed in PBS and DMEM medium supplemented with 5% of FBS to which 25 μg/ml of DNDs was added for 6 h. The medium was subsequently replaced by a medium with no DNDs and incubated up to 24 h. The cells were then washed in PBS and fixed in 2.5% glutaraldehyde (Sigma-Aldrich) in PBS at 4 °C overnight. Following fixation, the samples were dehydrated via an ethanol row (10 min, RT in 20%, 40%, 50%, 60%, 70%, 100% ethanol, acetone), dried using a critical point dryer (Bal-Tec CPD 030), covered with a 4 nm layer of chrome and observed by means of FEG SEM MAIA (Tescan).

## 3. Results and discussion

### 3.1. DNDs' characteristics

While basic characteristics such as the DLS size distribution in DI

**Table 2**
**SWATH: quantitative analysis of proteins enriched on 2 nm O-DNDs and 2 nm H-DNDs.** The table summarizes the distribution of proteins at least three fold increased on O-DNDs versus H-DNDs (fold change > 3) and their theoretical properties - molecular weight (MW), isoelectric point (pI) and hydrophobicity presented by GRAVY index. The analysed proteins originate from FBS.

| 2 nm O-DND | | | | | | 2 nm H-DND | | | | | |
|---|---|---|---|---|---|---|---|---|---|---|---|
| Accession | Name | Fold change | MW (kDa) | pI | GRAVY index | Accession | Name | Fold change | MW (kDa) | pI | GRAVY index |
| **Q29RY7** | Fibroleukin | 26.5 | 50.7 | 7.5 | −0.63 | **Q58CQ9** | Pantetheinase | 13.30 | 56.9 | 5.3 | −0.12 |
| **P01035** | Cystatin-C | 17.7 | 16.3 | 9.2 | 0.01 | **Q3Y5Z3** | Adiponectin | 11.82 | 26.1 | 5.4 | −0.47 |
| **P04815** | Spleen trypsin inhibitor I | 15.3 | 10.8 | 9.0 | −0.13 | **Q3SWX5** | Cadherin-6 | 7.96 | 88.3 | 4.8 | −0.49 |
| **F1MD83** | C-X-C motif chemokine | 14.6 | 12.6 | 9.3 | 0.06 | **P80012** | von Willebrand factor (Fragment) | 6.46 | 102.6 | 5.3 | −0.18 |
| **P02459** | Collagen alpha-1(II) chain | 11.7 | 141.8 | 6.8 | −0.81 | **Q3SYW7** | SPARC like 1 | 5.02 | 74.9 | 4.5 | −1.12 |
| **Q8SPP7** | Peptidoglycan recognition protein 1 | 11.2 | 21.1 | 9.6 | −0.26 | **G5E5T5** | Uncharacterized protein | 4.76 | 42.5 | 4.9 | −0.02 |
| **Q9N2I2** | Plasma serine protease inhibitor | 7.3 | 45.3 | 9.4 | −0.11 | **P31836** | Neural cell adhesion molecule 1 | 4.61 | 93.9 | 4.9 | −0.39 |
| **P17690** | Beta-2-glycoprotein 1 | 5.3 | 38.3 | 8.5 | −0.27 | **A5PKC2** | SHBG protein | 4.10 | 43.3 | 5.7 | −0.05 |
| **F1N4M7** | Complement factor I | 5.3 | 68.9 | 8.1 | −0.47 | **Q0VCG9** | Pentraxin-related protein PTX3 | 3.91 | 42.0 | 5.1 | −0.18 |
| **Q05716** | Insulin-like growth factor-binding protein 4 | 5.1 | 27.9 | 7.1 | −0.48 | **F1MPE1** | CD109 molecule | 3.89 | 161.7 | 5.4 | −0.08 |
| **P82943** | Regakine-1 | 5.0 | 10.3 | 8.8 | −0.10 | **Q9BGI3** | Peroxiredoxin-2 | 3.87 | 21.9 | 5.4 | −0.11 |
| **P80425** | Fatty acid-binding protein. liver | 4.8 | 14.2 | 7.8 | −0.40 | **P01044** | Kininogen-1 | 3.26 | 68.9 | 6.1 | −0.61 |
| **D1Z308** | Periostin | 4.5 | 93.2 | 7.0 | −0.20 | | | | | | |
| **P02453** | Collagen alpha-1(I) chain | 4.5 | 138.9 | 5.6 | −0.80 | | | | | | |
| **Q2KIS7** | Tetranectin | 4.1 | 22.1 | 5.5 | −0.24 | | | | | | |
| **P98140** | Coagulation factor XII | 4.0 | 67.2 | 7.9 | −0.38 | | | | | | |
| **E1BMJ0** | Factor XIIa inhibitor precursor | 4.0 | 51.7 | 6.2 | −0.06 | | | | | | |
| **Q5NTB3** | Coagulation factor XI | 3.9 | 69.9 | 7.8 | −0.27 | | | | | | |
| **F1N0K0** | Collagen alpha-1(XI) chain | 3.9 | 182.4 | 5.6 | −0.85 | | | | | | |
| **P13384** | Insulin-like growth factor-binding protein 2 | 3.7 | 34.0 | 7.1 | −0.52 | | | | | | |
| **Q2KJ63** | Plasma kallikrein | 3.6 | 71.0 | 8.6 | −0.29 | | | | | | |
| **E1BLA8** | Golgi membrane protein 1 | 3.6 | 45.5 | 4.8 | −1.09 | | | | | | |
| **P02465** | Collagen alpha-2(I) chain | 3.6 | 129.1 | 9.2 | −0.67 | | | | | | |
| **Q17QC8** | Complement factor properdin | 3.5 | 50.8 | 8.3 | −0.42 | | | | | | |
| **F1MYX5** | Lymphocyte cytosolic protein 1 | 3.3 | 70.1 | 5.2 | −0.31 | | | | | | |
| **Q28065** | C4b-binding protein alpha chain | 3.3 | 68.9 | 6.0 | −0.38 | | | | | | |

water, structure and surface chemistry of the 2 nm H/O-DNDs employed have been described previously [9,10], this study aimed to complement these characteristics with the determination of the zeta potential (ZP) of H/O-DNDs in various biological solutions and their effect on aggregation of DNDs. The ZP was measured in DMEM medium (cell cultivation solution) and DMEM medium supplemented with 5% of FBS (protein-containing cell cultivation medium) as well as in water as standard; the results are summarized in Table 1. The O-DNDs were found to display an overall negative charge in all the tested solutions - highly negative in water (−62 mV) as well as in the cultivation medium (−37 mV) even in the presence of proteins (−34 mV); in all cases significantly in excess of the stable colloidal solution value. The high ZPs were reflected in preservation of good dispersion ability in DMEM as well as DMEM with 5% of FBS. In contrast, the ZP of H-DNDs was highly positive in water (+62 mV) which is in agreement with a previous report [41] but dropped to a level associated with poor colloidal stability in the cultivation medium (+5 mV) accompanied by aggregation resulting in increased size of H-DNDs (Supplementary Table 1). The drop of ZP of positively charged NPs prepared from different materials is already a well-documented effect induced by proteins from serum/plasma [42,43]. The reduction in the ZP in the DMEM solution compared to pure water revealed the important effect of ions and non-protein molecules on the properties of DNDs (the medium contained amino acids, vitamins, inorganic salts and sugars), i.e. the formation of a biomolecular corona [44]. However, since we were primarily concerned with DND-associated FBS-containing proteins, these biomolecules were deemed outside the focus of the study. In addition to the non-protein molecules, the clear influence of FBS proteins on the ZP of H-DNDs was also detected; the ZP changed to −19 mV (in the FBS-supplemented medium), i.e. its value remained around the same (in the range of potentially poor colloidal stability) but the charge became negative. A similar change in the ZP from initially positive to negative following the formation of protein corona in the presence of FBS was also observed on Si-NP by Kurtz-Chalot et al. [45]. Thus, the formation of protein-DND aggregates can be expected in a similar way to that described previously [30]. The size of O-/H-DND aggregates in various media was measured immediately after the pellet was re-dispersed in water. Since the samples were re-dispersed in water from pellets, soft sonication of 1 min was applied and the sample were re-measured, for comparison both values are shown in Supplementary Table 1. Unlike reported agglomeration of 10–100 nm oxidized high pressure high temperature nanodiamonds in DMEM solution [18], the 2 nm oxidized DNDs show good colloidal stability in DMEM. Besides ions, DMEM contains several amino acids which may, through electrostatic interaction, work as stabilizers for ultra-small NDs but are inefficient for larger (more than 10 nm) ones.

### 3.2. Proteomic results

The protein corona on the H/O-DND samples was analysed via qualitative and quantitative LC-MS/MS. The qualitative analysis (data-dependent analysis - DDA) identified the number of proteins on each of the H/O-DNDs, which was found to be comparable − 164 ± 7.6 identified proteins on the H-DNDs and 173 ± 6.5 identified proteins on the O-DNDs. The number of identified proteins is in good agreement with previously published studies which revealed that the protein corona typically consists of hundreds of proteins

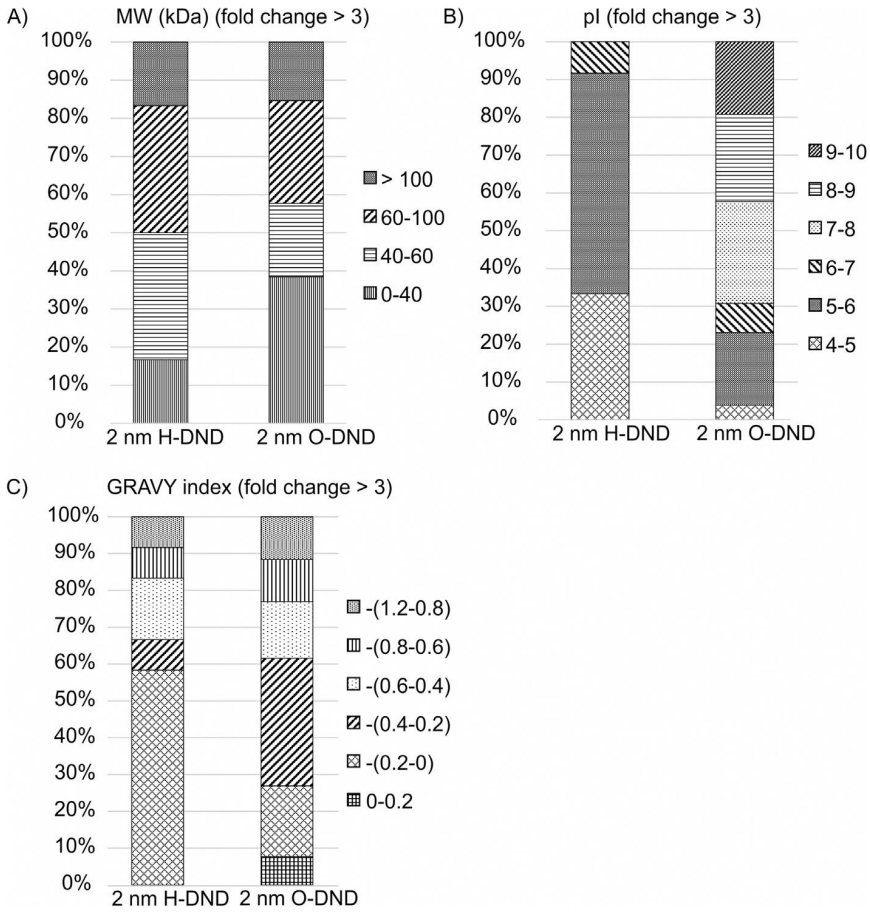


**Fig. 2.** Classification of proteins (with fold change > 3) significantly enriched on 2 nm H-DNDs and 2 nm O-DNDs. A) Proteins classified according to their molecular weight, B) theoretical pI and C) theoretical GRAVY index. The analysed proteins originate from FBS. (A colour version of this figure can be viewed online.)

[46–48]. However, most of the previously mentioned studies consulted characterized protein corona on much larger NPs. The list of identified proteins detected on the O-DNDs overlapped to a certain extent with that on the H-DNDs; thus, the simple qualitative listing of the proteins was unable to clearly capture the differences in the binding properties of H- and O-DNDs. Therefore, we performed a quantitative analysis in the form of SWATH, via which a library of 242 proteins was created based on the qualitative LC-MS/MS data (see Experimental); moreover, the data was processed in order to obtain statistical indicators of the binding characteristics of each of the protein in the library. The quantity of the proteins in the library was calculated as the sum of protein-specific peptides and fragments. The protein intensity was then compared via the Student T-test between 2 nm O-DNDs and 2 nm H-DNDs (the statistical significance threshold was set at $P < 0.05$). As can be seen in Fig. 1, the proteins in the library clustered so as to form three categories – i) proteins that bound similarly to both types of DNDs (66 proteins, e.g. fibronectin, Hsp70, tubulin, etc.), ii) proteins that bound preferentially to the H-DNDs (90 proteins, e.g. pantetheinase, adiponectin, etc.) and iii) proteins that bound preferentially to the O-DNDs (86 proteins, e.g. fibroleukin, cystatin C, etc.). A complete list of the quantitative data can be found in Supplementary Table 2. In order to allow for a description of the substantial differences between protein adsorption onto 2 nm H- and O-DNDs we focused further analysis on those proteins that were significantly different (Table 2) as a result of the T-test (statistical significance), and their protein abundance ratio was greater than 3. The later characteristic means relative quantitative value expressing the difference in abundance of proteins between 2 nm H-DND and 2 nm O-DND. We will use the term "fold change" for the designation of such characteristics throughout the rest of the text. The number of proteins enriched on the O-DNDs was found to be more than two-fold (26 proteins) the number enriched on the H-DNDs (12 proteins).

With respect to the seemingly contradictory results published previously – on the one hand suggesting that negatively charged NPs should attract primarily positively charged proteins and *vice versa* [49–51], while, on the other hand, indicating that the protein corona of NPs are composed predominantly of negatively charged proteins [46] – we compared the proteins detected on positively and negatively charged DNDs using selected parameters such as the theoretical molecular weight (MW), the isoelectric point (pI) and the GRAVY [52] index (Fig. 2).

A broad molecular weight distribution of proteins with fold changes of >3 in the range 10–200 kDa was determined for both types of DNDs; 80% of the proteins were <100 kDa on the O-DNDs and 90% on the H-DNDs (Table 2 and Fig. 2A). Due to a lack of similar studies on ultra-small NPs, we can only speculate as to the significance of this outcome; nevertheless, the differences were noticeable. Analogical studies employing mass spectrometry but using much larger particles and human plasma also determined a high percentage (80%) of proteins of <100 kDa (iron oxide particles

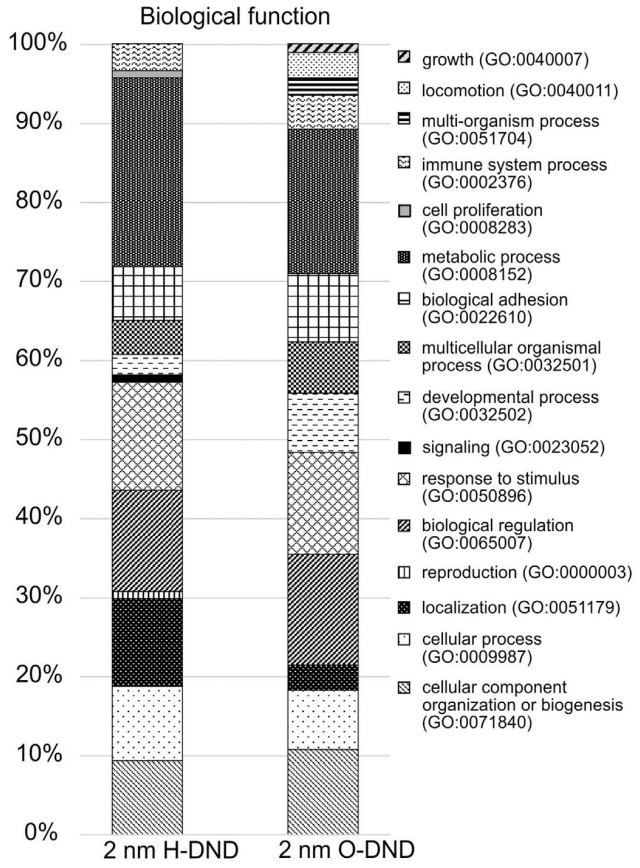


**Fig. 3. Bioinformatics classification of SWATH-MS quantified proteins (with fold change > 3) on 2 nm H-DNDs or 2 nm O-DNDs.** Proteins were classified by Panther classification system [39] according to their biological function. The analysed proteins originate form FBS.

[53], liposome particles [47], polystyrene NPs [46]).

The subsequent bioinformatics analysis compared the theoretical pI values of the proteins identified on the H-/O-DNDs (fold change > 3, Fig. 2B). The analysis detected proteins with a pI of <7 (proteins with a negative charge at a physiological pH, e.g. pantetheinase) among the most abundant proteins on the H-DNDs that initially exhibited a highly positive ZP. Conversely, 70% of the proteins with a pI of >7 (proteins with a positive charge at a physiological pH) were detected on the O-DNDs that have a highly negative ZP. Several of the most abundant proteins on the O-DNDs even exhibited a highly positive charge with a pI of >9. Thus, it can be concluded that FBS proteins bind predominantly to ultra-small DNDs due to electrostatic interaction originating from specific surface chemistry/zeta potential of the studied DNDs as also indicated by a number of previous studies [49–51]. Yet, a very broad study conducted by Tenzer et al. reported joint influence of the NPs physicochemical properties such as NP composition, surface chemistry/zeta potential and size on the binding preferences of differently charged proteins [46]. However, the study considered much larger NPs (30–140 nm) than the ultra-small 2 nm DNDs in our study.

Interestingly, the overall hydrophilic or hydrophobic character of the proteins detected on the two types of DNDs (with fold change > 3) was similar for both surfaces. The mean GRAVY values were −0.32 and −0.39 for the H-DNDs and O-DNDs, respectively. Only two proteins (cystatin-C and C-X-C motif chemokine) bound to the O-DNDs evinced a hydrophobic character as given by their positive GRAVY index value. No such proteins were found among the most abundant proteins on the H-DNDs (Fig. 2C). These two proteins also exhibited very high pI (they had strong positive charges) which predestined them to be close to the negative surface of the O-DNDs. They were also relatively small (16.3 and 12.6 kDa respectively), which accorded them priority in terms of binding to the surface among other (larger) proteins. Still, one must bear in mind that the MW, pI and GRAVY values are theoretical as computed from the amino acid sequences of the identified proteins employing Uniprot data. They do not take into consideration, for example, processing via post-translational cleavage or modifications. The interaction of proteins and NPs may also be facilitated merely by the specific amino acid sequence of a protein with suitable local characteristics [54]. Nevertheless, based on an experimental study by Ukraintsev et al. on diamond thin film surfaces, it is reasonable to expect that these hydrophobic proteins are indeed positioned in the proximal layer on particles shielded by hydrophilic proteins in the distal layer [55]. Thus, the electrostatic interaction and nanodiamond surface chemistry rather than the hydrophobic or hydrophilic character are responsible for the assembly of proteins on ultra-small DNDs.

In order to investigate a possible NP size dependence on the composition of the protein coronas, we also analysed 4 nm H-/O-DND analogues. We discovered that most of the proteins enriched on 2 nm H-/O-DNDs (fold change > 3 difference) were also quantified as significantly enriched on the larger 4 nm DNDs. 10 identical proteins were found on H-DNDs of both sizes and 2 unique proteins on each size, whereas 21 identical proteins were found on O-DNDs of both sizes and 5 unique proteins on each size (Table 2 and Supplementary Table 3.). This indicates that with respect to the interaction of proteins with DNDs in the 1–5 nm region, the surface termination is more important than the difference in their size. This finding is supported by other studies that revealed that the surface properties of various polystyrene NPs were more relevant in terms of protein adsorption than was particle size [49,56]. Despite these studies considering polystyrene NPs in the range 50 nm–400 nm, we observed that the same tendency is also valid for one to two orders of magnitude smaller DNDs that are also smaller than most of the FBS proteins.

Since the proteins that were significantly quantified on the tested DNDs represented a very broad spectrum of proteins with differing physicochemical properties (Table 2.), the whole spectrum was analysed via the Panther [39] classification system in order to classify the proteins according to their biological function (in the context of cell- or organism-level processes). As shown in Fig. 3, the biological function of the proteins from the protein corona of H-DNDs and O-DNDs covers many different cell processes including biological adhesion, localization, growth, etc., which were represented evenly for both the O-DND and H-DND samples. However, different proteins were linked on the O-DNDs and H-DNDs within the same biological group. For example, a group of proteins with the “adhesion” function containing proteins specific to cell-cell interaction (e.g. vascular cell adhesion molecule 1 (VCAM1), contactin-1, cadherin-6, procadherin gamma-C3, procadherin 12) was found on the H-DNDs, whereas proteins specific to cell-extracellular matrix interaction (e.g. collagen type V, periostin, fibrinogen gamma-B chain, transforming growth factor-beta-induced protein ig-h3) were detected on the O-DNDs. Currently, we can only speculate as to whether this difference plays an important role in the interaction of DNDs covered by these specific proteins with the cells.

In addition, a number of proteins of interest with respect to cell interaction were detected on both types of DNDs (non-significant group – grey squares in Fig. 1, Supplementary Table 2). For example,

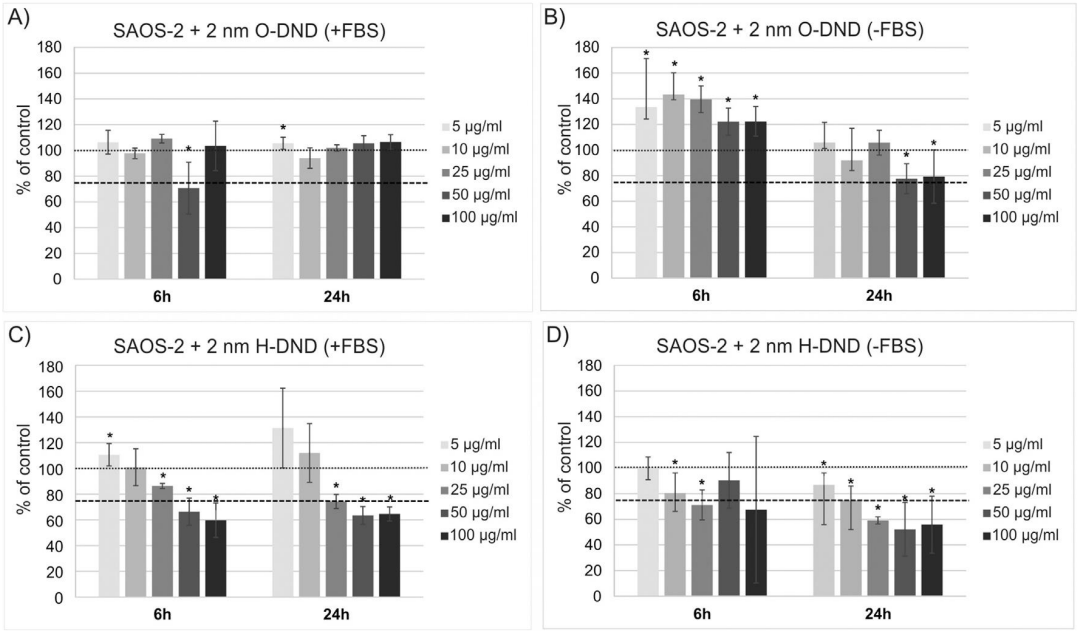


**Fig. 4. Metabolic activity of SAOS-2, incubated with 2 nm H-DND and 2 nm O-DND under standard (with FBS – A, C) and non-standard conditions (without FBS–B, D).** Relative values are expressed as a percentage of control sample (untreated cells in adequate cultivation medium). The star symbol (*) highlights a significant difference from the control in cultivation medium with 5% FBS (Wilcoxon matched-pairs test, $p < 0.05$). Dotted line shows 100% of control, the dashed line shows 75% of control (toxic level), error bars represent standard deviations.

vitronectin is a major protein that is responsible for cell adhesion; this protein constitutes a natural component of blood plasma (serum) and was identified on both the DND types considered in our study. A comprehensive study of differently terminated particles (with sizes of between 100 nm and 200 nm) by Palchetti et al. determined this protein to be an important promoter of NP association with HeLa cells [57] due to its featuring a specific receptor on the cellular membrane. The non-significant group of

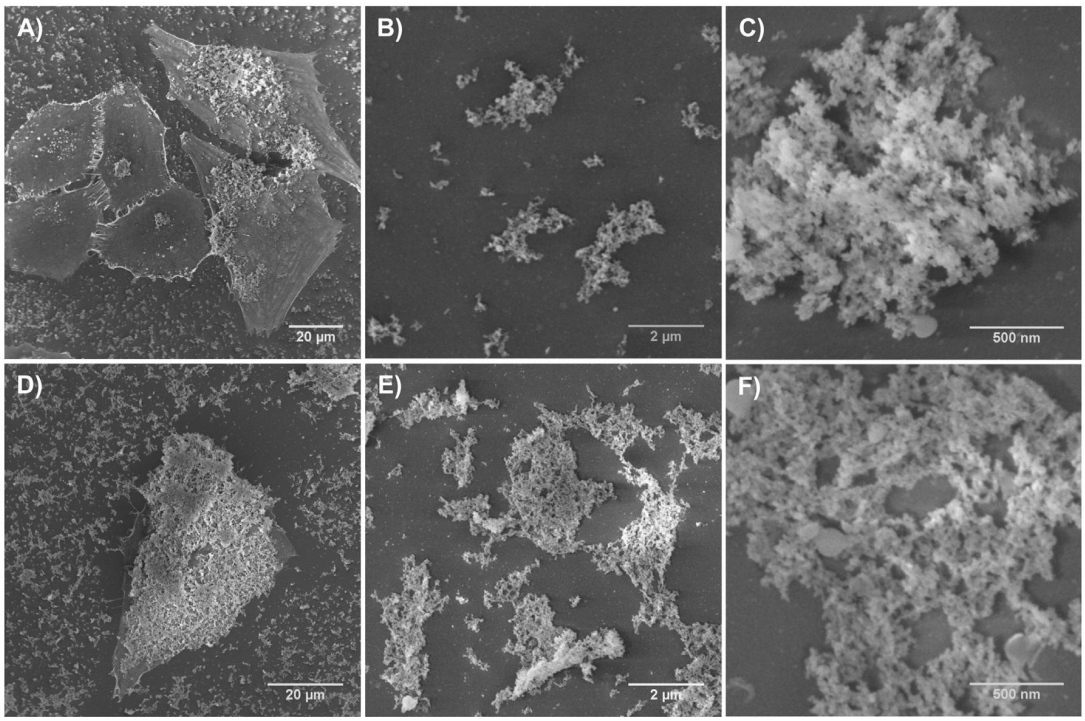


**Fig. 5. SEM images of 2 nm O-DNDs and 2 nm H DNDs after 24 h incubation with cells.** Cells incubated with particles in the medium with 5% FBS (A – O-DND, D – H-DND), nanoparticle-protein network located around the cells on the cultivation surface (B, C – O-DNDs; E, F – H-DNDs).

proteins also includes highly-abundant serum proteins such as alpha-1-antiproteinase, plasminogen and others that are found universally in FBS [58]. The most abundant serum protein – serum albumin – was determined in our study with an increased fold change on the H-DNDs (1.1 fold in comparison to the O-DNDs); however, as pointed out in other studies, the distribution of albumin as a major component in serum in the protein corona of differing NPs is variable [12,54,59]. Our study focused primarily on proteins that were considered specific to the hydrogenated and oxidized surfaces of ultra-small DNDs and that might be critical in terms of the *in vivo* response.

From the biomedical point of view (e.g. intravenous application), the physicochemical properties of DNDs are crucial in terms of their spontaneous interaction in body fluids, where they are able to form complexes with proteins and other biomolecules. These complexes are able to interact with human cells in a distinct way as compared to single or bare DNDs. The conformation of the proteins attached to the DND may be altered [60–62] or their functional motifs might be buried inside [63]. Moreover, DNDs are capable of inducing protein clustering and the creation of the multivalent effect, i.e. the multiple ligands bound to the NP are able to react with multiple receptors on the cell surface, which is beneficial in terms of enhanced biological recognition or improved binding [57,64]. For example, serum proteins such as fibrinogen, immunoglobulins and complement proteins are able to act as opsonins and thus promote the phagocytosis of NPs. Conversely, dysopsonins such as albumin or apolipoproteins inhibit phagocytic ingestion and thus prolong the half-life of NPs in blood [65]. Our analysis revealed that opsonins such as complement factors were significantly enriched on the O-DNDs (Table 2) and, moreover, several apolipoproteins were detected on both the H-DNDs and O-DNDs (Supplementary Table 2).

### 3.3. Nanodiamonds-cell interaction

All the above serves to document the diversity of proteins with distinct functions in complexes with NPs and indicates that their final biological properties are the result of complex contributions. Proteins with a wide variety of biological functions are attracted by both hydrogenated and oxidized DNDs and they may exert very distinct and, to date, unknown impacts on cells or, indeed, the whole organism. However, our data also demonstrated the huge potential in terms of the binding capability of specifically-targeted proteins to the various surfaces of DNDs. Thus, we evaluated the effect of H/O-DNDs on human cells. The potential cytotoxic effect of 2 nm H/O-DNDs on human osteoblasts (SAOS-2 cell line) was analysed via the monitoring of the metabolic activity that reflects the viability of cells (Fig. 4) treated with various DND concentrations over differing time intervals and under differing conditions (with and without the addition of FBS).

The presence of FBS in the medium enabled the spontaneous association of proteins with DNDs and the formation of protein corona thus leading to an immediate change in the properties of the DNDs (as can be seen from the ZP change in Table 1). The O-DNDs cultivated with cells in the presence of proteins (+FBS) appear to have exerted a non-toxic effect at the time points investigated (Fig. 4A). The interaction of FBS proteins with the O-DNDs most probably increased their hydrodynamic diameter or induced the formation of clusters (Supplementary Table 1); however, the ZP remained negative in the colloidal stability region (Table 1). Therefore, their increased size, together with the negative surface charge, may prevent them from entering the negatively charged cells and from inducing the effects detectable using this method. These results correspond well with observations concerning other DND samples with larger diameters (5 nm) and differing termination [30].

However, in the absence of FBS, the same O-DNDs induced an elevation in the metabolic activity of the cells at all the tested concentrations after 6 h (Fig. 4B). This temporary elevation returned to the control level after a longer incubation period (24 h) and only the highest concentration of O-DNDs induced osteoblast cytotoxicity (Fig. 4B). The O-DNDs without the presence of attached proteins remained in the colloid in the form of single particles and, thus, despite their negative charge, they were able to freely enter cells via direct transport through the membrane as demonstrated by other research groups [66–68]. The initial increase in metabolic activity in the FBS-free medium might be explained via the interaction of these bare DNDs with certain cellular pathways and the transient sensitization of the cells (e.g. the enhanced activity of cellular dehydrogenases) [69]. Subsequently, the internalized particles at the higher concentration impaired certain pathways or, alternatively, the normal functioning of the organelles, thus leading to cell death (Figs. 4B–50 and 100 μg/ml O-DNDs (-FBS)).

In contrast, the 2 nm H-DNDs induced concentration-dependent cytotoxicity in the presence of FBS. Thus, their mode of action is clearly different from that of O-DNDs (Fig. 4C). H-DNDs in contact with proteins from the FBS demonstrated a reverse in their ZP from +62 mV to −19 mV, thus indicating the formation of protein-H-DND aggregates in a more pronounced manner than in the case of the O-DNDs as also demonstrated by the DLS data analysis (Supplementary Table 1), which exhibited a ZP of −34 mV under the same conditions. Since the protein-H-DND aggregates became negatively charged they were unable to enter the negatively charged cells in the same manner as O-DNDs did. Moreover, these aggregates were observed to cause the cells to be mechanically stressed. Therefore, the metabolic activity of the cells is suppressed for a different reason than that concerning the bare, cell-penetrating O-DNDs. It is known that mechanical stress caused by the coverage of the cell surface with large NP aggregates (10–400 nm) destroys the cell cytoskeleton thus resulting in cell death via apoptosis [70,71].

The initial absence of FBS increased the cytotoxic effect of the 2 nm H-DNDs on the SAOS-2 cells (Fig. 4D) even at lower concentrations. In this case the H-DNDs remained positively charged in the cultivation medium without proteins even though the ZP value was lowered, thus potentially rendering the colloidal dispersion less stable (ZP + 5 mV, Table 1). Thus, the bare H-DNDs were able to easily bind to the cell membrane and most probably to enter the cells where they interfered with the various cellular processes and, thereby, induced a cytotoxic effect. This internal cytotoxic effect persisted and continued at least up to the 24 h-time point even though FBS was added after the first 6 h (essential in terms of the long-term survival of the cells – see Experimental). Remaining H-DNDs in the solution formed complexes with the proteins as in the case of the H-DNDs added directly to the FBS-supplemented medium. Thus, they may have exerted an additional cytotoxic effect on the cells due to mechanical stress. These findings are in contrast to those of Kurtz-Chalot et al. who concluded that a higher uptake of Si-NP is less cytotoxic than their adsorption on the cell membrane surface [45]. Various factors contributed to the differing conclusions. It is possible that the internal cytotoxic effect was screened by too high Si-NP concentration, the intake of Si-NPs was less than that of ultra-small DNDs, or the Si-NPs were rapidly biodegraded (dissolved) inside the cell.

With respect to the ZP data, which indicated the formation of protein-DND aggregates (especially in the case of the H-DNDs in the cultivation medium with FBS), SEM images of the cells and their surroundings were recorded following the administration of DNDs. Fig. 5 illustrates protein-DND aggregates that formed following the incubation of hydrogenated and oxidized DNDs with SAOS-2 for

24 h under standard conditions. A notable difference is evident in terms of the size of the aggregates (Fig. 5B versus Fig. 5E); their size is in agreement with the ZP measurements. The higher negative value of the O-DND ZP (−34 mV) resulted in the formation of smaller complexes than in the case of the H-DNDs (−19 mV). The closer the ZP approached zero, the lower was the colloidal stability and thus the higher was the potential for NP aggregation [72,73]. Hence, the ZP of the protein-DND controls aggregation rather than the interaction of the protein corona since the outer part of the protein corona features similar, hydrophilic proteins with respect to both the O-DNDs and H-DNDs.

The SEM images also clearly illustrate that the O-DNDs covered the cell surface only partially, whereas the H-DNDs covered almost the entire cell surface, which may have been the reason for the detected decrease in the cell metabolic activity to cytotoxic levels (Fig. 4C). The protein-DND complexes on the cell surface may have negatively influenced cell fitness including the intake of nutrients or, alternatively, they may have hampered the natural movements of the cell membrane (mechanical stress). Moreover, the physico-chemical interaction of the NPs with the membrane may have exerted an effect on its integrity. Different membrane models (e.g. giant uni-lamellar vesicles) have demonstrated that NPs may exert an impact on membrane integrity as a result of their ability to change their phase (gelation) thus triggering a cytotoxic effect due to the cells requiring a separated intracellular environment and a fluid membrane phase so as to regulate molecular transport [74]. More negatively charged O-DNDs evince a lower degree of attraction to the negatively-charged cell membrane and are thus less harmful in terms of membrane integrity than are positively-charged H-DNDs.

The surface chemistry of ultra-small DNDs thus exerts an obvious effect on the formation and composition of the protein corona as well as on the viability of cells via diverse interaction mechanisms (the entry of single ultra-small NPs versus the adsorption of protein-NP complexes on the plasma membrane). Despite the challenging nature of linking theoretical bioinformatics data based on mass spectrometry with the behaviour of NPs via *in vitro* cellular experiments, we demonstrated that such an interconnection is possible.

## 4. Conclusion

The study presented an initial insight into the behaviour of hydrogenated and oxidized ultra-small ~2 nm DNDs in various biological media and their interactions with proteins and human cells. The detailed study of the proteins associated with these ultra-small DNDs by means of LC-MS/MS and a subsequent qualitative and quantitative analysis demonstrated that the bound proteins completely altered the characteristics of the DNDs.

We determined that both the surface chemistry and the charge are crucial in terms of attracting proteins from the serum protein pool. We further demonstrated that proteins significantly associated with one type of DND surface chemistry differ with concern to their theoretical parameters such as pI etc. The proteins that were presented principally on the positively-charged H-DNDs displayed a predominantly negative charge at physiological pH (mean pI ~ 5.2) while those proteins that were presented primarily on the negatively-charged O-DNDs displayed a predominantly positive charge (pI 7–10) under the same conditions. Therefore, it can be stated that the nanodiamond surface chemistry and electrostatic interaction due to the zeta potential of the DNDs were responsible for selective protein attraction rather than the hydrophobic or hydrophilic character of the nanodiamonds and proteins. Moreover, the surface chemistry was determined to be more important than the difference in the size of the DNDs in the sub-5 nm region. The ZP of the H-DNDs was significantly altered in the cell media and even assumed the opposite charge as a result of interaction with the FBS proteins. In addition, the ZP controlled the aggregation of protein-DND complexes into smaller or larger structures as well as interaction with the cells. The ultra-small O-DNDs exerted a predominantly neutral or even positive effect on cell viability while, conversely, the ultra-small H-DNDs exhibited noticeable cytotoxic effects as a result of two different mechanisms, i.e. i) possible entry of single NPs and the disruption of metabolic processes in the case of bare NPs or ii) mechanical stress originating from the dense coverage of the cells by protein-DND aggregates.

Ultra-small DNDs provide a promising nanomaterial for use in the fields of biomedicine and biology in general thanks principally to their virtually molecular size and the potential to adjust their surface chemistry to the molecular scale and thus to target specific proteins. The research presented herein demonstrated that the surface chemistry of such ultra-small DNDs makes up an essential parameter in terms of their interaction with proteins as well with concern to their cytotoxicity. While a number of trends identified with respect to larger NPs were also found to apply to DNDs of 2 nm (size smaller than most of the proteins in the FBS) other findings differed to those determined in previous studies, e.g. the uptake of H-DNDs into cells is more cytotoxic than their adsorption on the cell membrane (mechanical stress). In spite of the high degree of complexity of nanoparticle-medium-cell interactions, the study revealed some of the key properties and mechanisms that govern the interaction of ultra-small nanodiamonds with proteins and cells. Thus, it is hoped that the research described herein will contribute to improving the understanding of the range of biomedical experiments previously performed employing nanodiamonds as well as ultra-small nanoparticles from other materials.

## Declaration of competing interest

The authors declare no competing interest.

## CRediT authorship contribution statement

**Iva Machova:** Investigation, Writing - original draft. **Martin Hubalek:** Conceptualization, Methodology, Formal analysis, Writing - original draft, Writing - review & editing, Supervision. **Tereza Belinova:** Investigation, Writing - original draft. **Anna Fucikova:** Investigation, Writing - review & editing. **Stepan Stehlik:** Investigation, Writing - review & editing, Funding acquisition. **Bohuslav Rezek:** Writing - review & editing, Funding acquisition. **Marie Hubalek Kalbacova:** Conceptualization, Writing - original draft, Writing - review & editing, Supervision, Funding acquisition, Project administration.

## Acknowledgements

The authors declare no competing financial interests. This work was supported by the project of National Sustainability Program I No. LO1503 provided by Ministry of Education, Youth and Sports of the Czech Republic and by PROGRES Q26 and SVV 260390 provided by Charles University. This work was also supported by the OPVVV project from ERDF/MSMT CZ.02.1.01/0.0/0.0/16_019/0000760 (Solid 21), LNSM research infrastructure (LM2015087), the Czech Science Foundation (GACR) grant number 18-11711Y (S. Stehlik), and UNCE/SCI/010 (A. Fucikova). Computational resources were provided by the ELIXIR-CZ project (LM2015047), part of the international ELIXIR infrastructure. The authors kindly acknowledge P. Bauerova (Inst. of Physics CAS) for the SEM measurements.

## Appendix A. Supplementary data

Supplementary data to this article can be found online at https://doi.org/10.1016/j.carbon.2020.02.061.

## References


[1] M. Lundqvist, C. Augustsson, M. Lilja, K. Lundkvist, B. Dahlbäck, S. Linse, T. Cedervall, The nanoparticle protein corona formed in human blood or human blood fractions, PloS One 12 (2017) 1–15, https://doi.org/10.1371/journal.pone.0175871.

[2] V.N. Mochalin, O. Shenderova, D. Ho, Y. Gogotsi, The properties and applications of nanodiamonds, Nat. Nanotechnol. 7 (2012) 11–23, https://doi.org/10.1038/nnano.2011.209.

[3] M. Chipaux, K.J. van der Laan, S.R. Hemelaar, M. Hasani, T. Zheng, R. Schirhagl, Nanodiamonds and their applications in cells, Small 14 (2018) 1–25, https://doi.org/10.1002/smll.201704263.

[4] K. van der Laan, M. Hasani, T. Zheng, R. Schirhagl, Nanodiamonds for in vivo applications, Small 14 (2018) 1–17, https://doi.org/10.1002/smll.201703838.

[5] M. Kurzyp, H.A. Girard, Y. Cheref, E. Brun, C. Sicard-Roselli, S. Saada, J.-C. Arnault, Hydroxyl radical production induced by plasma hydrogenated nanodiamonds under X-ray irradiation, Chem. Commun. 53 (2017) 1237–1240, https://doi.org/10.1039/C6CC08895C.

[6] A.M. Schrand, S.A.C. Hens, O.A. Shenderova, Nanodiamond particles: properties and perspectives for bioapplications, Crit. Rev. Solid State Mater. Sci. 34 (2009) 18–74, https://doi.org/10.1080/10408430902831987.

[7] A.M. Schrand, H. Huang, C. Carlson, J.J. Schlager, E. Ōsawa, S.M. Hussain, L. Dai, Are diamond nanoparticles cytotoxic? J. Phys. Chem. B 111 (2007) 2–7, https://doi.org/10.1021/jp066387v.

[8] S. Stehlik, M. Varga, M. Ledinsky, V. Jirasek, A. Artemenko, H. Kozak, L. Ondic, V. Skakalova, G. Argentero, T. Pennycook, J.C. Meyer, A. Fejfar, A. Kromka, B. Rezek, Size and purity control of HPHT nanodiamonds down to 1 nm, J. Phys. Chem. C 119 (2015) 27708–27720, https://doi.org/10.1021/acs.jpcc.5b05259.

[9] S. Stehlik, M. Varga, M. Ledinsky, D. Miliaieva, H. Kozak, V. Skakalova, C. Mangler, T.J. Pennycook, J.C. Meyer, A. Kromka, B. Rezek, High-yield fabrication and properties of 1.4 nm nanodiamonds with narrow size distribution, Sci. Rep. 6 (2016) 38419, https://doi.org/10.1038/srep38419.

[10] S. Stehlik, M. Varga, P. Stenclova, L. Ondic, M. Ledinsky, J. Pangrac, O. Vanek, J. Lipov, A. Kromka, B. Rezek, Ultrathin nanocrystalline diamond films with silicon vacancy color centers via seeding by 2 nm detonation nanodiamonds, ACS Appl. Mater. Interfaces 9 (2017) 38842–38853, https://doi.org/10.1021/acsami.7b14436.

[11] I.I. Vlasov, A.A. Shiryaev, T. Rendler, S. Steinert, S.Y. Lee, D. Antonov, M. Vörös, F. Jelezko, A.V. Fisenko, L.F. Semjonova, J. Biskupek, U. Kaiser, O.I. Lebedev, I. Sildos, P.R. Hemmer, V.I. Konov, A. Gali, J. Wrachtrup, Molecular-sized fluorescent nanodiamonds, Nat. Nanotechnol. 9 (2014) 54–58, https://doi.org/10.1038/nnano.2013.255.

[12] J. Piella, N.G. Bastús, V. Puntes, Size-dependent protein–nanoparticle interactions in citrate-stabilized gold nanoparticles: the emergence of the protein corona, Bioconjugate Chem. 28 (2017) 88–97, https://doi.org/10.1021/acs.bioconjchem.6b00575.

[13] S. Tenzer, D. Docter, S. Rosfa, A. Wlodarski, J.J. Kuharev, A. Rekik, S.K. Knauer, C. Bantz, T. Nawroth, C. Bier, J. Sirirattanapan, W. Mann, L. Treuel, R. Zellner, Michael Maskos, H.H. Schild, R.H. Stauber, M. Maskos, Nanoparticle size is a critical physico- chemical determinant of the human blood plasma corona: a comprehensive quantitative proteomic analysis, ACS Nano 5 (2011) 7155–7167, https://doi.org/10.1021/nn201950e.

[14] A. Salvati, A.S. Pitek, M.P. Monopoli, K. Prapainop, F.B. Bombelli, D.R. Hristov, P.M. Kelly, C. Åberg, E. Mahon, K.A. Dawson, Transferrin-functionalized nanoparticles lose their targeting capabilities when a biomolecule corona adsorbs on the surface, Nat. Nanotechnol. 8 (2013) 137–143, https://doi.org/10.1038/nnano.2012.237.

[15] A. Lesniak, F. Fenaroli, M.P. Monopoli, C. Åberg, K.A. Dawson, A. Salvati, Effects of the presence or absence of a protein corona on silica nanoparticle uptake and impact on cells, ACS Nano 6 (2012) 5845–5857, https://doi.org/10.1021/nn300223w.

[16] D. Di Silvio, M. Maccarini, R. Parker, A. Mackie, G. Fragneto, F. Baldelli Bombelli, The effect of the protein corona on the interaction between nanoparticles and lipid bilayers, J. Colloid Interface Sci. 504 (2017) 741–750, https://doi.org/10.1016/j.jcis.2017.05.086.

[17] J. Simon, L.K. Müller, M. Kokkinopoulou, I. Lieberwirth, S. Morsbach, K. Landfester, V. Mailänder, Exploiting the biomolecular corona: pre-coating of nanoparticles enables controlled cellular interactions, Nanoscale 10 (2018) 10731–10739, https://doi.org/10.1039/C8NR03331E.

[18] E.R. Wilson, L.M. Parker, A. Orth, N. Nunn, M. Torelli, O. Shenderova, B.C. Gibson, P. Reineck, The effect of particle size on nanodiamond fluorescence and colloidal properties in biological media, Nanotechnology 30 (2019) 1–7, https://doi.org/10.1088/1361-6528/ab283d.

[19] C. Carrillo-carrion, M. Carril, J. Wolfgang, ScienceDirect Techniques for the experimental investigation of the protein corona, Curr. Opin. Biotechnol. 46 (2017) 106–113, https://doi.org/10.1016/j.copbio.2017.02.009.

[20] G. Miotto, M. Magro, M. Terzo, M. Zaccarin, L. Da Dalt, E. Bonaiuto, D. Baratella, G. Gabai, F. Vianello, Protein corona as a proteome fingerprint: the example of hidden biomarkers for cow mastitis, Colloids Surf. B Biointerfaces 140 (2016) 40–49, https://doi.org/10.1016/j.colsurfb.2015.11.043.

[21] L.C. Gillet, P. Navarro, S. Tate, H. Röst, N. Selevsek, L. Reiter, R. Bonner, R. Aebersold, Targeted data extraction of the MS/MS spectra generated by data-independent acquisition: a new concept for consistent and accurate proteome analysis, Mol. Cell. Proteomics 11 (2012), https://doi.org/10.1074/mcp.O111.016717. O111.016717.

[22] A.E. Garcia-Bennett, A. Everest-Dass, I. Moroni, I. Das Rastogi, L.M. Parker, N.H. Packer, L.J. Brown, Influence of surface chemistry on the formation of a protein corona on nanodiamonds, J. Mater. Chem. B. 7 (2019) 3383–3389, https://doi.org/10.1039/c9tb00445a.

[23] M. Lundqvist, J. Stigler, T. Cedervall, T. Berggård, M.B. Flanagan, I. Lynch, G. Elia, K. Dawson, The evolution of the protein corona around nanoparticles: a test study, ACS Nano 5 (2011) 7503–7509, https://doi.org/10.1021/nn202458g.

[24] S. Chatterjee, T.K. Mukherjee, Spectroscopic investigation of interaction between bovine serum albumin and amine-functionalized silicon quantum dots, Phys. Chem. Chem. Phys. 16 (2014) 8400–8408, https://doi.org/10.1039/c4cp00372a.

[25] D. Nierenberg, A.R. Khaled, O. Flores, Formation of a protein corona influences the biological identity of nanomaterials, Rep. Practical Oncol. Radiother. 23 (2018) 300–308, https://doi.org/10.1016/j.rpor.2018.05.005.

[26] Z.J. Deng, M. Liang, M. Monteiro, I. Toth, R.F. Minchin, Nanoparticle-induced unfolding of fibrinogen promotes Mac-1 receptor activation and inflammation, Nat. Nanotechnol. 6 (2011) 39–44, https://doi.org/10.1038/nnano.2010.250.

[27] A.E. Nel, L. Mädler, D. Velegol, T. Xia, E.M.V. Hoek, P. Somasundaran, F. Klaessig, V. Castranova, M. Thompson, Understanding biophysicochemical interactions at the nano–bio interface, Nat. Mater. 8 (2009) 543–557, https://doi.org/10.1038/nmat2442.

[28] D. Zhang, O. Neumann, H. Wang, V.M. Yuwono, A. Barhoumi, M. Perham, J.D. Hartgerink, P. Wittung-Stafshede, N.J. Halas, Gold nanoparticles can induce the formation of protein-based aggregates at physiological pH, Nano Lett. 9 (2009) 666–671, https://doi.org/10.1021/nl803054h.

[29] K. Bolaños, M.J. Kogan, E. Araya, Capping gold nanoparticles with albumin to improve their biomedical properties, Int. J. Nanomed. 14 (2019) 6387–6406, https://doi.org/10.2147/IJN.S210992.

[30] C. Bradac, I. Das Rastogi, N.M. Cordina, A. Garcia-Bennett, L.J. Brown, Influence of surface composition on the colloidal stability of ultra-small detonation nanodiamonds in biological media, Diam. Relat. Mater. 83 (2018) 38–45, https://doi.org/10.1016/j.diamond.2018.01.022.

[31] M. Kopp, S. Kollenda, M. Epple, Nanoparticle–protein interactions: therapeutic approaches and supramolecular chemistry, Acc. Chem. Res. 50 (2017) 1383–1390, https://doi.org/10.1021/acs.accounts.7b00051.

[32] G. Dravecz, T.Z. Jánosi, D. Beke, D. Major, G. Károlyházy, J. Erostyák, K. Kamarás, Á. Gali, Identification of the binding site between bovine serum albumin and ultrasmall SiC fluorescent biomarkers, Phys. Chem. Chem. Phys. 20 (2018) 13419–13429, https://doi.org/10.1039/c8cp02144a.

[33] M. Wang, O.J.R. Gustafsson, E.H. Pilkington, A. Kakinen, I. Javed, A. Faridi, T.P. Davis, P.C. Ke, Nanoparticle–proteome *in vitro* and *in vivo*, J. Mater. Chem. B. 6 (2018) 6026–6041, https://doi.org/10.1039/C8TB01634H.

[34] B. Pelaz, S. Jaber, D. de Aberasturi, V. Wulf, The state of nanoparticle-based nanoscience and biotechnology: progress, promises, and challenges, ACS Nano 6 (2012) 8468–8483, https://doi.org/10.1021/nn303929a.

[35] H.S. Choi, W. Liu, P. Misra, E. Tanaka, J.P. Zimmer, B. Itty Ipe, M.G. Bawendi, J.V. Frangioni, Renal clearance of nanoparticles, Nat. Biotechnol. 25 (2007) 1165–1170, https://doi.org/10.1038/nbt1340.Renal.

[36] A.K. Murthy, R.J. Stover, W.G. Hardin, R. Schramm, G.D. Nie, S. Gourisankar, T.M. Truskett, K.V. Sokolov, K.P. Johnston, Charged gold nanoparticles with essentially zero serum protein adsorption in undiluted fetal bovine serum, J. Am. Chem. Soc. 135 (2013) 7799–7802, https://doi.org/10.1021/ja400701c.

[37] K. Zarschler, L. Rocks, N. Licciardello, L. Boselli, E. Polo, K.P. Garcia, L. De Cola, H. Stephan, K.A. Dawson, Ultrasmall inorganic nanoparticles: state-of-the-art and perspectives for biomedical applications, Nanomed. Nanotechnol. Biol. Med. 12 (2016) 1663–1701, https://doi.org/10.1016/j.nano.2016.02.019.

[38] J. Erde, R.R.O. Loo, J.A. Loo, Enhanced FASP (eFASP) to increase proteome coverage and sample recovery for quantitative proteomic experiments 2014 loo. https://doi.org/10.1021/pr4010019, 2014.

[39] H. Mi, X. Huang, A. Muruganujan, H. Tang, C. Mills, D. Kang, P.D. Thomas, PANTHER version 11: expanded annotation data from Gene Ontology and Reactome pathways, and data analysis tool enhancements, Nucleic Acids Res. 45 (2017) D183–D189, https://doi.org/10.1093/nar/gkw1138.

[40] B. Bjellqvist, G.J. Hughes, C. Pasquali, N. Paquet, F. Ravier, J.-C. Sanchez, S. Frutiger, D. Hochstrasser, The focusing positions of polypeptides in immobilized pH gradients can be predicted from their amino acid sequences, Electrophoresis 14 (1993) 1023–1031, https://doi.org/10.1002/elps.11501401163.

[41] O.A. Williams, J. Hees, C. Dieker, W. Jäger, L. Kirste, C.E. Nebel, Size-dependent reactivity of diamond nanoparticles, ACS Nano 4 (2010) 4824–4830, https://doi.org/10.1021/nn100748k.

[42] N.V. Konduru, R.M. Molina, A. Swami, F. Damiani, G. Pyrgiotakis, P. Lin, P. Andreozzi, T.C. Donaghey, P. Demokritou, S. Krol, W. Kreyling, J.D. Brain, Protein corona: implications for nanoparticle interactions with pulmonary cells, Part. Fibre Toxicol 14 (2017) 1–12, https://doi.org/10.1186/s12989-017-

0223-3.
[43] A. Kurtz-Chalot, C. Villiers, J. Pourchez, D. Boudard, M. Martini, P.N. Marche, M. Cottier, V. Forest, Impact of silica nanoparticle surface chemistry on protein corona formation and consequential interactions with biological cells, Mater Sci. Eng. C-Materials Biol. Appl. 75 (2017) 16–24, https://doi.org/10.1016/j.msec.2017.02.028.
[44] R.M. Pearson, V.V. Juettner, S. Hong, Biomolecular corona on nanoparticles: a survey of recent literature and its implications in targeted drug delivery, Front. Chem. 2 (2014), https://doi.org/10.3389/fchem.2014.00108.
[45] A. Kurtz-Chalot, J.P. Klein, J. Pourchez, D. Boudard, V. Bin, G.B. Alcantara, M. Martini, M. Cottier, V. Forest, Adsorption at cell surface and cellular uptake of silica nanoparticles with different surface chemical functionalizations: impact on cytotoxicity, J. Nanoparticle Res. 16 (2014) 2738, https://doi.org/10.1007/s11051-014-2738-y.
[46] S. Tenzer, D. Docter, J. Kuharev, A. Musyanovych, V. Fetz, R. Hecht, F. Schlenk, D. Fischer, K. Kiouptsi, C. Reinhardt, K. Landfester, H. Schild, M. Maskos, S.K. Knauer, R.H. Stauber, Rapid formation of plasma protein corona critically affects nanoparticle pathophysiology, Nat. Nanotechnol. 8 (2013) 772–781, https://doi.org/10.1038/nnano.2013.181.
[47] D. Pozzi, G. Caracciolo, A.L. Capriotti, C. Cavaliere, G. La Barbera, T.J. Anchordoquy, A. Laganà, Surface chemistry and serum type both determine the nanoparticle–protein corona, J. Proteomics. 119 (2015) 209–217, https://doi.org/10.1016/j.jprot.2015.02.009.
[48] S.R. Hemelaar, A. Nagl, F. Bigot, M.M. Rodríguez-García, M.P. de Vries, M. Chipaux, R. Schirhagl, The interaction of fluorescent nanodiamond probes with cellular media, Microchim. Acta. 184 (2017) 1001–1009, https://doi.org/10.1007/s00604-017-2086-6.
[49] M.P. Monopoli, C. Åberg, A. Salvati, K.A. Dawson, Biomolecular coronas provide the biological identity of nanosized materials, Nat. Nanotechnol. 7 (2012) 779–786, https://doi.org/10.1038/nnano.2012.207.
[50] M.P. Monopoli, D. Walczyk, A. Campbell, G. Elia, I. Lynch, F. Baldelli Bombelli, K.A. Dawson, Physical-Chemical aspects of protein corona: relevance to in vitro and in vivo biological impacts of nanoparticles, J. Am. Chem. Soc. 133 (2011) 2525–2534, https://doi.org/10.1021/ja107583h.
[51] D. Walczyk, F.B. Bombelli, M.P. Monopoli, I. Lynch, K.A. Dawson, What the cell "sees" in bionanoscience, J. Am. Chem. Soc. 132 (2010) 5761–5768, https://doi.org/10.1021/ja910675v.
[52] J. Kyte, R.F. Doolittle, A simple method for displaying the hydropathic character of a protein, J. Mol. Biol. 157 (1982) 105–132, https://doi.org/10.1016/0022-2836(82)90515-0.
[53] V. Escamilla-Rivera, A. Solorio-Rodriguez, M. Uribe-Ramirez, O. Lozano, S. Lucas, A. Chagolla-López, R. Winkler, A. De Vizcaya-Ruiz, Plasma protein adsorption on $Fe_3O_4$-PEG nanoparticles activates the complement system and induces an inflammatory response, Int. J. Nanomed. 14 (2019) 2055–2067, https://doi.org/10.2147/IJN.S192214.
[54] V. Gorshkov, J.A. Bubis, E.M. Solovyeva, M.V. Gorshkov, F. Kjeldsen, Protein corona formed on silver nanoparticles in blood plasma is highly selective and resistant to physicochemical changes of the solution, Environ. Sci. Nano. 6 (2019) 1089–1098, https://doi.org/10.1039/C8EN01054D.
[55] E. Ukraintsev, B. Rezek, A. Kromka, A. Broz, M. Kalbacova, Long-term adsorption of fetal bovine serum on H/O-terminated diamond studied in situ by atomic force microscopy, Phys. Status Solidi Basic Res. 246 (2009) 2832–2835, https://doi.org/10.1002/pssb.200982257.
[56] H. Zhang, K.E. Burnum, M.L. Luna, B.O. Petritis, J.-S. Kim, W.-J. Qian, R.J. Moore, A. Heredia-Langner, B.-J.M. Webb-Robertson, B.D. Thrall, D.G. Camp, R.D. Smith, J.G. Pounds, T. Liu, Quantitative proteomics analysis of adsorbed plasma proteins classifies nanoparticles with different surface properties and size, Proteomics 11 (2011) 4569–4577, https://doi.org/10.1002/pmic.201100037.
[57] S. Palchetti, L. Digiacomo, D. Pozzi, G. Peruzzi, E. Micarelli, M. Mahmoudi, G. Caracciolo, Nanoparticles-cell association predicted by protein corona fingerprints, Nanoscale 8 (2016) 12755–12763, https://doi.org/10.1039/C6NR03898K.
[58] X. Zheng, H. Baker, W.S. Hancock, F. Fawaz, M. McCaman, E. Pungor, Proteomic analysis for the assessment of different lots of fetal bovine serum as a raw material for cell culture. Part IV. Application of proteomics to the manufacture of biological drugs, Biotechnol. Prog. 22 (2006) 1294–1300, https://doi.org/10.1021/bp060121o.
[59] K. Saha, M. Rahimi, M. Yazdani, S.T. Kim, D.F. Moyano, S. Hou, R. Das, R. Mout, F. Rezaee, M. Mahmoudi, V.M. Rotello, Regulation of macrophage recognition through the interplay of nanoparticle surface functionality and protein corona, ACS Nano 10 (2016) 4421–4430, https://doi.org/10.1021/acsnano.6b00053.
[60] M. Lundqvist, I. Sethson, B.-H. Jonsson, High-resolution 2D 1 H– 15 N NMR characterization of persistent structural alterations of proteins induced by interactions with silica nanoparticles, Langmuir 21 (2005) 5974–5979, https://doi.org/10.1021/la050569j.
[61] M. Lundqvist, I. Sethson, B.-H. Jonsson, Protein adsorption onto silica nanoparticles: conformational changes depend on the particles' curvature and the protein stability, Langmuir 20 (2004) 10639–10647, https://doi.org/10.1021/la0484725.
[62] V.H. Nguyen, B.-J. Lee, Protein corona: a new approach for nanomedicine design, Int. J. Nanomed. 12 (2017) 3137–3151, https://doi.org/10.2147/IJN.S129300.
[63] G. Caracciolo, S. Palchetti, V. Colapicchioni, L. Digiacomo, D. Pozzi, A.L. Capriotti, G. La Barbera, A. Laganà, Stealth effect of biomolecular corona on nanoparticle uptake by immune cells, Langmuir 31 (2015) 10764–10773, https://doi.org/10.1021/acs.langmuir.5b02158.
[64] Y. Yeo, Nanoparticulate Drug Delivery Systems: Strategies, Technologies, and Applications, John Wiley & Sons, 2013.
[65] M. Jansch, P. Stumpf, C. Graf, E. Rühl, R.H. Müller, Adsorption kinetics of plasma proteins on ultrasmall superparamagnetic iron oxide (USPIO) nanoparticles, Int. J. Pharm. 428 (2012) 125–133, https://doi.org/10.1016/j.ijpharm.2012.01.060.
[66] Y. Jiang, S. Huo, T. Mizuhara, R. Das, Y. Lee, S. Hou, D.F. Moyano, B. Duncan, X. Liang, V.M. Rotello, The interplay of size and surface functionality on the cellular uptake of sub-10 nm gold nanoparticles, ACS Nano 9 (2015) 9986–9993, https://doi.org/10.1021/acsnano.5b03521.
[67] J. Lin, A. Alexander-Katz, Cell membranes open "doors" for cationic nanoparticles/biomolecules: insights into uptake kinetics, ACS Nano 7 (2013) 10799–10808, https://doi.org/10.1021/nn4040553.
[68] L. Ostrovska, A. Broz, A. Fucikova, T. Belinova, H. Sugimoto, T. Kanno, M. Fujii, J. Valenta, M.H. Kalbacova, The impact of doped silicon quantum dots on human osteoblasts, RSC Adv. 6 (2016) 63403–63413, https://doi.org/10.1039/C6RA14430F.
[69] F. Marano, S. Hussain, F. Rodrigues-Lima, A. Baeza-Squiban, S. Boland, Nanoparticles: molecular targets and cell signalling, Arch. Toxicol. 85 (2011) 733–741, https://doi.org/10.1007/s00204-010-0546-4.
[70] A. Fucikova, J. Valenta, I. Pelant, M.H. Kalbacova, A. Broz, B. Rezek, A. Kromka, Z. Bakaeva, Silicon nanocrystals and nanodiamonds in live cells: photoluminescence characteristics, cytotoxicity and interaction with cell cytoskeleton, RSC Adv. 4 (2014) 10334–10342, https://doi.org/10.1039/C3RA47574C.
[71] C.C. Zimmer, Y.X. Liu, J.T. Morgan, G. Yang, K.H. Wang, I.M. Kennedy, A.I. Barakat, G.Y. Liu, New approach to investigate the cytotoxicity of nanomaterials using single cell mechanics, J. Phys. Chem. B 118 (2014) 1246–1255, https://doi.org/10.1021/jp410764f.
[72] D. Hanaor, M. Michelazzi, C. Leonelli, C.C. Sorrell, The effects of carboxylic acids on the aqueous dispersion and electrophoretic deposition of ZrO2, J. Eur. Ceram. Soc. 32 (2012) 235–244, https://doi.org/10.1016/j.jeurceramsoc.2011.08.015.
[73] R.W. O'Brien, B.R. Midmore, A. Lamb, R.J. Hunter, Electroacoustic studies of moderately concentrated colloidal suspensions, Faraday Discuss. Chem. Soc. 90 (1990) 301, https://doi.org/10.1039/dc9909000301.
[74] X. Wei, W. Jiang, J. Yu, L. Ding, J. Hu, G. Jiang, Effects of SiO2 nanoparticles on phospholipid membrane integrity and fluidity, J. Hazard Mater. 287 (2015) 217–224, https://doi.org/10.1016/j.jhazmat.2015.01.063.